Pedro Gonçalo Dias de Almeida

Licenciado em Ciências de Engenharia Física

Cylindrical Spinning Rotor Gauge — A new approach for vacuum measurement

Dissertação para obtenção do Grau de
Mestre em Engenharia Física

Orientador: Orlando M. N. D. Teodoro, Professor Associado,
Universidade Nova de Lisboa

Júri:

Presidente:	Doutora Maria Isabel Simões Catarino
Arguente:	Doutor Augusto Manuel Celorico Moutinho
Vogal:	Doutor Orlando Manuel Neves Duarte Teodoro

FACULDADE DE CIÊNCIAS E TECNOLOGIA
UNIVERSIDADE NOVA DE LISBOA

September, 2015

Cylindrical Spinning Rotor Gauge —
A new approach for vacuum measurement

Acknowledgements

Firstly, I would like to express my sincere gratitude to my advisor Professor Orlando Teodoro for giving me the chance to work in such an interesting project, for the stimulating discussions and his innovative ideas that made this dissertation so exciting.

Besides my advisor, I would like to thank everyone in the METROVAC laboratory for providing such a positive work environment, specially Nenad Bundaleski for the various insightful discussions and João Santos for his availability to help no matter how small the problem was.

I am grateful to José Carlos Mesquita for not only going to great lengths to make sure I always had the necessary resources available, but also for all the cake slices and for being a great company throughout the project.

I would like to thank João Faustino for his commentaries and the meticulous building of the first prototype parts in the physics department's workshop. As well as Mr. Luís from the conservation and restoration department for the careful manufacture of the glass chamber.

My sincere thanks to the faculty's library for making 3D printing available for everyone and specially to Filipe Silvestre for all the tips and for teaching me how to operate the 3D printer.

My gratitude to Mario Xavier for the help with the finite element method (FEM) simulations.

I would also like to thank my brother João Almeida who, besides being family with all that that entails, helped me troubleshoot some of the python code.

Finally, I am particularly grateful for having shared this journey with awesome people, who made this experience unforgettable. Specially Andry Teixeira for being a daily source of inspiration and support throughout these years. And last but not least, nothing would be possible without my family's unconditional support to whom I owe everything.

ABSTRACT

The spinning rotor gauge (SRG) is one of the most interesting vacuum gauges ever made, covering a pressure range of over seven orders of magnitude, with minimal gas interference (no pumping, ionization or heating of the measured gas), and a great stability of less than 1% drift per year.

But despite its remarkable properties, apparently the SRG has not been further developed since the eighties, when it gained commercial interest.

In this context, this dissertation aims at providing a starting point for a new line of investigation regarding this instrument, focused on the rotor itself.

A brief study of different rotor geometries is provided, including a comparison between a cylindrical rotor and a spherical one. A cylindrical spinning rotor gauge (CSRG) is then proposed, based on the original SRG, but requiring a completely new lateral damping system. A prototype was built and tested against a non calibrated reference gauge.

Keywords: vacuum, gauge, magnetic levitation

RESUMO

O *spinning rotor gauge* (SRG) é um dos manómetros de pressão mais interessantes devido ao facto de cobrir uma gama de pressões superior a sete ordens de grandeza, de não interferir com o gás medido (não bombeia, ioniza nem aquece o gás), e de ter uma estabilidade com variações inferiores a 1% por ano.

Apesar das suas excelentes propriedades, aparentemente o SRG não foi desenvolvido de forma significativa desde os anos oitenta, altura em que ganhou interesse comercial.

Neste contexto, esta dissertação procura providenciar as condições necessárias ao desenvolvimento de uma nova linha de investigação sobre este instrumento, com um foco no rotor deste.

É apresentado um breve estudo sobre diferentes geometrias, incluindo uma comparação entre rotores cilindricos e rotores esféricos. É proposto um *cylindrical spinning rotor gauge* (CSRG) baseado no SRG original, mas com um sistema de estabilização horizontal completamente novo. Foi construído um protótipo que posteriormente foi testado e comparado a um manómetro não calibrado de referência.

Palavras-chave: vácuo, manómetro, levitação magnética

CONTENTS

List of Figures

List of Tables

GLOSSARY

$\bar{c}$ average molecular speed.

Ψ energy potential field.

ε vacuum permittivity.

ω angular frequency.

θ polar angle.

ϕ azimuth angle.

σ momentum accommodation coefficient.

τ the time needed for the rotor to complete a predefined number of turns.

ρ density.

γ electrical conductivity.

χ_e electric susceptibility.

ε_r relative permittivity.

μ_r magnetic permeability of free space.

A area.

B magnetic flux density.

E electric field.

F force.

F_e electric force.

F_m magnetic force.

H magnetic field.

I moment of inertia.

J current density.

L angular momentum.

M molecular mass.

P polarization.

P_{EC} power loss by eddy current.

R molar gas constant.

S surface.

T temperature.

V volume.

a relative proportion of each gas of the measured pressure.

c speed of light.

d distance to the axis of rotation.

f frequency.

h cylinder height.

m mass.

p pressure.

p_l light pressure.

p_m dipole moment.

q electric charge.

r radius.

t time.

z cylindrical longitudinal coordinate.

CSRG cylindrical spinning rotor gauge.

FEM finite element method.

LED light-emitting diode.

PLA Polylactic acid, a biodegradable thermoplastic aliphatic polyester.

SRG spinning rotor gauge.

TTL transistor to transistor logic.

CHAPTER 1

INTRODUCTION

Vacuum technology has been established for a long time, from the industry to scientific research. Scientifically, it is a very old subject but its technology keeps on pushing the boundaries of what is possible to achieve. A good example of this evolution are the particle accelerators, where ultra high vacuum has to be sustained continuously for incredibly large volumes. Besides these outstanding systems, there are aspects of the technology that can be improved like cost, easy maintenance, reliability, etc.

In this context, the spinning rotor gauge is one of the most interesting pressure gauges. It has an incredible pressure range of operation that can theoretically go from 10^{-7} mbar up to atmospheric pressures. Also, this gauge does not heat up the gas molecules in the measuring process, nor does it pump the gas, ionise its particles or change its properties in any other way; which alone is enough to make it more interesting than many other competing gauges.

Unfortunately, according to the literature there were no significant developments in this field of research ever since this instrument gained commercial interest in the eighties.

Not only could the commercial units still be improved by broadening their operation range to higher and lower pressures or increasing the instrument's reading rate, for example, but there is also interest in using this instrument to investigate other physical phenomena.

The virtual absence of friction allows the sensing of very subtle effects, that would usually be inaccessible. The low pressure gas friction is one of them, but others have been studied, such as temperature that can affect the rotor's moment of inertia through its expansion coefficient, the Coriolis effect due to earth's rotation, momentum exchanged by radiation pressure or even more subtle effects like Keith's gravitational effect [1].

Radiation pressure effects have already been reported by Fremerey [2], and one of the starting motivations behind this project was to see if it was possible to accelerate the rotor by applying tangential radiation pressure to it. Other interests include testing other rotors with possibly different geometries or composed by more than one material.

Such developments can only take place after the construction of a prototype. With future improvements like these in mind, the proposed prototype makes use of a cylindrical rotor instead of a spherical one, which alone required a whole new lateral stabilization system based on Hall sensors. Therefore, this dissertation is aimed at providing a starting point for a new line of investigation regarding this pressure gauge.

A study of the working principles is provided followed by the proposition and consequent implementation of a working prototype. In the end, pressure measurements were performed and compared with a reference gauge.

CHAPTER 2

MAGNETIC LEVITATION SYSTEMS

Magnetic levitation is far from being a trivial achievement. At first glance, one could assume that a carefully arranged static set of magnets could repel a smaller magnet in such a way that would allow stable suspension, but in fact, this is not possible.

This is known as the Earnshaw's theorem [3]. It was published in 1849 by Samuel Earnshaw, who proved that it is impossible to achieve a stable static configuration of particles solely based on each other's inverse-square law forces. Gravity and electromagnetism fall into such category, which at the time held many implications in the structure of the universe as it was then understood, and raised fundamental questions concerning the atom's internal composition that would only be answered with the development of relativity and quantum mechanics.

Notwithstanding its consequences, this theorem makes certain assumptions that can be bypassed making magnetic levitation possible under special conditions. These cases include superconductivity [4], diamagnetism [5], mechanical constraints (or pseudo-levitation) [6], non-static arrangements (such as the levitron [7]), time-varying fields, and also the solution used by the spinning rotor gauge, active feedback control [8].

Given its relevance for magnetic levitation, an illustration of the theorem will be provided in the context of electromagnetic fields.

2.1 Earnshaw's Theorem

One way to state this theorem is to say that no stable equilibrium can be attained by a particle in any sum of energy potential fields Ψ of inverse-square law forces.

For a stable equilibrium to occur, two necessary conditions must be met.

1. In the equilibrium point the net force must be zero.

$$\sum \boldsymbol{F}_i = -\nabla \sum \boldsymbol{\Psi}_i = 0 \tag{2.1}$$

This would be sufficient for equilibrium, but not enough for stability. Hence the need for a second condition.

2. If a particle subjected to the aforementioned force field was to be placed in the said equilibrium point, there would have to be an arbitrary small vicinity around that point where the force points inwards as to oppose any displacement, independently of its direction.

In other words, the equilibrium has to be located in a relative minimum of the potential field.

$$\nabla^2 \sum \boldsymbol{\Psi}_i > 0 \tag{2.2}$$

However, this condition cannot be satisfied since this kind of potential satisfies the Laplace equation [9].

$$\nabla^2 \sum \boldsymbol{\Psi}_i = 0 \tag{2.3}$$

Therefore, no minimum points can exist in the potential of a inverse-square force. Equilibrium points do exist, but only as saddle points.

Gauss's law can be used to illustrate this property in electric fields, and given that the conclusion also applies to magnetic fields, it will help characterize the limitations this theorem entails for magnetic levitation and the respective workarounds.

An electrostatic field that fulfils the requirements stated in equations 2.1 and 2.2 would have equipotential lines surrounding the minimum point, and force lines perpendicular to them. In the case of a positive charge, the force lines would have to point inwards as to provide the restoring force (as seen in the figure 2.1a), and in the case of a negative charge, they would have to point outward.

The field represented in figure 2.1a results from the requirements stated for the existence of a minimum value in the electrostatic potential. As such, this field is impossible to occur as it would mean that flux lines would disappear in the minimum point without the presence of a charge, which goes directly against Gauss's law.

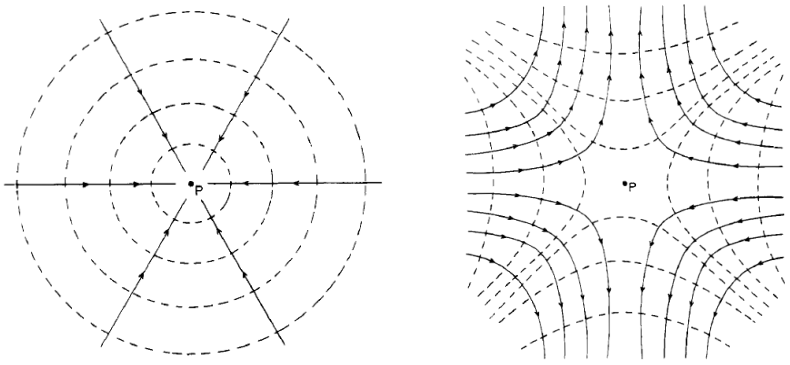

(a) Impossible situation where P is a minimum point

(b) Realistic situation where P is a saddle point

Figure 2.1: Comparison between two electric fields, the dotted curves are equipotentials while the full curves represent lines of force [9].

In such a field, if a Gaussian surface S of spherical shape is centred at the minimum point, and given that the electric field $\boldsymbol{E}$ points inwards, Gauss's law will result in the following

$$\iint \boldsymbol{E} \cdot \mathrm{d}\boldsymbol{S} < 0 \tag{2.4}$$

where $\mathrm{d}\boldsymbol{S}$ is an outward-oriented infinitesimal surface area element of the Gaussian sphere. From the divergence theorem, this implies the existence of a charge inside the surface.

$$\iint \boldsymbol{E} \cdot \mathrm{d}\boldsymbol{S} = \iiint \nabla \cdot \boldsymbol{E} \, \mathrm{d}V = \frac{q}{\varepsilon} < 0 \tag{2.5}$$

Meaning that it is impossible to create a minimum in an electric field potential, and that imposing the stability criteria on an electric field results in the necessity of a charge being present in the aforementioned (and supposed vacant) minimum point, in order to comply with Gauss's law.

Until now everything was done with particle charges in mind, but the proof stands for dipoles [10].

A dielectric body located in an electrostatic field $\boldsymbol{E}$ suffers a polarisation $\boldsymbol{P}$ dictated by the body's electric susceptibility χ_e.

$$\boldsymbol{P} = \chi_e \boldsymbol{E} \tag{2.6}$$

From which the dipole moment p_m may be calculated over the volume V of the body.

$$\boldsymbol{p_m} = \int \boldsymbol{P} \, \mathrm{d}V \tag{2.7}$$

$$\boldsymbol{p_m} = \int \chi_e \boldsymbol{E} \, \mathrm{d}V \tag{2.8}$$

This last equation's integral can be simplified by assuming that the dipole is small enough for the electric field to be constant.

$$\boldsymbol{p_m} = \chi_e \boldsymbol{E} V \tag{2.9}$$

The dipole moment is then used to calculate the force generated on the body.

$$\boldsymbol{F_e} = (\boldsymbol{p_m} \cdot \nabla)\boldsymbol{E} \tag{2.10}$$

$$\boldsymbol{F_e} = \chi_e V (\boldsymbol{E} \cdot \nabla)\boldsymbol{E} \tag{2.11}$$

The electric susceptibility is defined by $\chi_e = \epsilon_r - 1$ where ϵ_r is the relative permittivity of the material, and mathematically $(\boldsymbol{E} \cdot \nabla)\boldsymbol{E} = \frac{1}{2}\nabla \boldsymbol{E}^2$.

$$\boldsymbol{F_e} = \frac{1}{2}\left(\epsilon_r - 1\right) V \nabla \boldsymbol{E}^2 \tag{2.12}$$

The force acting on the dipole can be analysed in the context of the stability criteria, namely the condition expressed by equation 2.2.

$$\nabla^2 \boldsymbol{\Psi}_e = -\nabla \boldsymbol{F_e} \ > \ 0 \tag{2.13}$$

$$-\nabla \left(\frac{1}{2}\left(\epsilon_r - 1\right) V \nabla \boldsymbol{E}^2 \right) > \ 0 \tag{2.14}$$

Yet the volume V, the electric susceptibility $(\epsilon_r - 1)$ and the term $\nabla \boldsymbol{E}^2$ are always positive values, making this inequality impossible and thus confirming the Earnshaw's theorem for electric dipoles.

Analogously to the electric force in equation 2.12, it is possible to write the magnetic force acting on a magnetic dipole [10].

$$\boldsymbol{F_m} = \frac{1}{2}\left(\mu_r - 1\right) V \nabla \boldsymbol{H}^2 \tag{2.15}$$

To which the same stability criteria is applicable.

$$-\nabla \left(\frac{1}{2}\left(\mu_r - 1\right) V \nabla \boldsymbol{H}^2 \right) > 0 \tag{2.16}$$

And although the same reasoning applies to the volume V and the term $\nabla \boldsymbol{H}^2$, the magnetic susceptibility $(\mu_r - 1)$ is different since it can in fact be a negative number for a number of magnetic effects including diamagnetism, superconductivity and eddy current induction. Meaning that it is possible for these type of systems to find a stable configuration.

2.2 Beyond the Earnshaw's Theorem

The conclusion that magnetic levitation is possible does not mean that Earnshaw's theorem has exceptions. In fact, the reason why these types of magnetism are able to overcome its limitations is because they do not act as typical inverse-square laws.

2.2.1 Diamagnetism

Diamagnetism is a very subtle magnetic effect that is way less pronounced than paramagnetism or ferromagnetism. It results from a change in the electrons orbital velocity due to an external magnetic field in accordance to Lenz's law. In absence of an external magnetic field affecting the electrons of the material, a pure diamagnetic material will not show any signs of having magnetic properties.

Given its nature, this type of material acts as if it wants to expel the magnetic field within itself, hence the relative permeability being less than one. The magnetic field produced is dependent on the orientation of the external magnetic field, and the force produced will always be repulsive.

For this system

$$\nabla^2 \boldsymbol{B}^2 \geq 0 \tag{2.17}$$

Which means that a stable configuration is actually possible to achieve [11]. Every material has diamagnetic properties. In theory this could mean that every material could be levitated, but this is not a very practical approach since this effect is very weak and massive fields are necessary to levitate even small objects. To give a sense of scale, the magnetic field used for the levitation of the frog in figure 2.2 has an intensity of 16 T.

Figure 2.2: diamagnetic levitation of a frog [11].

The intensity of the magnetic field is always dependent on the diamagnetism of the material, and its density. One can generate very intense magnetic fields in order to levitate any purely diamagnetic object or even use simple tabletop setups to levitate small objects with low density like pyrolytic carbon or bismuth. Either way, it excludes every material with paramagnetic or ferromagnetic properties since these magnetic effects are much more

pronounced, and require incredibly intense magnetic fields or special materials, making this solution far from a general purpose application.

In the context of vacuum measurement it is interesting to note that despite its limitations, this type of diamagnetic levitation was used in one of the first SRG-like vacuum manometers [12].

2.2.2 Superconductivity

Superconductors are regarded as perfect diamagnets, with $\mu_r = 0$. A superconductor will always generate the magnetic field necessary to prevent the penetration of the field within the superconducting material. Additionally to this perfect diamagnetic effect there is also the pinning of flux lines in Type II superconductors, where the magnetic field is allowed to penetrate the superconductor but gets pinned holding the external magnetic field in place. If this external field is caused by a magnet above the superconductor, chances are that it will levitate in a very stable configuration.

Despite being one of the most spectacular ways to achieve magnetic levitation, the superconducting requirements are not very practical for an ordinary instrument.

2.2.3 Mechanical Constraints

The Earnshaw's theorem only stands for 3D space. In two dimensions, or in one dimension, it is possible to create a magnetic field with a minimum point. Although this alone is not a feasible solution, if the object is somehow restricted to a plane or axis, it is then possible to create a magnetic minimum along that plane or axis, resulting in a partial levitation, also called pseudo-levitation.

(a) 3D render [13]

(b) Schematic representation [14]

Figure 2.3: The Mendocino motor is a device designed around this concept [13–15].

Despite not being a complete levitation system, since there is a mechanical constraint along one of the axes, it can be useful nonetheless.

The Mendocino motor represented in figure 2.3, is a good example. Magnets in both ends of the motor's axes are repelled by two pairs of magnets at ground level. This creates a potential saddle point with instability along the axis. After offsetting the magnets ever so slightly in a preferred direction, a vertical wall is then provided as a means to constrain the freedom of the motor on the said direction, effectively trapping the motor in place.

This is a quite simple approach to implement passive magnetic bearings [6].

2.2.4 Non-static Arrangements

Dynamic effects are not considered by the Earnshaw's theorem, and can also be exploited to achieve magnetic levitation.

The Levitron^{TM} is a toy discovered and patented by Roy Harrigan in 1983. It is composed by a strong permanent magnet base that levitates a spinning permanent magnet hand-spun top, like shown in figure 2.4a. Both magnets have a vertically aligned magnetic field but with opposing directions.

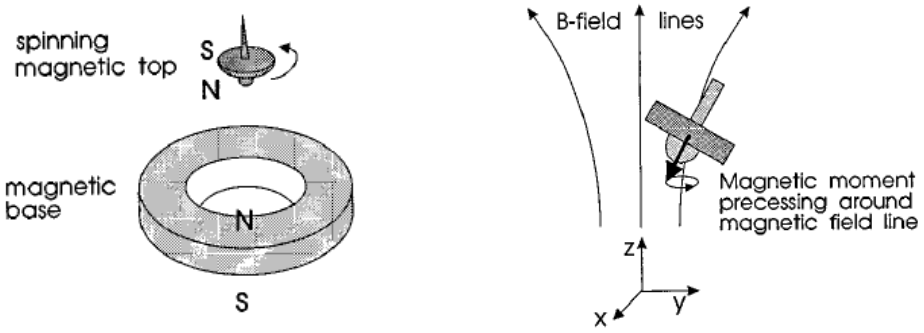

(a) (b)

Figure 2.4: a) diagram of the Levitron^{TM} setup and b) diagram of the spin-precessing stabilization process [7].

The spinning itself provides gyroscopic stability against the flipping of the top. But that alone is not enough since Earnshaw's theorem would still prevent the levitation from being stable. As Simon and colleagues have shown [7], the gyroscopic precession of the spinning axis around the magnetic field lines is what enables the magnetic levitation. As the top displaces itself from the equilibrium, the orientation of the precession axis moves along the local field direction, and thus providing the necessary stabilization, as shown in figure 2.4b. A curious consequence of this mechanism is that if the top spins too fast, the increased gyroscopic stability will reduce the precession stabilization and make the levitation impossible.

Another interesting example of a non-static levitation system is called the indutrack [16] and was proposed by Richard Post for a possible magnetic levitated train, or maglev. There are several different approaches to this application, but this one in particular takes advantage of the movement of the train relative to its track to induce repulsive currents. The train is equipped with special arrays of permanent magnets called Halbach arrays, discovered by Klaus Halbach for particle accelerators applications. This array is composed of magnets with a rotating pattern of magnetization in a way that reduces the magnetic flux on one side of the array and maximizes it on the other, as can be seen in figure 2.5. With this magnetic field being practically sinusoidal along the array [16].

The track itself is equipped with a close-packed array of shorted circuits. As the

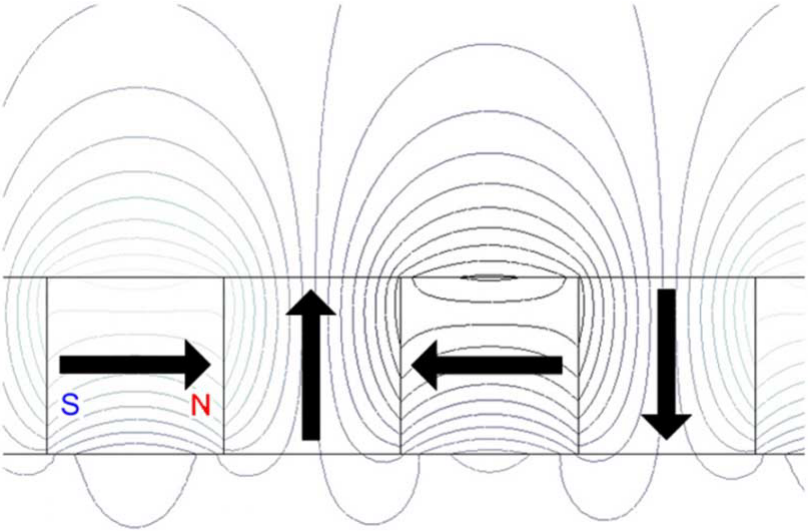

Figure 2.5: Four magnet segments of a Halbach array with respective magnetic flux lines.

train moves over the track, currents are induced in the shorted circuits by the sinusoidal magnetic field of the Halbach array, whose frequency will depend on the train's velocity. The induced currents will generate a repelling magnetic field with the same frequency but with a phase lag due to the circuits impedance, resulting in an always repelling force able to sustain the train. This approach has several problems, namely the fact that it only works for a train moving over a certain speed.

Today, the technology used in maglevs is based on feedback control, which will be explained further ahead. Besides trains, this technology has also been considered by NASA for the launching of rockets [17].

The indutrack falls into a category known as electrodynamic suspension, where a time dependent magnetic field induction is responsible for the levitation's repelling forces. In non static arrangements this magnetic field comes from moving magnets, but the same effect can be attained by an alternating electromagnet.

2.2.5 Time-varying Fields

Time-varying fields can also achieve stable levitation through electrodynamic suspension. Analogous to the indutrack system, and instead of relying in moving magnets, alternating magnetic fields created by electromagnets can be used to induce alternating currents in conductors, in the same fashion explained in the non-static arrangements section in order to achieve the same effect. The advantage here would be the fact that static levitation is possible, similarly to diamagnetic levitation.

There are several examples of applications for this approach. These include levitation melting of metals, the Bedford levitator, or even magnetic bearings.

Despite their role in electrodynamic suspension, there are other ways to employ time-varying magnetic fields to avoid the Earnshaw's theorem limitations. Ion traps like the

Paul or the Penning ion traps make use of alternating electromagnetic fields to trap ions in a space region.

2.2.6 Active Feedback Control

In 1937, Holmes developed a way to surpass the Earnshaw's theorem's restrictions by generating a dynamic magnetic field with a coil [8]. Considering that the magnetic field intensity generated by the coil has a proportional relation to its current, it was possible for Holmes to create a sensing circuit that would adapt the magnetic field intensity to the body's position, resulting in a macroscopically stable magnetic levitation.

Contrasting with the majority of other solutions, the active feedback control method does not require the existence of a minimum in the potential field. Instead, the levitating body is kept in the unstable equilibrium point, and as it moves away from this point, the sensing circuit responds by providing damping forces to keep the body in place. Consequentially, it is theoretically impossible to keep the body perfectly stable, hence the use of the expression "macroscopic stability". Yet, it can virtually be made as stable as necessary to meet any application requirements.

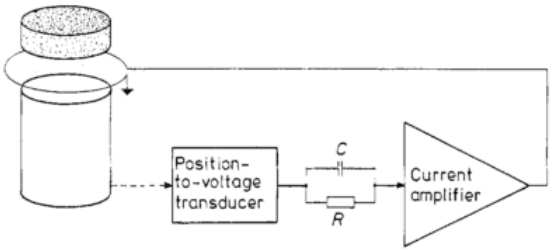

Figure 2.6: Feedback levitation system diagram [18].

A feedback control system (as seen in figure 2.6) is usually comprised of a position-to-voltage transducer, that converts the suspended object position into an electric signal; a control element, that outputs the appropriate response of the system based on the position of the body over time; and an output amplifier that will apply the response to the coil, keeping the object in place.

The position-to-voltage transducer can be based on a number of different physical principles. In the first levitation systems a beam of light would be partially blocked by the suspended body and detected by a light sensitive electric component, like a photodiode. If the body were to move, the consequent blocking or unblocking of the light beam would yield a response in the output of the optical sensor. Being based on light, there is no interference from the surrounding magnetic fields, which can be an advantage over other solutions. On the other hand, this method gets harder to use as rotors get smaller, and it also requires open view over the suspended object, making it harder to operate inside enclosed spaces, like vacuum chambers, for example.

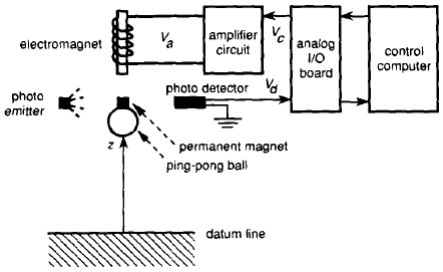

Figure 2.7: Optical-based magnetic levitation system [19].

Avoiding these issues, impedance-based sensing systems were implemented as seen in figure 2.8 with very good results, becoming what is probably the most widespread transducer. An RLC oscillator circuit is tuned at radio frequencies with the inductor being a coil placed above or under the suspended body. This inductance changes with the proximity of the body, bringing the oscillator frequency closer or farther away from resonance. The oscillator's rectified output signal is higher when the frequency is closer to resonance, and lower if otherwise, indicating the body position. This is the approach used by the spinning rotor gauge, and many other applications.

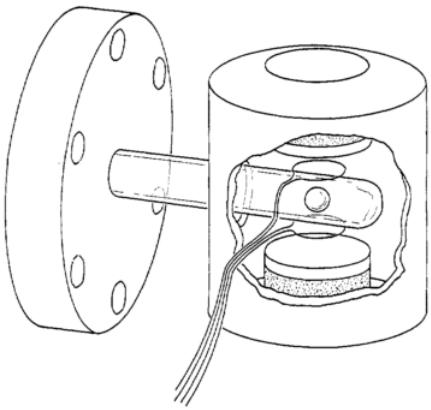

Figure 2.8: Impedance-based magnetic levitation concept used by Fremerey in the SRG [18].

According to the literature, Hall sensors were never used in this context. For this reason, some experiments were done based on these sensors. Unlike previous examples, Hall sensors measure magnetic field and since the magnetized body has a magnetic field of it's own, it is possible to measure it and get a position signal from it. This is relatively easy to implement, but because both the input and the output of the system are magnetic fields there is the possibility of interference if they are not properly filtered.

These are some of the most relevant sensing systems in this line of investigation, among innumerable others, from lasers to capacitor electrodes mounted near the body.

The controlling aspect of the feedback loop can also be accomplished in a number of ways. Usually, the spinning rotor gauge is controlled by analogue electronics, meaning that

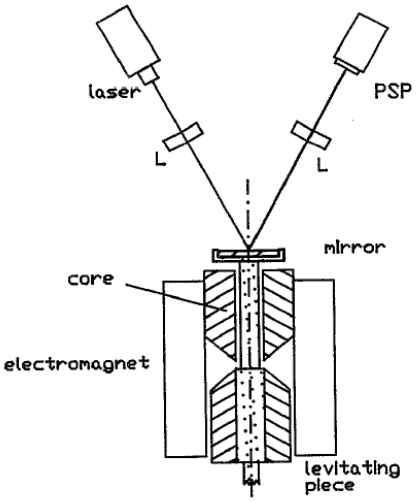

(a) Cutaway view of the system's configuration

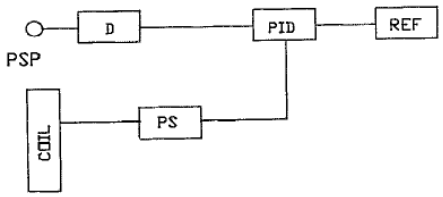

(b) PID controller of the system

Figure 2.9: Optical-based feed back controlled magnetic levitation [20].

simple controllers are used, like PID controllers or phase-lead compensators. However, more advanced schemes have also been used and proposed [19, 21–25].

Feedback systems are a very adaptable solution since they do not require special magnetic properties like diamagnetism or superconductivity nor do they have an exceedingly amount of stability conditions like the levitron. When they were initially proposed in the beginning of the twentieth century, the relatively complex electronics involved could be seen as drawback, but with the remarkable technological advances made since then this is no longer the case. Being one of the most reliable, versatile and inexpensive solutions to the restrictions posed by the Earnshaw's theorem, feedback systems became the go-to solution for most magnetic levitation applications, the spinning rotor gauge being one of them.

CHAPTER 3

THE SPINNING ROTOR GAUGE

The spinning rotor gauge was developed throughout the 20th century, alongside feedback control magnetic levitation which was also being used in several other applications like centrifuges [26, 27], high precision scales [28] or even beam choppers [18, 29].

However, the basic concept of studying a gas by measuring its interaction with a rotating body is even older, it started in the 19th century with Meyer, Maxwell and Kundt, among others [30]. Back then, the rotating body consisted of a disk hanging by a thread, which would typically look like the figure 3.1a. This type of setup was used until Holmes proposed one of the first feedback controlled magnetic levitation systems, shown in figure 3.1b.

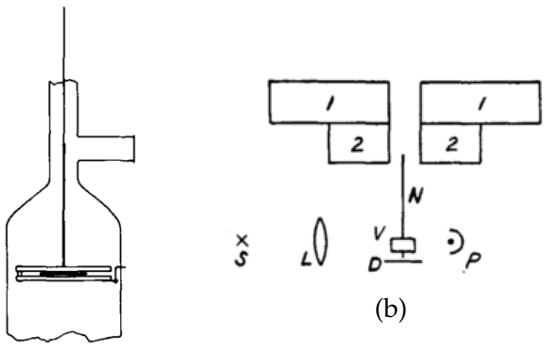

(a) (b)

Figure 3.1: a) is a typical thread-based setup [30] and b) Holmes' first magnetic levitation system proposal [8]. Where *1* and *2* identify the two levitation coils, *P* a photocell, *S* a source of light, *L* a focusing lens, with a vane *V* attached to *N* and a damping plate *D*.

The feedback controlled magnetic levitation concept presented clear advantages over the thread-based one which Beams [26–28, 31–35] explored and developed. He made an in-depth analysis of the several variables involved, different coil configurations, properties of

the suspended body and also worked on several solutions for the position sensing circuit and respective feedback system. From these studies, he was able to propose and build devices for several applications [26–28]. But most importantly, he made very valuable contributions to magnetically levitated pressure sensing systems [31–34], which culminated in the first concept proposal of the SRG [35].

According to this concept, a body is suspended magnetically in vacuum and after being subjected to an angular acceleration by a rotating magnetic field, it is left to spin freely. By measuring the consequent angular velocity attenuation due to friction with the surrounding remaining air particles it is possible to deduce the pressure of that vacuum.

As a result of several studies on very high frequency rotation systems, Beams is still to this day the record holder for angular velocity obtained in this kind of device according to the literature, after achieving an angular frequency of 386 000 rps with a steel ball of 0.795 mm in diameter [31, 36], as demonstrated by the table in figure 3.1.

Table 3.1: World record rotation speeds obtained by Beams in 1946 [31].

Diameter of the Rotor (mm)	Rotor Speed (rps)	Peripheral speed (cm/s)
3.97	77 000	9.60×10^4
2.38	123 500	9.25×10^4
1.59	211 000	1.05×10^5
0.795	386 000	9.65×10^4

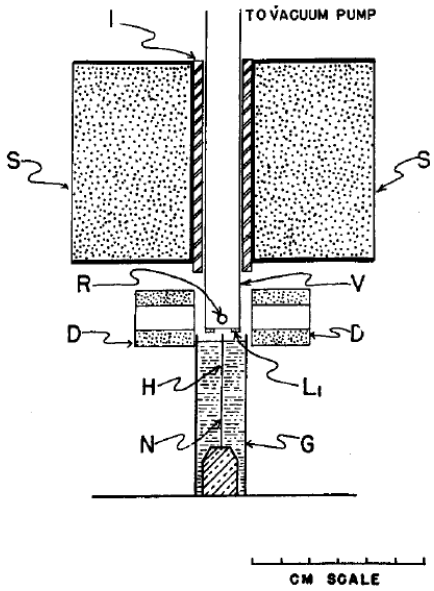

Figure 3.2: Diagram of the Beam's record holder magnetic levitation system [31]. Being *L1* the position sensing coil, *R* the rotor, *S* the levitation coil, *I* a hollow magnetic core, *V* the vacuum connecting tube, *D* the driving coils and the needle *H*, the wire *N* and the glass tube *G* form the lateral damping system.

MacHattie, a Beams' associate, also made a significant contribution by comparing the levitation of rods and spheres [37].

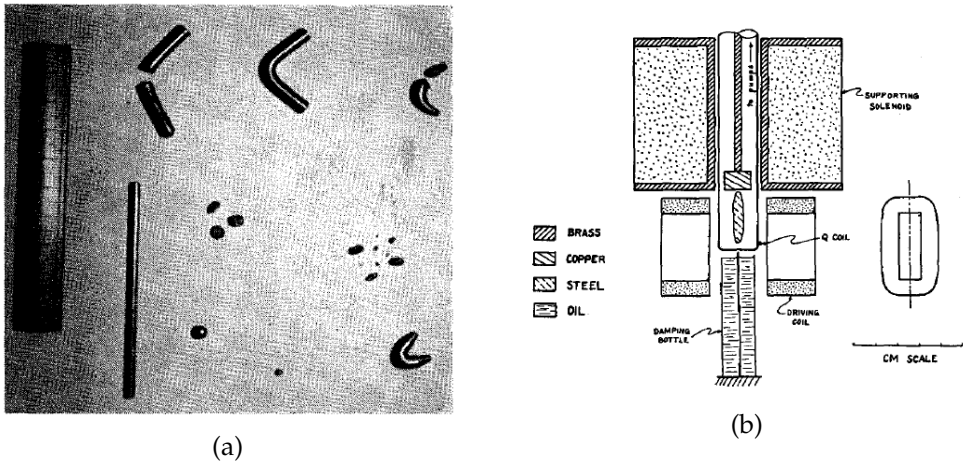

(a) (b)

Figure 3.3: a) is a photography of rotors bent and shattered by McHattie and b) a diagram of the magnetic levitation system he used [37].

Many other authors made contributions either to magnetic levitation systems or to the SRG concept. Some, apparently working independently, found different solutions to the same problem, like Evrad and Beaufils [12] that built a SRG based on diamagnetic suspension shown in figure 3.4a, and used a very ingenious method to deliver torque to the rotor with the careful targeting of the molecules of the measured gas itself as seen in figure 3.4b.

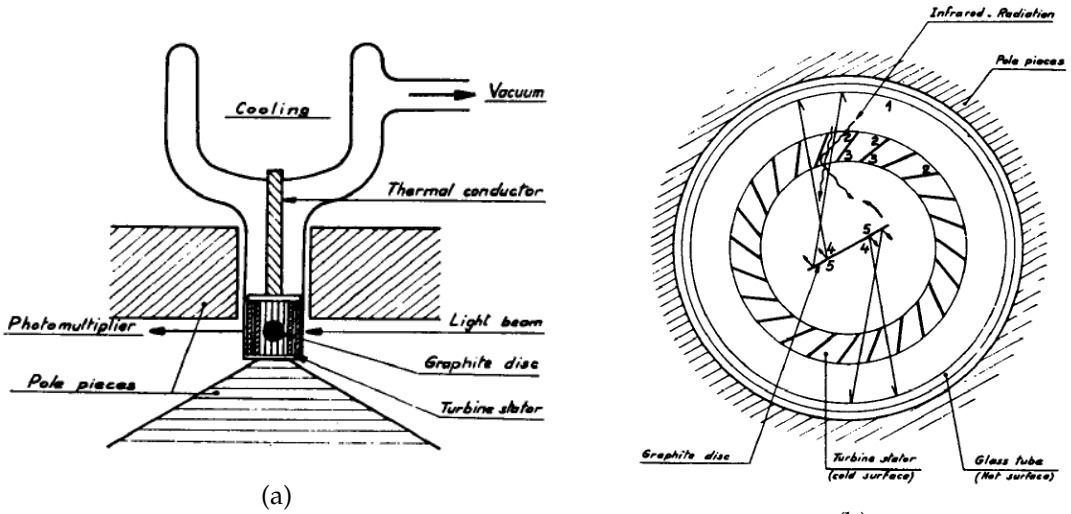

(a) (b)

Figure 3.4: a) diagram of the diamegnetic levitation concept and b) top-view diagram of the torque delivery system [12].

Lord and colleagues made several contributions regarding the interaction between the surface of the rotor and the measured gas, from which the ones that stand out the most are focused on the study of the momentum accommodation and the way parameters like roughness affect the results [38–40]. Steckelmacher is also the author of a noteworthy study regarding this subject [41].

Table 3.2: Summary of the different SRGs built over time with the respective authors. Adapted from Fremerey's state of the art analysis in 1982 [30].

Authors	Year of publication	Type of rotor	Suspension	Pressure range (mbar)
Meyer	1865	disk	bifilar wire	$10^3 - 1$
Maxwell	1866	"	single wire	$10^3 - 10$
Knudt and Warburg	1875	"	bifilar wire	$10^3 - 1$
Hogg	1906	"	single wire	$10^{-1} - 10^{-4}$
Knudsen	1934	sphere	"	$-$
Beams et al	1946	"	ferromagnetic	-10^{-5}
Beams et al	1962	"	"	$10^{-4} - 10^{-7}$
Harbour and Lord	1965	"	"	$10^{-3} - 10^{-5}$
Evrard and Beaufils	1965	vane	diamagnetic	$10^{-3} - 10^{-7}$
Thomas and Lord	1974	sphere	ferromagnetic	$-$
Lord	1977	disk	"	$10^{-2} - 10{-}3$
Lord and Thomas	1977	"	"	-10^{-2}
Comsa et al	1977	sphere	permanent ferromagnetic	$10^{-3} - 10^{-4}$
Comsa et al	1980	"	"	$10^{-2} - 10^{-5}$
Comsa et al	1980	sphere and vane	"	$10^{-3} - 10^{-4}$
Messer	1980	sphere	"	-7×10^{-4}
Messer and Rubet	1980	sphere and vane	permanent ferromagnetic and diamagnetic	-3×10^{-4}
Fremerey	1984	sphere	ferromagnetic	$1 - 10^{-7}$

Later, Fremerey was of vital importance in turning the concept, and all these different author's studies, into a fully fledged device. He not only worked in the instrumentation behind it [18], but also on the relation between pressure and the loss of the rotor's angular momentum, culminating in the 1980's in the spinning rotor gauge as we know it [42], shown in figure 3.5.

Fremerey's proposition took a lab promising concept and built an incredibly compact, reliable and easy to use instrument. In fact, the SRG proposed by him in 1984 was so mature and well designed all around that it would stay fundamentally unchanged until the time of writing this dissertation, over thirty years after, and apparently will keep on going for the foreseeable future.

Around that time, the qualities of Fremerey's SRG made it a commercial viable product. His work gave birth to several patents [43–46]. Commercial units were made available, and sadly, with few exceptions, it seems from the literature that the investigation regarding this fascinating instrument has stopped.

3.1 Gauge's Operation Principle

The following explanation of the spinning rotor gauge's operation is based on the article published by Fremerey in 1984 [42] given that in spite of being over thirty years old it has not suffered any significant change in the way it operates.

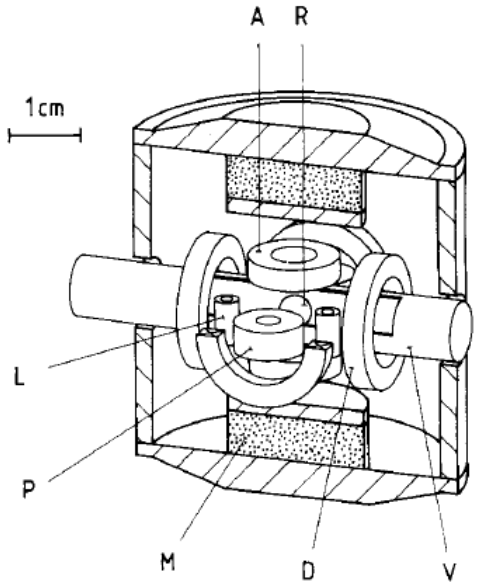

Figure 3.5: The spinning rotor gauge [42]: R - rotor; V - vacuum enclosure; M - one of two permanent magnets; A - one of two coils for pickup and control of axial rotor position; L - one of four coils of lateral damping system; D - one of four drive coils; P - one of two pickup coils.

At the center, there is a tube (identified by "V" in figure 3.5) connected to the vacuum chamber. Inside it, a sphere with 4.5 mm in diameter is magnetically suspended and rotated by the rest of the system. After measuring its deceleration due to gas friction, it is possible to assess the pressure inside the chamber.

3.1.1 Vertical Stabilization System

The suspension is achieved by two vertical permanent magnets (identified by "M") which create an equilibrium point middle way along the symmetry axis where the magnetic and gravitational forces cancel. However, the natural instability of the system dictates that as the body is displaced of its equilibrium point, towards either end, the magnetic attraction will increase, lengthening the displacement. For this reason, the magnets are aided by two vertical coils (identified by "A") that are responsible for assessing the rotors position and applying the necessary restoring magnetic forces to it. When the rotor flips upward, the lower magnet's attraction is supported by the lower coil, and likewise, when the rotor flips downward.

The decision to strengthen the upper or the lower magnetic field can only be done after assessing the rotor's position. This is accomplished by comparing the RF impedance of both coils, since they are sensible to the rotor's presence, and from this comparison it is possible to identify the rotor's position.

3.1.2 Lateral Damping System

The vertical magnetic field is responsible for some of the lateral damping, consequence of the fact that the field is stronger in the vertical symmetry axis. Nevertheless, there is still need for further lateral damping to assure better stability and control over the system.

To this end, there are four coils oriented vertically (identified by "L") that are responsible for the correction of any displacement along the horizontal plane. Given the rotor's strong vertical magnetization, any movement towards a coil will cause voltage induction. The signal is then amplified and applied to the coil in the opposite side resulting in the generation of a magnetic field that will interact with the rotor in such a way as to provide damping and restoring forces along the direction of those coils.

3.1.3 Rotation System

The physical principles behind the rotation system are quite similar to those of an induction motor.

Four coils (identified by "D") facing the rotor are supplied an AC current with a phase shift between them as to obtain a two-phase motor driving magnetic field. The orientation of the rotating magnetic field has to be horizontal in order to maximize the torque generated and to minimize possible interference with the magnetic levitation.

Under normal operation, the rotor is accelerated by the rotation system up until 400 Hz. After achieving this velocity, the rotation system is shut off and the rotor is left to coast.

3.1.4 Rotor's Frequency Detection

Two pickup coils (identified by "P") are used to determine the rotation frequency. They are exposed to the rotating component of the rotor's magnetic field, and as a result an AC inductive signal is observed and used to do the measurement.

This rotating component exists because the magnetization axis is slightly inclined from the spin axis. As such, every turn the magnetic poles will alternately point more towards each coil. A differential signal between the two coils allow the rejection of external magnetic fields or the coupling with the rotating field.

3.2 Pressure Calculation

The problem of understanding the relationship between pressure and rotor deceleration can be simplified by assuming that gas molecules leaving a smooth adsorbate-covered metal surface, like that of the SRG rotor, do it so isotropically [42]. As a consequence, on average their linear momentum has no impact on the angular momentum of the rotor and thus these outgoing molecules don't need to be considered in the calculation.

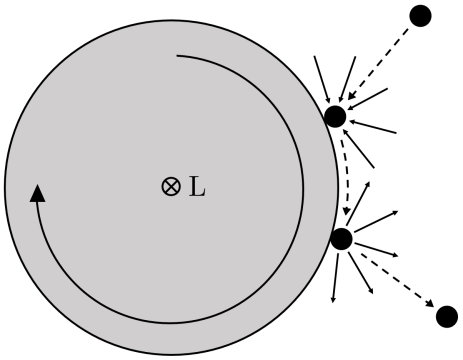

Figure 3.6: Diagram of a collision of a molecule with the SRG rotor rotating clockwise with perfect momentum accommodation. In a molecular regime the incoming molecules collide from any angle, adding their mass to the rotor's moment of with a practically diffuse rebound.

The same is not quite true for incoming molecules. On the one hand it's also possible to ignore their linear momentum by assuming that an isotropic velocity distribution in the gas results in the cancellation of the tangential component of the incoming molecule's velocity. On the other hand, the collisions have practically perfect momentum accommodation, which in a sense means that each of these molecules will adhere to the surface for a brief moment long enough to be accelerated by it. Given that the average initial tangential velocity of the molecules is zero, they get accelerated from zero to the rotor's surface velocity acquiring the respective angular momentum L from the rotor.

$$L = I\omega \tag{3.1}$$

I being the molecule's moment of inertia, and ω the rotor's angular frequency, which on average is the same as the molecule's after the collision.

With the molecules being treated as point masses of mass m, their moment of inertia I while spinning around an axis with distance d is md^2, resulting in the following change in momentum for the rotor for each molecule collision.

$$\Delta L = -md^2\omega \tag{3.2}$$

The loss of angular momentum from the rotor will be proportional to the collision rate of the gas by unit area.

$$f = \frac{2p}{\pi m\bar{c}}\,\mathrm{d}A \tag{3.3}$$

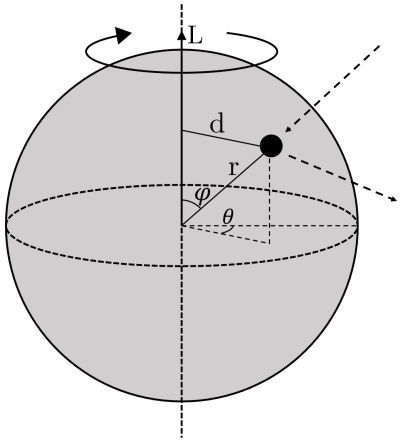

Figure 3.7: Diagram of a collision of a molecule with the rotor.

Where f is the number of collisions per second in a surface element area dA, where p is the pressure and $\bar{c}$ is the average molecular speed.

By multiplying the change of angular momentum per collision (equation 3.2) with the collision frequency (equation 3.3) an expression of the loss of the variation of angular momentum per time unit is obtained.

$$\Delta\dot{L} = -md^2\omega\frac{2p}{\pi m\bar{c}}\,\mathrm{d}A \tag{3.4}$$

By taking the infinitesimal limit, the previous expression turns into one of the time derivative of the angular momentum:

$$\dot{L} = -\int \frac{2pd^2\omega}{\pi\bar{c}}\,\mathrm{d}A \tag{3.5}$$

This is the loss rate of angular momentum of the rotor due to the collisions with gas molecules. Additionally, the angular velocity of the rotor is also calculated from equation 3.1.

$$I\dot{\omega} = -\int \frac{2pd^2\omega}{\pi\bar{c}}\,\mathrm{d}A$$

$$-\frac{\dot{\omega}}{\omega} = \frac{2p}{I\pi\bar{c}}\int d^2\,\mathrm{d}A \tag{3.6}$$

This last equation 3.6 is the most generic solution to the problem at hands. From here, information specific to the geometry of the rotor is necessary to proceed with the calculations.

In the case of the SRG, the rotor is a sphere. Knowing that for a sphere, the element area $\mathrm{d}A$ is equal to $r^2 sen(\phi)\,\mathrm{d}\phi\,\mathrm{d}\theta$ in spherical coordinates.

$$-\frac{\dot{\omega}}{\omega} = \frac{2p}{I\pi\bar{c}}\int_o^{2\pi}\int_0^{\pi} d^2r^2\sin(\phi)\,\mathrm{d}\phi\,\mathrm{d}\theta \tag{3.7}$$

Assuming the axis of rotation as being the vertical axis passing through the center of the sphere, the distance of the collisions from the axis of rotation, d, is the distance of the vertical axis from each point of the surface.

$$d = r\sin(\phi) \tag{3.8}$$

Substituing the integral yields

$$-\frac{\dot{\omega}}{\omega} = \frac{2p}{I\pi\bar{c}} \int_{o}^{2\pi} \int_{0}^{\pi} r^4 \sin^3(\phi)\, \mathrm{d}\phi\, \mathrm{d}\theta$$

$$-\frac{\dot{\omega}}{\omega} = \frac{pr^4}{I\bar{c}} \frac{16}{3} \tag{3.9}$$

Finally, the moment of inertia I can be replaced by the respective expression for an homogeneous sphere, $(2/5)mr^2$. Nevertheless, it is more convenient to write the mass m in terms of geometric dimensions and density of the material, i. e. by definition $m = V\rho$ where ρ is the density and V is the spheric volume of the rotor $(4/3)\pi r^2$.

$$I = \frac{8\pi}{15} r^5 \rho \tag{3.10}$$

In turn, this substitution gives place for the final expression used to calculate the pressure from SRG's rotor relative deceleration rate.

$$-\frac{\dot{\omega}}{\omega} = \frac{10p}{\pi r \rho \bar{c}} \tag{3.11}$$

This deduction is based on the assumption that there is total momentum accommodation per molecule collision. Although this is very close to reality, there are small deviations that differ from rotor to rotor. To take this fact into account, a parameter σ is multiplied on the right-hand side of the equation 3.11. Its value is usually close to one, but can be higher or lower depending on the rotor's roughness.

3.2.1 Relative Deceleration Rate Evaluation

Moving forward, a disclaimer is necessary towards the interchangeability of the angular frequency and the frequency of the rotor in this context. Despite being fundamentally different, since one is measured in rad/s and the other in Hz or s^{-1}, the relative rate of change of this quantities in this system is the same. In other words the angular frequency ω and its derivative $\dot{\omega}$ could be substituted by the frequency of the rotor f_{rot} and its derivative $\dot{f_{rot}}$, respectively, in equation 3.11 and the expression would still be accurate. For this reason, in the literature and in this dissertation, the expressions angular frequency and frequency are used interchangeably.

However, in practice the actual quantity measured is the time needed for the rotor to complete a predefined number of turns, τ, which is related to the angular frequency by the equation $\omega = 2\pi n/\tau$, if n represents the number of rotations accounted in the time interval τ. It is important to convey the impossibility that is to make instantaneous measurements of a time-dependent variable change rate. For this reason, the ideal infinitesimal quantity has to be approximated by a finite one.

$$-\frac{\dot{\omega}}{\omega} \approx -\frac{\Delta\omega}{\omega\Delta t} = \left|-\frac{\dot{\omega}}{\omega}\right|_{av} \tag{3.12}$$

Two measurements of τ are made for each calculation of the relative deceleration rate.

$$-\frac{\omega_j - \omega_i}{\omega_i}\frac{1}{\Delta t} = \frac{\tau_j - \tau_i}{\tau_j}\frac{1}{\Delta t} \tag{3.13}$$

If the measurement of τ_j follows exactly after the measurement of τ_i, then is reasonable to consider the time interval Δt between the two measurements to be τ_i, since it is the time that takes from the start of the first measurement to the start of the second.

$$\left|-\frac{\dot{\omega}}{\omega}\right|_{av} = \frac{\tau_j - \tau_i}{\tau_j \cdot \tau_i} \tag{3.14}$$

However, there is another way to think about it that takes advantage of the fact that the deceleration rate is very small. In one of Beams' levitation systems [31] a sphere of 1.59 mm in diameter spinning freely at about 120 000 r.p.s. in a pressure of 1.33×10^{-5} mbar would take two hours to lose 1% of its rotation speed.

In these conditions, where $\Delta\tau \ll \tau$, it is safe to assume that $\tau_i \approx \tau_j \approx \tau$.

$$-\frac{\Delta\omega}{\omega}\frac{1}{\Delta t} = \frac{\Delta\tau}{\tau}\frac{1}{\Delta t} \tag{3.15}$$

Although the calculation has to be made with τ_i and τ_j. To this end, τ may be best estimated by taking the mean value of both measurements.

$$\left|-\frac{\dot{\omega}}{\omega}\right|_{av} = \frac{2(\tau_j - \tau_i)}{(\tau_j + \tau_i)}\frac{1}{\Delta t} \tag{3.16}$$

A nice perk of this equation is that it doesn't require consecutive measurements, which is made possible by the Δt term that takes into account the time elapsed between the two measurements τ_i' and τ_j'. Nevertheless, if the measurements are still made consecutively, Δt becomes equal to τ and the equation simplifies.

$$\left|-\frac{\dot{\omega}}{\omega}\right|_{av} = \frac{4(\tau_j - \tau_i)}{(\tau_j + \tau_i)^2} \tag{3.17}$$

These three solutions (equations 3.14, 3.16 and 3.17) were used by Fremerey in 1984 [42]. They provide a practical way to evaluate the rotor's relative deceleration rate from time intervals. However, a typical intrinsic time jitter $\delta t = 0.5\mu s$ in the measurement is expected to introduce an uncertainty of the order of 1 Hz at a frequency of 400 Hz, which is quite significant. The way to tackle this variation is to average several measurements over time, meaning that the user has to settle with a trade off between the precision of the measurement and the rate at which the measurements are made.

Some degree of averaging is already happening in the above expressions, given the fact that the time period τ takes a predefined number of turns to measure, thus representing the average angular frequency during that period. Still, there is going to be some degree of scatter in the final pressure reading which can be attenuated by more advanced averaging methods.

In figure 3.8 the horizontal line represents the SRG's output frequency signal, with the vertical pulses representing successive rotor turns in time, separated by a time interval tau_0. In this case, 10 turns are included in each *tau* measurement.

The simplest way to perform the calculation would be measuring consecutive τ periods, and use the equation 3.14 or 3.16 to calculate a new value of pressure for every pair of τ periods.

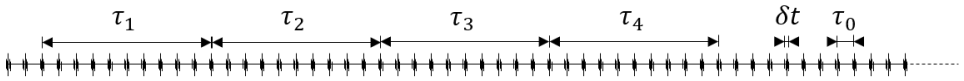

Figure 3.8: Simple frequency averaging [42].

In the example, τ_1 and τ_2 would be used for one $-\dot{\omega}/\omega$ calculation, and τ_3 and τ_4 for another, which is far from optimal since the instrument will only have one pressure reading every 2τ period, and it will still be heavily affected by the signal scatter, identified in the figure by δt.

One way to address the output rate is to have several measurements in parallel every time, something that Fremerey labelled multi-track multiperiod averaging, or MMA for short [42].

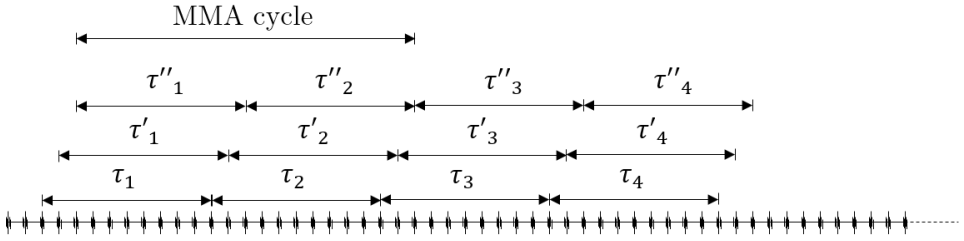

Figure 3.9: Multiple-track multiperiod averaging method [42].

Theoretically, this method could wield one new value for each turn. However, the instrument response time is the same since truly independent measures would still only

be available every 2τ seconds, like before.

Until now, every example has been given with successive measurements in mind, but through the use of the equation 3.16 one can measure τ periods spaced Δt seconds in the time line, and the same reasoning applies.

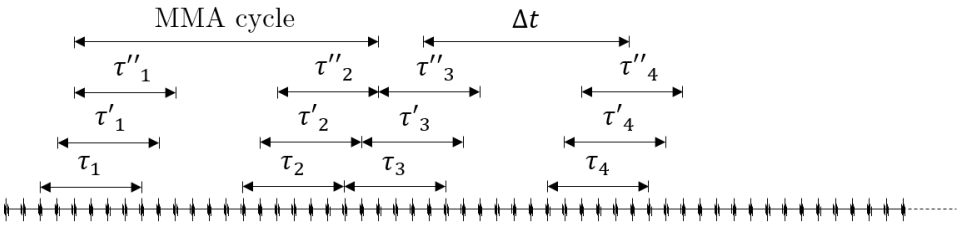

Figure 3.10: Multiple-track multiperiod averaging method with time separation Δt [42].

Up until this point, the only averaging made was a direct consequence of the fact that the frequency was taken as the mean value over the number of turns accounted in every τ period. To reduce the scattering even further, Fremerey proposed a new cycle calculated from the sum of the various τ_i and τ_j of dependent MMA cycles. In both figures 3.9 and 3.10, the MMA cycle calculated from τ_1 and τ_2 wields a value that is dependent from the τ_1' and τ_2' cycle, but is in fact independent from the τ_3 and τ_4 cycle.

The sum of every $\tau_i + \tau_i' + \tau_i'' \cdots \tau_i^n$ and $\tau_j + \tau_j' + \tau_j'' \cdots \tau_j^n$ are then used to calculate the pressure value. Fremerey called this averaging mode AMA for accumulated multiperiod averaging.

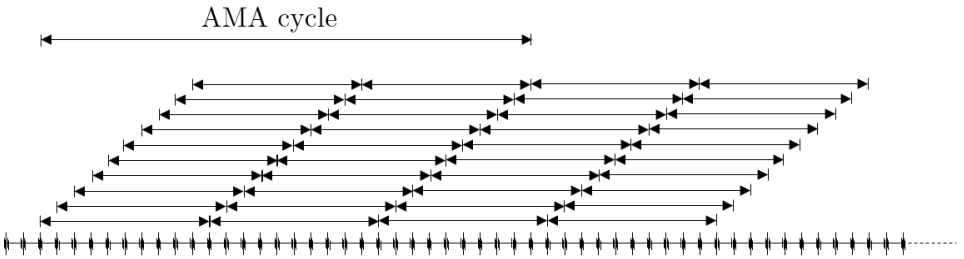

Figure 3.11: Accumulated multiperiod averaging [42].

Again, this is also applicable to separated measurements.

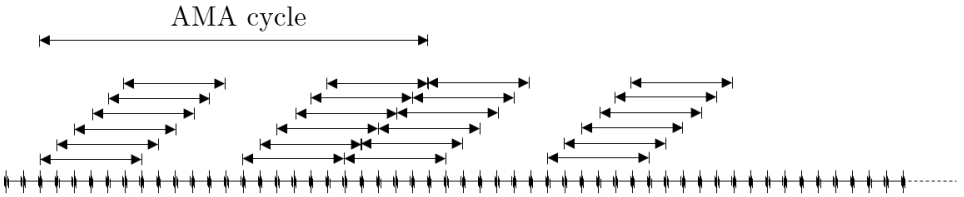

Figure 3.12: Accumulated multiperiod averaging with time separation [42].

In the examples pictured in the figures 3.11 and 3.12 a full independent AMA cycles occurs every 29 turns and 23 turns respectively, increasing the instrument's response time, and reducing the output scatter by a factor of the root of the number of turns included in

the period τ, which in this case would be $\sqrt{10}$ and $\sqrt{6}$, respectively although, like before, dependent new readings can be made every new turn.

The reproducibility can be quite significantly improved by the AMA method over the MMA method. Ultimately, it comes down to the compromise between the accuracy of the measurement and the response time of the instrument.

3.3 Drag Sources and SRG's limitations

The drag felt by the rotor is due to several different phenomena. Typically, the most dominant source is the gaseous drag, but as the pressure goes lower, a residual drag starts to emerge. The pressure level where this effect starts to dominate is usually the lower limit of the gauge's operating range. For reference, in Fremerey's SRG this residual drag was equivalent to the gaseous drag of a 10^{-6} mbar vacuum [42].

Isogai studied in 1997 some of the most relevant drag sources [47]. According to his work, there are three main sources for error in the measurement of the SRG's drag: temperature, electrostatic force (or Coulomb force as Isogai refers to it) and eddy currents.

$$\left(\frac{\dot{\omega}}{\omega}\right)_{\text{total}} = \left(\frac{\dot{\omega}}{\omega}\right)_{\text{gas}} + \left(\frac{\dot{\omega}}{\omega}\right)_{\text{eddy currents}} + \left(\frac{\dot{\omega}}{\omega}\right)_{\text{temperature}} + \left(\frac{\dot{\omega}}{\omega}\right)_{\text{electrostatic force}} \tag{3.18}$$

Temperature error can be troublesome for two reasons: because the temperature is included in the equation of the relative deceleration rate in the gas mean thermal velocity (equation 3.11), but also because it affects the rotor's dimensions and thus its moment of inertia by thermal expansion although it can generally be controlled by keeping the room's temperature constant. The electrostatic force is exerted on the center of mass of the rotor and therefore is time-independent. Both these forces are responsible for an offset in the pressure reading but are not too difficult to account for in the final reading. Whereas eddy currents induced by the rotating component of the rotor's magnetic field in the surrounding parts of the instrument, and by external magnetic fields in the rotor itself, are more strictly tied to the residual drag and thus to the low pressure range limitations of the instrument.

Isogai concluded that the deviation due to eddy currents was up to 10 times bigger than the deviation due to thermal effects temperature. Being the measured residual dragg, shown in figure 3.13, roughly equivalent to a pressure of the order or 10^{-7} mbar. Other culprits for the residual dragg have been identified, like asymmetries in the magnetic field or imperfections in the rotor, which would result in an unequal moment of inertia.

Nevertheless, decaying time constants of 10 years have been previously achieved [1], meaning that there is so little dragg that more subtle fundamental phenomena get to meaningfully impact the system's performance. Keith proposed that the Coriolis effect due to the earth's rotation would have a significant impact in the residual dragg [1]. His predictions would later be confirmed by Fremerey's experimental results [2, 48, 49], and ending up representing an equivalent pressure of 10^{-9} mbar.

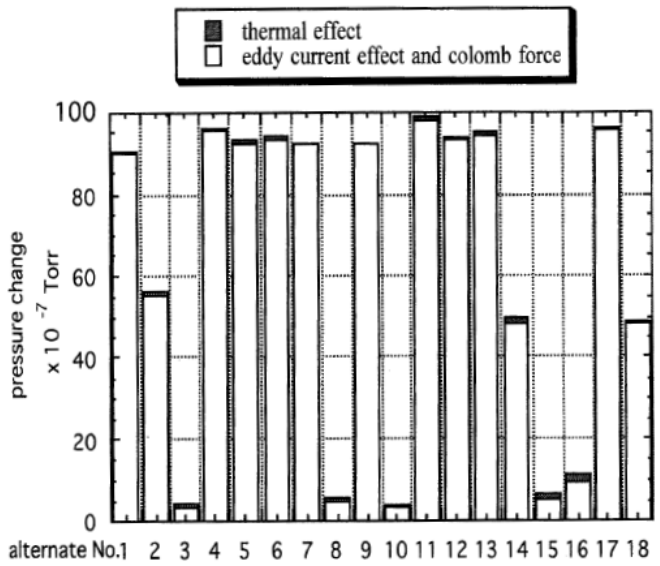

Figure 3.13: Isogai's results from 18 independent measurements comparing eddy current plus electrostatic force with thermal effects in the SRG output.

Keith also predicted a gravitational radiation effect as a dragg source based on Birkhoff's theory of gravitation, with an equivalent pressure of the order of 10^{-12} mbar. Although with little certainty, Fremerey's results agreed with Keith's predictions [49], but his predictions also met some criticism [50].

On the other hand, there is also a high pressure limit for which the equation 3.11 starts to fail. This happens when the pressure rises above the molecular regime, which for Fremerey's SRG would start to happen for pressures above 10^{-2} mbar.

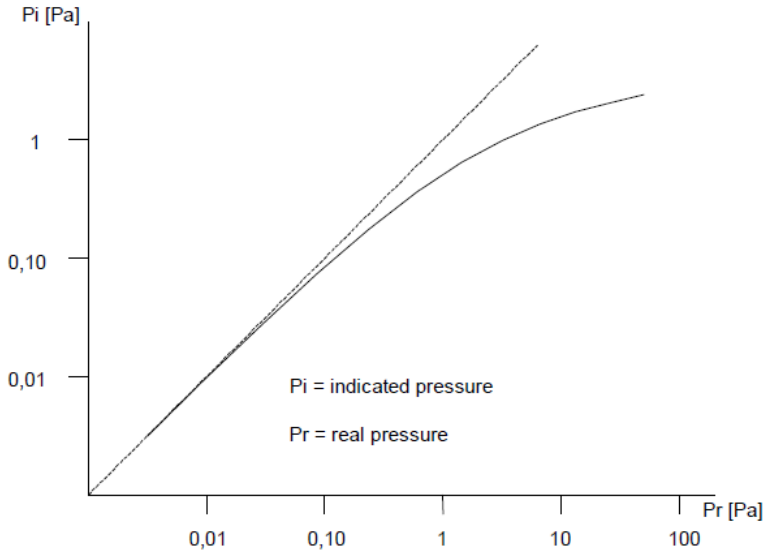

Figure 3.14: Non-linearity curve for higher pressures [51].

However, despite not being linear, the pressure reading can be corrected. Even though

the rotor gets very susceptible to thermal errors, due to the increased friction with the gas and the fact that the saturation effect reduces the slop of the plot, which implies an increased measurement uncertainty.

Commercial units are able to correct these effects up to 1 mbar [51], associated with an increase in the uncertainty that reaches 10%. Although theoretically the linearisation of the pressure reading can be taken even further, provided that adequate thermal control methods are used [42].

CHAPTER 4

THE CHALLENGE OF LOW PRESSURE MEASUREMENT

Vacuum technology operates in a range of over 15 orders of magnitude, as shown in table 4.1. Therefore, there is not one single device that works for every pressure level in vacuum generation or measurement. As a consequence, vacuum pressure is usually divided in several ranges according to the technological requirements to produce or measure it.

Table 4.1: Pressure categories according to the United Kingdom's National Measurement Institute [52].

Type of Vacuum	Pressure Range (Pa)
low vacuum	$10^5 - 3 \times 10^3$
medium vacuum	$3 \times 10^3 - 10^{-1}$
high vacuum	$10^{-1} - 10^{-4}$
very high vacuum	$10^{-4} - 10^{-7}$
ultra-high vacuum	$10^{-7} - 10^{-10}$
extreme ultra-high vacuum	$< 10^{-10}$

Note that this is just an example, as there is not one universally accepted method to classify vacuum pressure, and that another source could have a different classification system.

Despite the fact that this classification is mostly based on technological limitations, as shown in figure 4.1, when it comes to measure vacuum pressure there is a more fundamental separation between the methods employed. The different techniques are either direct or indirect. This is important because in the former the measured quantity is pressure itself, contrasting with the latter where a different property of the system is measured, and by knowing some additional parameters of the system in question, the pressure can be deduced.

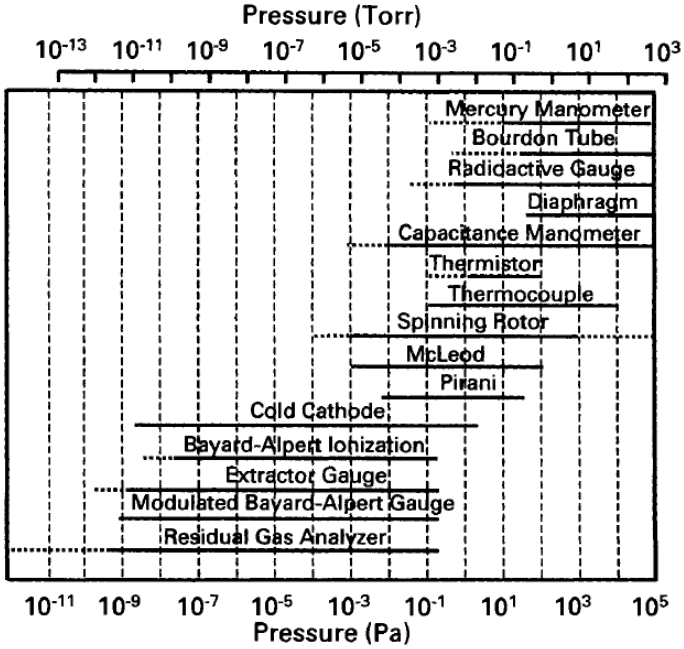

Figure 4.1: The pressure range of several manometers [53].

4.1 Direct Pressure Measurement

Direct methods make use of instruments that by definition measure the force the gas exerts in a certain area, i.e. they measure pressure directly. This force can be translated into a mechanical displacement as can be seen in figure 4.2, where a capacitance manometer is represented with a mobile diaphragm. This diaphragm will move according to the pressure difference between P_X and P_R, and by knowing the reference pressure P_R it is possible to know the value of P_X.

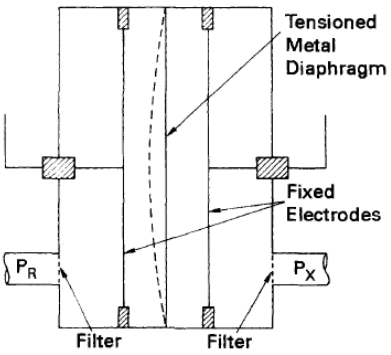

Figure 4.2: Double-sided capacitance manometer [53].

Other examples of direct instruments are mercury columns, Bourdon or McLeod gauges. Ideally, this would be the only way used to measure pressure, but unfortunately these methods only apply to pressures over 1 mbar (except for the McLeod that can reach

10^{-6} mbar). Measurements under this value become very difficult due to instrument limitations, since the primary signal is always somewhat related to movement and therefore vulnerable to error sources like vibrations and hysteresis, among others.

4.2 Indirect Pressure Measurement

On the other hand, indirect methods rely on theoretical relationships between pressure and other more easily measurable variables. The knowledge of the various parameters of the system involved in these relationships allow the measured variable to be converted into a pressure reading. Example of these variables are thermal conductivity, ionization probability or coefficient of friction, each of these spanning their own range of instruments and methods.

As an example, thermal conductivity gauges take advantage of the fact that a filament's resistance change with its temperature, which in this case is used as an indication of the heat transfer between a hot filament and its surroundings. In low pressures, the heat dissipation depends on the pressure since the amount of molecules available to absorb thermal energy is limited. However, different molecules have different heat capacities and consequently the pressure dependence on thermal conductivity has to account for the nature of gas being measured.

This requirement is the most significant disadvantage of these gauges, since the molar mass of the residual gas is of fundamental importance across all indirect methods. Although they are usually calibrated for air and can be calibrated for different gases, they can be problematic when dealing with an unknown residual gas.

The spinning rotor gauge is also an indirect method, as it will be further explained.

4.3 Calibration in the Low Pressure Range

Since no instrument operates on the whole spectrum of low pressures, the primary standard used for calibration will depend on the targeted pressure range. Therefore, calibration is carried by two different methods: direct comparison and static or continuous expansion.

Down until 1 mbar, the pressure can be directly measured by mercury columns with low uncertainty. In these circumstances, direct comparison is sufficient for the calibration of an unknown gauge against a standard. It is possible to go even further to 10^{-6} mbar with the compression provided by a McLeod gauge.

For lower pressures, static expansion is used to produce a well known pressure. If temperature is kept constant, this expansion can be described by Boyle's law.

$$P_1 V_1 = P_2 V_2 \tag{4.1}$$

If all the necessary conditions are met, one can start with a well-known pressure and expand it to a known volume to achieve a much lower well-known pressure, depending

on the volume ratio of the expansion. Additionally, the process can be repeated several times in order to achieve even lower pressures.

Despite being very simple from a theoretical standpoint, the static expansion method constitutes a great technical challenge. The residual pressure on the expanding volume prior to the expansion has to be exceptionally low, and even then there is the problem of outgassing of the chamber walls. Since this process requires closed volumes, the outgassing will increase the pressure over time. One way to deal with this problem is to measure this effect and account for it in the data analysis, another way is to allow the initial volume to expand itself in a way that keeps the pressure constant. Either way these systems can produce pressures from 10 to 10^{-10} mbar, and are claimed to be the most precise methods [54].

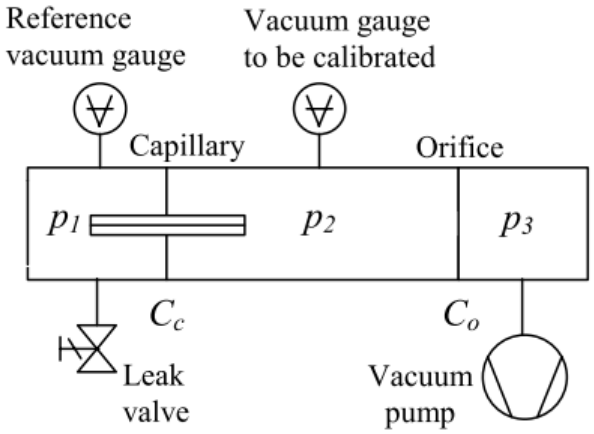

Figure 4.3: Example of a continuous expansion calibration apparatus [55].

The continuous expansion method is also able to avoid some of these problems, as shown in figure 4.3. It consists of a chamber with a well-known pressure p_1 connected to a calibration chamber, with pressure p_2, by a known flow rate C_c, which in turn is connected to a vacuum pump with known flow rate C_o and pumping speed. Since it is being pumped, the system will reach an equilibrium from which is possible to calculate the pressure in the calibration chamber. There is also the outgassing of the walls to consider, but since this method is dynamic, and does not rely on closed volumes, it is not nearly as troublesome.

4.4 The Spinning Rotor Gauge in Vacuum Technology

The spinning rotor gauge has long found its place among vacuum gauges, and has become the instrument of choice to be a calibration standard for other indirect gauges in its operation range, which attest its stability and accuracy.

Fremerey argues in his SRG proposal paper [42] that given that it is theoretically possible to trace the relative deceleration rate of the rotor down to fundamental quantities like mass, length, time and other well defined quantities that require no calibration, this instrument can be regarded as an absolute gauge.

Although this is possible, in practice it is hardly the case. The roughness of the rotor's surface introduces enough uncertainty to justify the need of an additional σ parameter in the pressure equation 3.11, and all the effects explored in section 3.3 end up contributing for it to be an indirect pressure gauge.

It is also necessary to consider the nature of the measured gas. The thermal velocity of the molecules of the gas used in the pressure equation 3.11 depend on the mass of the molecules, and therefore on the composition of the gas. For example, to measure gas mixtures, it is necessary to know the resulting relative molecular masses. Which for n gases in a mixture is calculated in the following way [51].

$$M_{res} = a_1\sigma_1\sqrt{M_1} + a_2\sigma_2\sqrt{M_2} + \cdots a_n\sigma_n\sqrt{M_n} \tag{4.2}$$

Where a is the relative proportion of each gas in the total mixture and σ the respective different momentum accommodation factors. Which means that the SRG can only operate as an absolute gauge as long as there is perfect information about the nature of the vacuum's residual gas.

For all these reasons in practice the SRG has to be calibrated and is used as an indirect gauge.

Nevertheless, the SRG has an impressive amount of advantages. It is an incredibly stable gauge, with and annual drift inferior to 1%, making it an ideal standard for calibration. Its mode of operation doesn't have secondary effects in the measured gas like pumping, thermal or ionization effects. And commercial units have an extensive operation range that can go from 5×10^{-7} to 1 mbar, which is theoretically possible to extend even further. From all its specifications, probably the only disadvantage is the reading rate that can be as low as two readings per minute for good accuracy.

All this characteristics set this gauge apart from all the others, making it extremely interesting.

CHAPTER 5

THEORETICAL CONSIDERATIONS CONCERNING THE ROTOR

For future work, it's important to understand the impact of the different properties of the rotor in the performance of the SRG.

The higher the deceleration rate of the rotor, the faster and more accurate the pressure reading will be. Therefore, any parameter change that could increase the deceleration rate would potentially improve the instrument, if the change is within the technological limitations.

Here, the main focus is on the rotor's shape, dimensions and density. But others may be considered like magnetic permeability, electrical resistivity or thermal expansion coefficient.

One can assume that the larger the area of interaction of the rotor with the gas, the higher the number of collisions will be and therefore the higher the deceleration rate response. However, for regular solid rotors like a cylinder or a sphere, the increase in surface area implies an increase in volume, in turn increasing the moment of inertia which has a negative impact in the rotor deceleration. Since the volume scales with the cube of the dimensions where the area scales with the square, as a rule of thumb the bigger the rotor the weaker will be its deceleration response to pressure variation.

The general equation 3.6 from section 3.2 provides the perfect starting point for this geometry-focused discussion.

$$-\frac{\dot{\omega}}{\omega} = \frac{2p}{I\pi\bar{c}} \int d^2 \, \mathrm{d}A$$

In the equation, these parameters are taken into account by the surface integral and by

the moment of inertia, I.

$$I = \int \rho(\boldsymbol{x}) d^2 \, \mathrm{d}V \tag{5.1}$$

Being $\rho(\boldsymbol{x})$ an non-homogeneous density dependent on the the position vector $\boldsymbol{x}$, and d the already mentioned distance to the spinning axis.

$$-\frac{\dot{\omega}}{\omega} = \frac{2p \int d^2 \, \mathrm{d}A}{\pi \bar{c} \int \rho(\boldsymbol{x}) d^2 \, \mathrm{d}V} \tag{5.2}$$

If, for a first analysis, the density is assumed homogeneous ($\rho(\boldsymbol{x}) = \rho$), the problem gets simplified.

$$-\frac{\dot{\omega}}{\omega} = \frac{2p \int d^2 \, \mathrm{d}A}{\pi \bar{c} \rho \int d^2 \, \mathrm{d}V} \tag{5.3}$$

$$-\frac{\dot{\omega}}{\omega} = \frac{2p \int d^2 \, \mathrm{d}A}{\pi \bar{c} \rho \int \int d^2 \, \mathrm{d}A \, \mathrm{d}r} \tag{5.4}$$

r being the rotor's radial direction along which the area integral can be integrated for the volume, i.e. $dV = dAdr$.

As expected, the density increases the moment of inertia thus reducing the deceleration. Besides, the surface integral is present in both numerator and denominator, but is further integrated along the volume in the latter, confirming that for regular solids increasing the rotor's surface by increasing its size is counterproductive given that the moment of inertia increases with the volume.

5.1 Pressure Calculation With a Cylinder Rotor

The pressure is calculated in a similar way as it was explained in section 3.2, but some tinkering is necessary to adapt the solution from a spherical rotor to a cylindrical one. For a cylinder the same reasoning applies until equation 3.6, which is the most generic solution. Then, a cylindrical geometry is considered in the calculation of the integral.

$$-\frac{\dot{\omega}}{\omega} = \frac{2p}{I\pi\bar{c}} \left(2 \int_0^{2\pi} \int_0^{r} d^2 r \, \mathrm{d}r \, \mathrm{d}\theta + \int_0^{h} \int_0^{2\pi} d^2 r \, \mathrm{d}\theta \, \mathrm{d}z \right) \tag{5.5}$$

For a cylinder rotor, the distance d is equal to the cylinder's radius.

$$-\frac{\dot{\omega}}{\omega} = \frac{2p}{I\pi\bar{c}} \left(2 \int_o^{2\pi} \int_0^{r} r^3 \, \mathrm{d}r \, \mathrm{d}\theta + \int_0^{h} \int_0^{2\pi} r^3 \, \mathrm{d}\theta \, \mathrm{d}z \right)$$

$$-\frac{\dot{\omega}}{\omega} = \frac{2p}{I\pi\bar{c}} \left(\pi r^4 + 2\pi h r^3 \right)$$

$$-\frac{\dot{\omega}}{\omega} = \frac{2pr^3}{I\bar{c}} \left(r + 2h \right) \tag{5.6}$$

Given that for a cylinder the moment of inertia is $\frac{1}{2}mr^2$.

$$-\frac{\dot{\omega}}{\omega} = \frac{4pr}{m\bar{c}}(r+2h)$$

By definition, the mass m is equal to $V\rho$, where V is the volume and ρ is the density. Additionally, the volume of the cylinder is $V = \pi r^2 h$. With all things considered, the following result is obtained.

$$-\frac{\dot{\omega}}{\omega} = \frac{4p}{\pi r\rho\bar{c}}\left(\frac{r}{h}+2\right) \tag{5.7}$$

All this reasoning is based on the assumption that there is perfect momentum accommodation in every molecule collision. Despite being close to reality, every rotor's surface is different and not ideal. To compensate for this difference, an accommodation factor σ has to be considered.

$$-\frac{\dot{\omega}}{\omega} = \frac{4p\sigma}{\pi r\rho\bar{c}}\left(\frac{r}{h}+2\right) \tag{5.8}$$

The equation 5.8 is analogous to the equation 3.11 of the traditional SRG, and was used to calculate the pressure from the deceleration rate.

5.2 Cylinder vs. Sphere

Let D_s be the relative deceleration rate of a sphere and D_c the relative deceleration rate of a cylinder. From equation 3.11 it follows

$$D_s \equiv \left|-\frac{\dot{\omega}}{\omega}\right|_s = \frac{10p\sigma}{\pi r_s\rho\bar{c}} \tag{5.9}$$

and from equation 5.8:

$$D_c \equiv \left|-\frac{\dot{\omega}}{\omega}\right|_c = \frac{4p\sigma}{\pi r_c\rho\bar{c}}\left(\frac{r_c}{h_c}+2\right) \tag{5.10}$$

Since the focus here is on the impact of these geometries, its possible to group all the non geometry related parameters under a constant K.

$$K = \frac{p\sigma}{\pi\rho\bar{c}} \tag{5.11}$$

And then apply this simplification to both equations 5.9 and 5.10.

$$D_s = \frac{10K}{r_s} \tag{5.12}$$

$$D_c = \frac{4K}{r_c}\left(\frac{r_c}{h_c}+2\right) \tag{5.13}$$

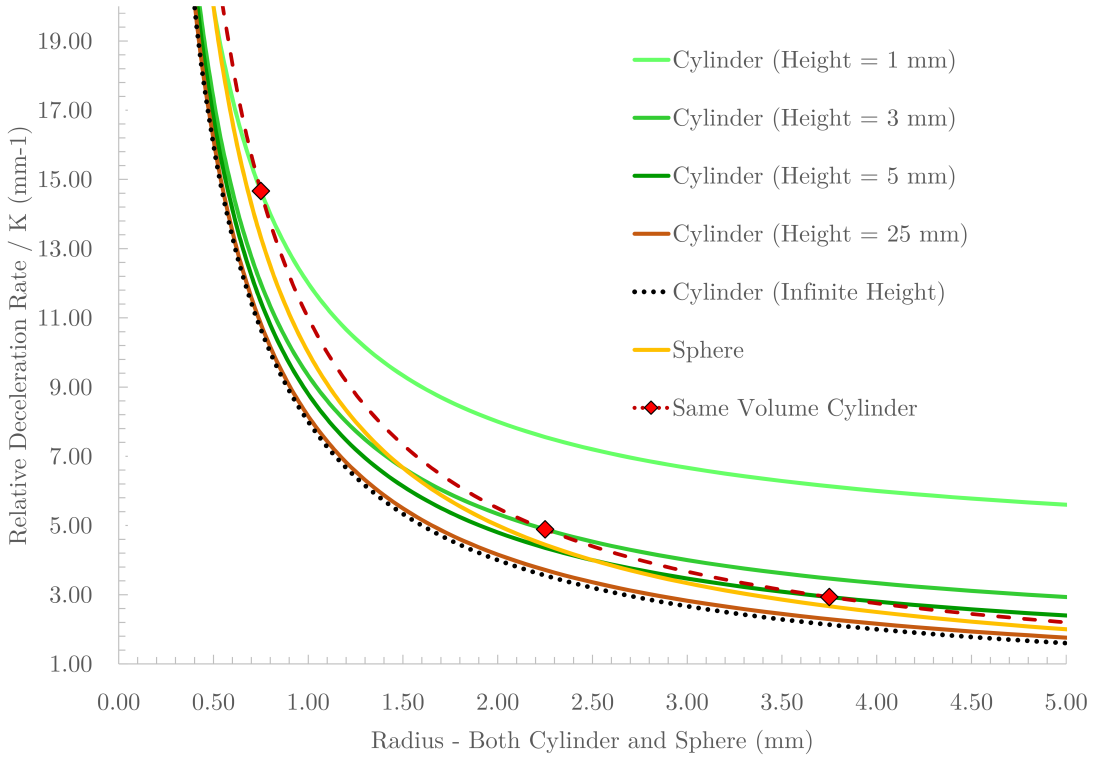

Figure 5.1: Relative deceleration rate (in mm^{-1}) comparison of a sphere and cylinders of different heights, where the radii at which the volume of each cylinder is the same as the sphere's is identified by the red marks and the red dashed line marks the respective trendline.

Geometrically the deceleration rate of the sphere only depends on the sphere's radius r_s, making it easy to plot. On the other hand, the deceleration rate of the cylinder depends on the cylinder's radius r_c and its height h_c.

Different cylinder geometries are compared with the sphere's deceleration in figure 5.1. It is possible to observe that as the height of the cylinder increases, the respective deceleration curves approach the infinite height curve, meaning that an infinitely high cylinder still has a deceleration rate. This behaviour is expected, and can be calculated by taking the limit when h_c tends do infinite in equation 5.13.

The most interesting conclusion from this plot is that for small enough radius, the sphere has a higher deceleration rate than the cylinder. This results from the fact that the sphere's curve has a steeper slope than any cylinder curve as the radius tends to zero. Yet, as the radius increase, cylinder rotors start to perform better than the spherical one, since the sphere curve tends to zero faster as the radius increase.

Furthermore, a red cross in each cylinder curve marks the radius at which the cylinder and the sphere have the same volume. The volume is a relevant parameter since it is related to the eddy current production. Ohmic losses on the rotor by eddy currents are

calculated by integrating the ohmic loss density across the rotor volume [36].

$$P_{EC} = \int_0^{2\pi}\int_0^{\pi}\int_0^{r} \frac{1}{\gamma}\mathbf{J}^2\, r^2 \sin\theta \,\mathrm{d}r\,\mathrm{d}\theta\,\mathrm{d}\phi \tag{5.14}$$

P_{EC} J γ

In this respect, it is interesting to note that figure 5.1 shows that for equal volumes and radii, the cylinders always preform better than the sphere. Nonetheless, this comparison is incomplete given that it only compares geometries with the same radius.

To allow a better comparison, another approach may be used. Here, the deceleration rate of the cylinder (equation 5.13) is divided by the deceleration rate of the sphere (equation 5.12).

$$\frac{D_c}{D_s} = \frac{4r_s}{10r_c}\left(\frac{r_c}{h_c} + 2\right) \tag{5.15}$$

The result depends on three variables: r_s, r_c and h_c. To simplify, the volume of both geometries is made to be equal since eddy currents are related to the rotor's volume.

$$\frac{4}{3}\pi r_s^3 = h_c \pi r_c^2 \tag{5.16}$$

Now the question is how differently will both rotors perform for different rotor sizes, but having the same volume. For this reason, the ratio between radii is the variable used to make this comparison.

$$r_c = x r_s \tag{5.17}$$

Substituting r_c in the volume equality 5.16 results in:

$$h_c = \frac{4}{3}\frac{1}{x^2} r_s \tag{5.18}$$

Basically, this last expression defines the cylinder's height in such a way that both rotors have always the same volume. Now, r_c and h_c can be replaced in equation 5.15.

$$\frac{D_c}{D_s} = \frac{4}{10}\frac{r_e}{x r_e}\left(\frac{x r_e}{\frac{4}{3x^2} r_e} + 2\right) \tag{5.19}$$

$$\frac{D_c}{D_s} = \frac{3}{10}x^2 + \frac{4}{5x} \tag{5.20}$$

This last expression is plotted in figure 5.2 where it is possible to verify that the cylinder always outperforms the sphere for a given volume. Although the difference is not that substantial for similar radius, which is also the case in figure 5.1 where the red dashed line marks the same-volume curve and for which the deceleration is slightly higher than that of the sphere. Actually, the figure 5.1 was built assuming that $r_s = r_c$, meaning that same volume red dashed curve and the sphere's curve have a proportionality constant of 1.1 which is the D_c/D_s value in figure 5.2 for $r_c/r_s = 1$.

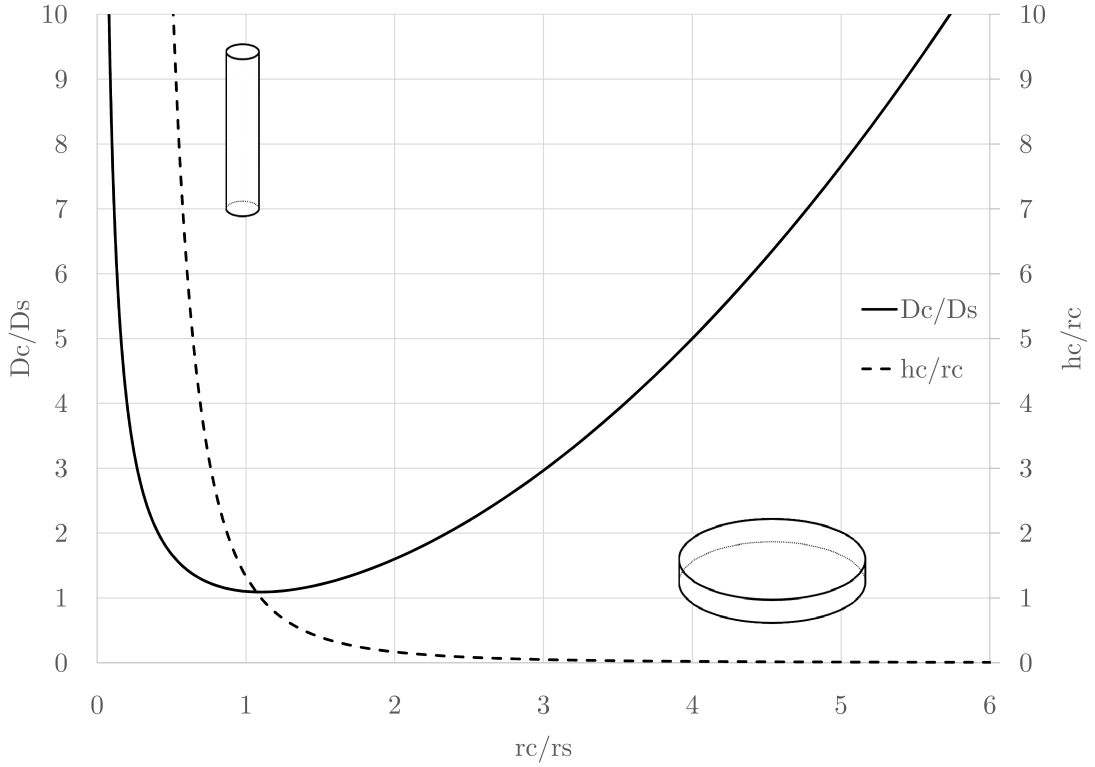

Figure 5.2: The ratio between deceleration rates of the cylinder D_c and the sphere D_s, for a given ratio of cylinder radius r_c over the sphere radius r_s. Where the heigh of the cylinder is defined as to keep the volume of the cylinder equal to the sphere's by equation 5.18.

5.3 Other Properties

The geometry of the rotor has a central role in defining its deceleration rate. Not only does it define the surface of interaction between the rotor and the gas, and the rotor's moment of inertia, but it also affects other properties.

5.3.1 Resistivity

The previously seen eddy current production is one of such properties, since it occurs throughout the rotor's volume. This means that the smaller the volume, the lower the eddy current production will be and thus the lower will be the low pressure limit of the device.

Another way to reduce the production of eddy currents would be to use a material with higher resistivity. A typical stainless steel has a resistivity of $6.9 \times 10^{-7} \Omega \cdot m$ which makes it a poor conductor when compared with the resistivity of the copper with $1.68 \times 10^{-8} \Omega \cdot m$, but a conductor nonetheless.

The production of eddy currents could be minimized with the use of a high resistance

magnetic material, such as ferrite ceramics that are non conducting ferromagnetic materials. A similar approach would be to use a rotor with interpolated layers like the magnetic circuits of electric transformers where losses by eddy currents are a great concern.

Either way, by reducing or stopping the eddy current production, the driving system would have to be reworked since it relies on induction. One possible way to solve this problem would be to cover the rotor with a conducting film with the necessary thickness for the generation of inducted currents. Another radically different approach would be to use a driving system based on different principles. An example would be to use radiation pressure focused tangentially to transmit torque to the rotor, accelerating it. The basic principles of such a system are explored in appendix A.

5.3.2 Thermal Expansion Coefficient

Thermal fluctuation also increases the uncertainty of the SRG. Thermal expansion alters the dimensions of the rotor changing the moment of inertia and the surface of interaction. The smaller the dimensions, the smaller will be the impact of these thermal fluctuations.

Nevertheless, a rotor material with a small coefficient of thermal expansion would also help to mitigate this problem.

5.3.3 Density

Density has a pretty straightforward effect as it can be seen in equations 3.11 and 5.8. The lower the density, the lower the moment of inertia and the higher will be the deceleration response with the pressure.

But at the very least, the material has to be magnetic which is a constraint when it comes to its selection. In this context, an heterogeneous rotor built of different materials may be an interesting approach.

As an example, a cylinder composed of two materials could be conceived like shown in figure 5.3. One inner magnetic core and one outer low-density material. The magnetic core would allow the magnetic suspension and driving system to work as expected while the outer low-density hollow cylinder would increase the interaction surface without increasing the moment of inertia as much.

With the following moment of inertia

$$I = I_{core} + I_{outercylinder} = \frac{1}{2}\pi\rho_1 h r_1^4 + \frac{1}{2}\pi\rho_2 h\left(r_2^4 - r_1^4\right) \tag{5.21}$$

To calculate this rotor's deceleration rate, its moment of inertia is considered for equation 5.6. Note that r is now r_2 for the new rotor.

$$-\frac{\dot{\omega}}{\omega} = \frac{2pr_2^3}{I\bar{c}}\left(r_2 + 2h\right) \tag{5.22}$$

$$-\frac{\dot{\omega}}{\omega} = \frac{4pr_2^3}{\pi h\bar{c}\left(\rho_1 r_1^4 + \rho_2\left(r_2^4 - r_1^4\right)\right)}\left(r_2 + 2h\right) \tag{5.23}$$

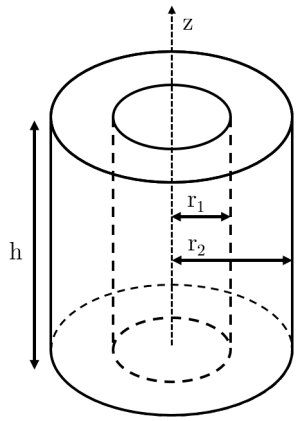

Figure 5.3: Diagram of a cylindrical rotor composed of two concentric cylinders of different materials.

Where $\rho_2 < \rho_1$, being ρ_2 the density of the outer hollow cylinder and ρ_1 the density of the inner cylinder. The radius r_1 of this inner cylinder would be only as big as to provide the magnetic suspension and driving forces.

5.3.4 Geometry

Another similar approach to consider would be the use of other less conventional solid geometries, examples of which are presented in figure 5.4.

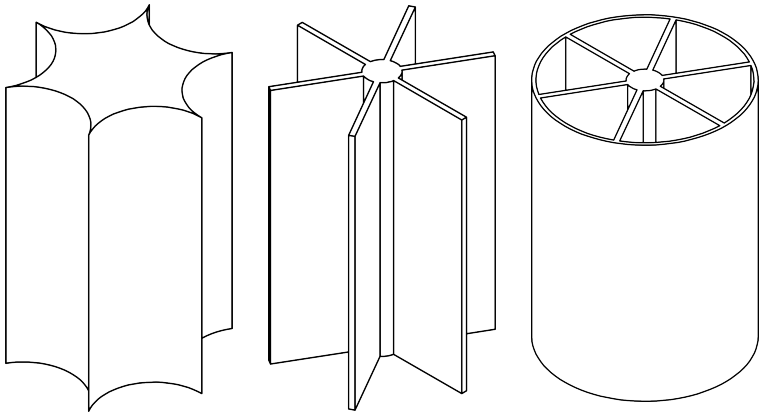

Figure 5.4: Examples of alternative rotor geometries that would improve the trade-off between the surface of interaction with the gas and the moment of inertia.

However, it is uncertain how stable the suspension and driving of such rotors would be. Throughout the literature, ball bearings are usually used as rotors because of their very low building tolerances and high stress handling capabilities. Having asymmetries in the rotor may render the use of alternative geometries impracticable, but this is something requiring further studies.

CHAPTER 6

PROPOSED CYLINDRICAL SPINNING ROTOR GAUGE

On revisiting the spinning rotor gauge, the system described in chapter 3 was used as a starting point. With the main starting difference being the use of a cylindrical rotor instead of a spherical one, as it would be a more versatile setup to further study radiation pressure or other possible improvements. This represents an additional challenge when compared to spherical rotors since there is angular vibration and precession to take into consideration.

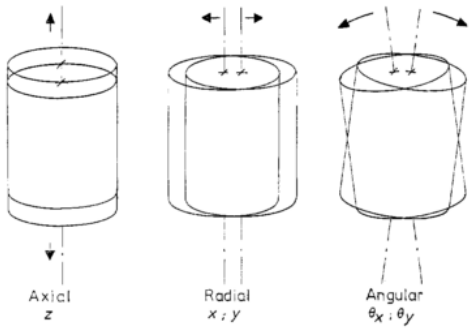

Figure 6.1: Rotor's available vibration movements where z is the symmetry axis [18].

6.1 The Rotor

There were several factors to take into account when choosing the rotor's dimensions. First, radiation pressure future studies require a cylinder with sufficient radius as to provide enough area for the incidence of radiation. On the other hand, there are disadvantages for large radius cylinders, like angular stabilization issues. As Fremerey describes it [18], a rotor with isotropic permeability allows the magnetic flux to take the path of least reluctance. If the cylinder is somehow tilted by angular vibrations, the field lines would

concentrate at the edge of the cylinder's surface closer from the coil, augmenting the displacement. To mitigate this effect, Fremerey advised a height/radius ratio of 10:1. Another way to avoid this possible problem is to exchange the cylinder for a rod shape with spherical round ends. A high height/radius ratio helps but it has a secondary effect. The moment of inertia of a rotating object tends to increase. With a high height/radius ratio the rotor's moment of inertia will have much to gain by going from the vertically aligned position to an horizontal one. In this sense, a disk with a height/radius ratio inferior to one would be more stable than a long cylinder, which requires lateral stabilization to keep a stable spin along its vertical axis.

Nevertheless, in this context there has not been much research done regarding the magnetic suspension of rods, and given that in practice no problems were found for cylinders with higher ratio radius/height, a cylinder with a radius of 2.5 mm and height of 25.6 mm was chosen, which is close to the actual SRG's rotor radius with 2.25 mm.

6.2 Vertical Magnetic Suspension

The first system to tackle was the vertical magnetic suspension. At first, a system was devised with the use of two Hall sensors. They were placed symmetrically over and under the coil's magnetic core, like shown in figure 6.2a. Given their symmetric location in respect to the coil, a difference in the signals would originate from the rotor's own magnetic field. By taking the difference of the two signals, it was possible to infer the rotor's position. From there, and based on this input, a control circuit generated the output signal required for stable suspension, by adjusting the current in the coil accordingly, just like any active feedback control system.

The Hall sensors worked very well for a simple magnetic suspension system, but as other systems were required, like lateral stabilization and rotation, it became increasingly harder to distinguish the rotor's position signal from other magnetic fields. Moreover the sensor signal was far from linear with the rotor's height, making the feedback signal very complex. When it became evident that this solution was not practical for a SRG, the displacement sensing was then changed from the Hall sensor system to an optical system, as shown in figure 6.2b.

It comprises an infrared light-emitting diode (LED) pointed to an infrared phototransistor across the symmetry axis and tangentially to the position of the rotor's top end. Any down displacement from the height set point position would expose more light from the LED to the phototransistor and increase its output signal. On the other hand, if the displacement was to be upwards, the rotor would block too much infrared light, and the output signal would decrease.

The associated electronics have also been through several iterations. In its final version, the magnetic suspension control circuit represented in figure 6.3 works surprisingly well for its relative simplicity.

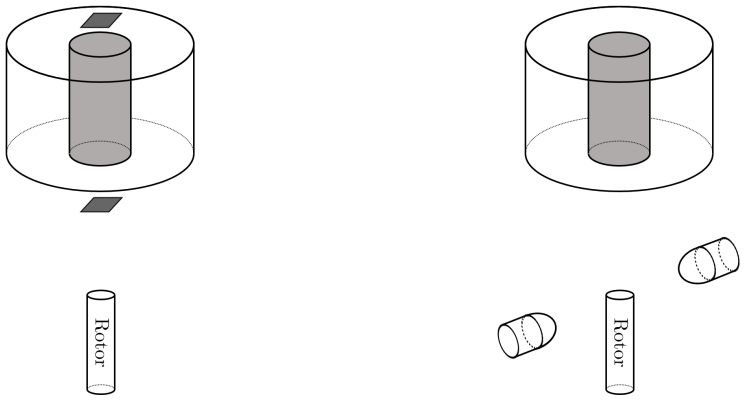

(a) Magnetic suspension with two Hall sensors

(b) Magnetic suspension with a LED-phototransistor pair

Figure 6.2: Diagram of magnetic suspension setups. On the left, the first type of magnetic suspension implemented, and on the right, the system chosen for the final prototype.

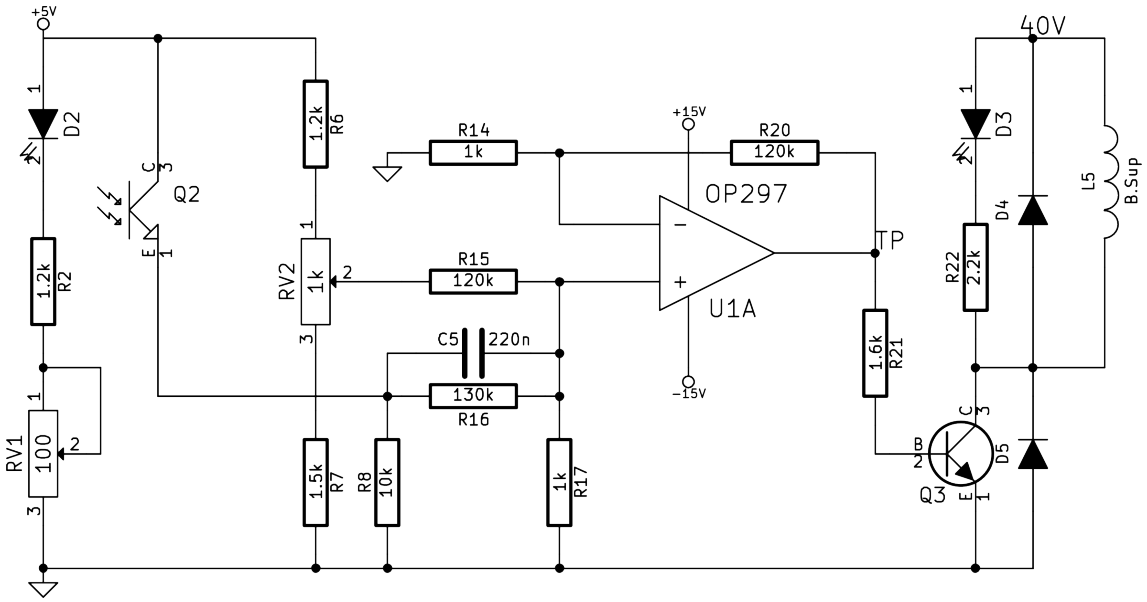

Figure 6.3: Magnetic suspension control circuit.

The LED D2 and the phototransistor Q2 comprise the aforementioned position sensor. Both these components are located inside two black shallow support cylinders with 2 mm holes facing each other, as represented in figure 6.4. These not only block most of the possible external infrared interference, but also defines the position window where the system tracks the body.

To make sure the position signal is using the most of the dynamic range allowed by the 15 volt rail supply, the resistance in series with the LED is chosen so that the signal in

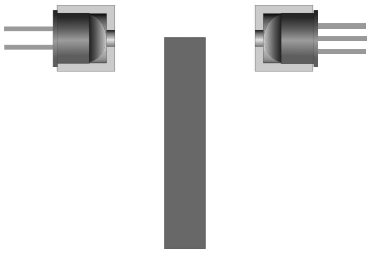

Figure 6.4: At scale cutaway view of the support parts for the LED, on the left, and for the phototransistor, on the right.

the phototransistor's emitter pin is just under the saturation voltage when the body does not block any light. If the resistance is too low, i.e. if the light emitted by the LED is too intense, the gain may be increased to the point where any displacement of the body will suffice to saturate the signal. Under these circumstances the rotor is not tracked through the 2 mm range, but for only a fraction of it, which reduces the quality of the magnetic suspension.

The capacitor C5 and the resistors R16 and R17 form a phase-lead network, responsible for the control aspect of the circuit, making them critical to the vertical stabilization of the rotor.

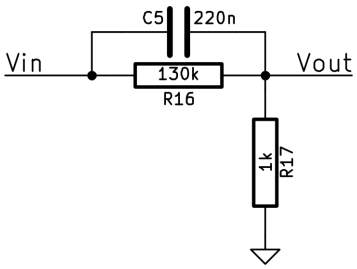

Figure 6.5: Detail of the phase lead network used in the magnetic suspension circuit, in the figure 6.3.

For low frequencies, the network will act as a simple voltage divider, whereas very high frequencies will tend to unity gain. The Bode plot of the circuit's transfer function presented in figure 6.6 conveys not only the gain along the frequency domain, but also the phase shift caused by the capacitor.

This phase shift is caused by the current derivative properties of capacitors. A simple analysis of the circuit wields the following result.

$$\frac{V_{out}}{R_{17}} = C\frac{\partial\left(V_{in} - V_{out}\right)}{\partial t} + \frac{V_{in} - V_{out}}{R_{16}} \tag{6.1}$$

The derivative aspect of the circuit is very important, as it provides PD controller type characteristics, but unlike a PD controller that performs its derivative operation

throughout the whole signal frequency range, a phase lead compensator only provides a phase shift in a selectable frequency window.

In simplistic terms, this property allows the controller to assess its output based not only on positional information but also on velocity information.

The respective transfer function can be attained from equation 6.1, by applying the Laplace transform.

$$G(s) = \frac{R_17(1 + R_16Cs)}{R_16 + R_17 + R_16R_17Cs} \tag{6.2}$$

$$G(s) = \frac{s + a}{s + b} \tag{6.3}$$

Where $a = 1/R_1C$ and $b = 1/R_1C + 1/R_2C$. -a and $-b$ are a zero and a pole, respectively. And the condition for a phase lead compensation is that $a < b$ which is the case. By adjusting this two variables, one can tune the frequency window that suffers the derivative phase shift.

One of the big disadvantages of PD controllers is that they tend to amplify high frequency noise, for which the phase lead compensator presents a clear advantage, since the user can select both corner frequencies of the phase shift. Again, the Bode plot in figure 6.6 is a great way to visualize this aspect of the transfer function.

The proportional aspect of the controller is not of much concern here since it can be easily adjusted in other parts of the stabilization circuit.

Additionally to the main upper coil, a bottom coil was also introduced as a way to experiment with symmetric and asymmetric configurations as discussed by Fremerey [18]. Both of these coils are aided by a steel magnetic core.

The nominal current needed for suspension was enough for significant heat dissipation in the upper coil. As a consequence, when operating over extended periods of time, the coil would get hotter and its resistance would increase, to which the circuit would respond by increasing its output voltage. However, there were times when the output level would reach the supply rails causing the rotor to fall. To avoid this problem, and to reduce the high current, neodymium magnets were placed on top of the upper coil's steel core, thus increasing its magnetic field and reducing the need for current. A fan was also used to cool down the whole instrument.

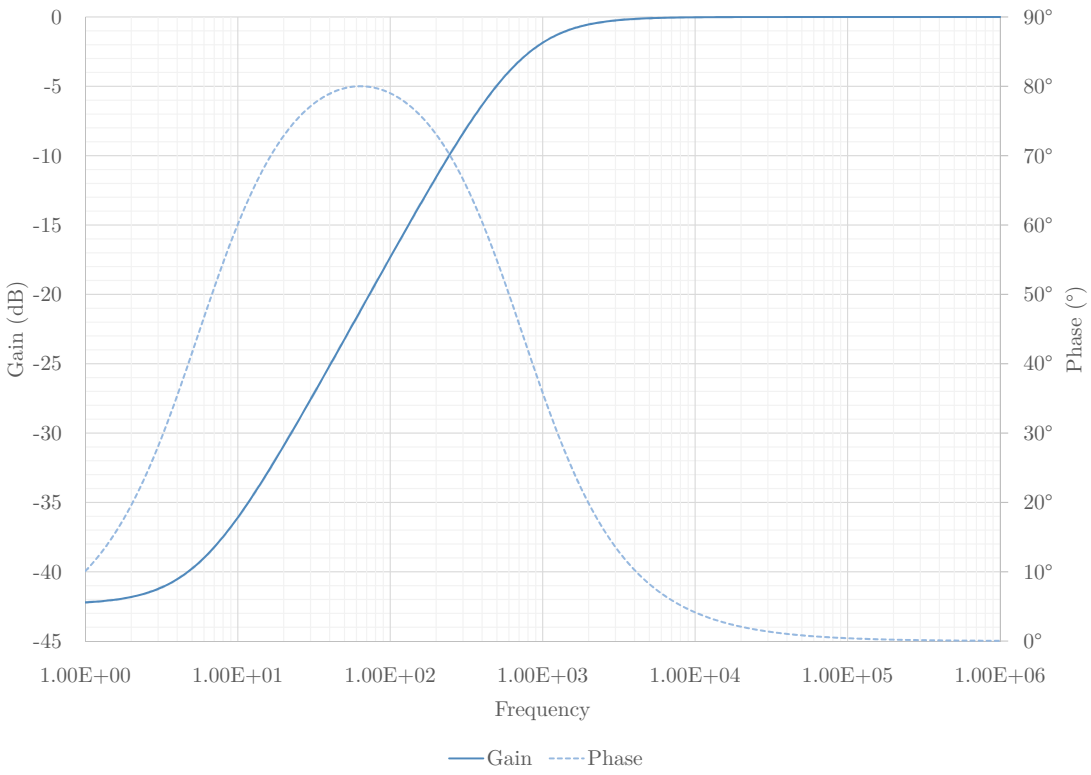

Figure 6.6: Bode Plot of the phase lead network.

6.3 Lateral Damping

To a certain extent, there is passive stabilization at work. It results from the shape of the magnetic field whose gradient causes the suspended body to minimize its energy by positioning itself at the vertical symmetry axis. In the situation depicted by figure 6.7a, the gradient is much more noticeable when closer to the coil where the magnetic field is stronger. As a result the system behaves similarly to a pendulum, where the upper end of the rotor is kept in place vertically by the levitation feedback circuit and horizontally by the afore mentioned field shape, and the lower end is essentially left free to oscillate since it is farther from the coil where the magnetic field is weaker.

With the objective of extending this passive stabilization effect to the lower end of the rotor, a magnetic circuit was added, as shown in figure 6.7b, amplifying and further shaping the levitation coil's magnetic field.

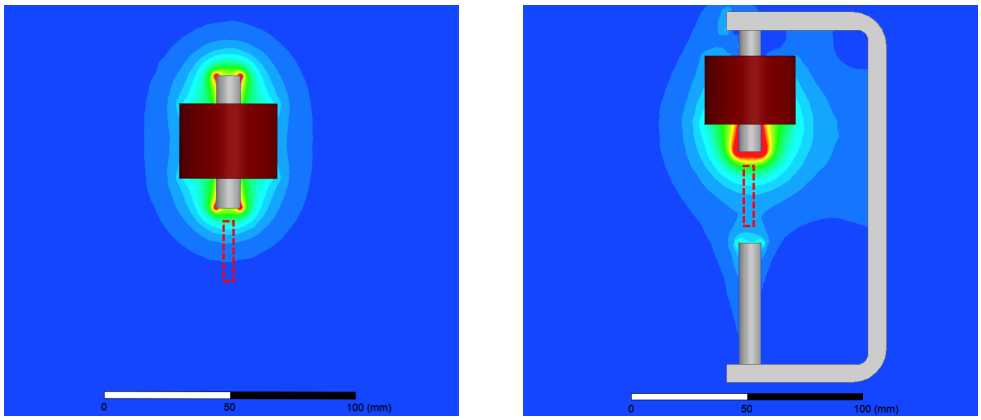

(a) Typical magnetic suspension configuration

(b) Magnetic suspension with magnetic circuit for a more confined field

Figure 6.7: Finite element method (FEM) analysis comparison between simple magnetic suspension and magnetic suspension with a magnetic circuit where different colors represent different magnetic field magnitudes and the dashed red box represents the rotor's position.

Since passive stabilization alone was not enough, an active horizontal stabilization system was designed to prevent these oscillations .

Originally, and based on Fremerey's spinning rotor gauge [42], a set of four vertical coils placed parallel to the rotor were used for the horizontal stabilization. The idea being that if the rotor displaces itself from the symmetry axis in the direction of a stabilization coil, that coil would produce a repelling magnetic field while another coil in the same plane from which the rotor is getting farther away would produce an attractive magnetic field.

Given the tendency for pendulum like behaviour, emphasis was given to the correction of the lower end displacement. As such, a set of four Hall sensors were placed beneath the rotor for position displacement sensing, as can be seen in figure 6.8a, but this solution was soon regarded as insufficient. The problem laid in the fact that the damping would

only work effectively on the lower end of the rotor that was being tracked by the position sensing circuit and the system would induce vibrations on the upper end that the passive stabilization was not able do suppress.

With this configuration, it was possible to determine that Fremerey's original design was not suitable for the levitation of a cylinder, because a cylinder, unlike a sphere, does not have a general horizontal displacement. Instead, the angular freedom allows anti parallel displacement of the rotor's ends.

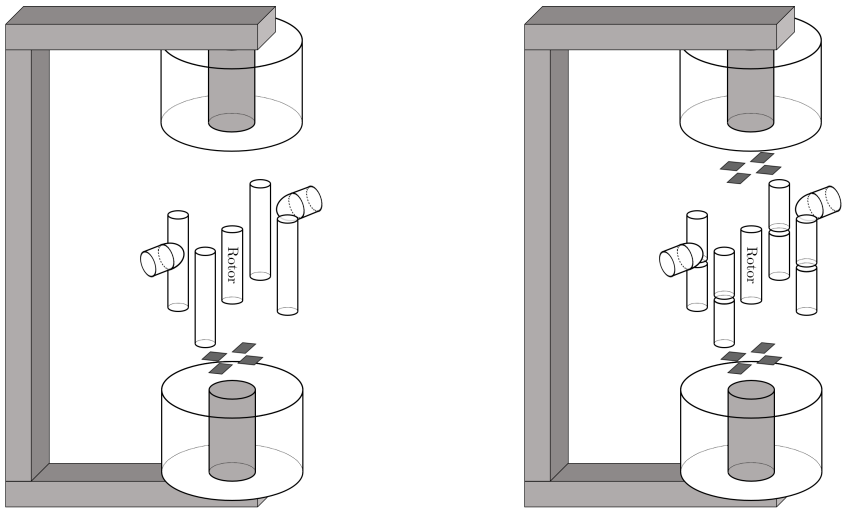

(a) First attempt with only four damping coils

(b) Final prototype solution with eight damping coils

Figure 6.8: Diagram of magnetic suspension setups with lateral damping.

For this reason, and after several iterations, a set of eight vertical coils were implemented in order to produce the horizontal damping. A set of four coils for the upper end of the rotor and another set of four coils for the lower end of the rotor. The position tracking of both ends was done with a set of four Hall sensors each, as shown in figure 6.8b.

The way this system works is by dividing Hall sensors in pairs. Each end of the cylinder is tracked by two pairs, in other words there are two pairs in the upper part of the system, and two pairs for the lower part. Each pair is positioned along a vertical plane, with the rotor in between. Together, these sensors and their respective damping coils, form an independent lateral damping subsystem responsible for damping the vibrations of one end of the rotor in regard to the said vertical plane. This means that the lateral damping system is actually formed by four lateral damping subsystems, each formed by two sensors and two damping coils that act independently of the other subsystems.

In each subsystem, if the rotor stays stable halfway along the sensors, no correction force is necessary, and the damping circuit's output stays zero. On the other hand, if the rotor vibrates, its ends will move closer to the sensors in one side and farther away from

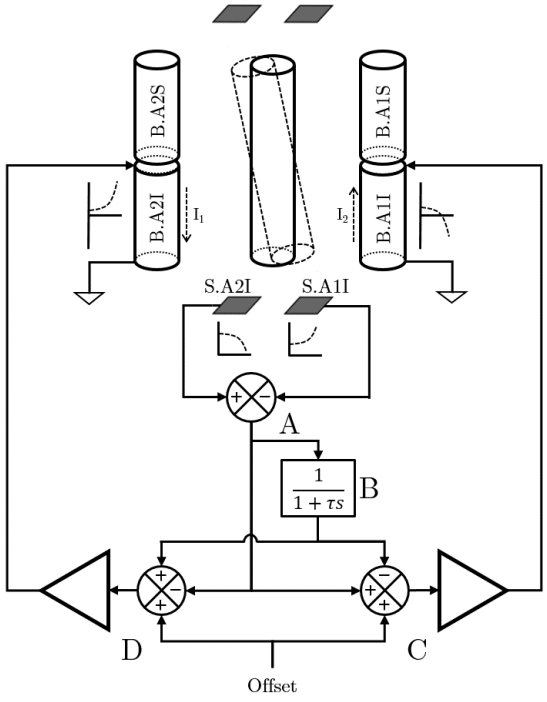

Figure 6.9: Block diagram of one Hall sensor pair and respective damping coil pair subsystem.

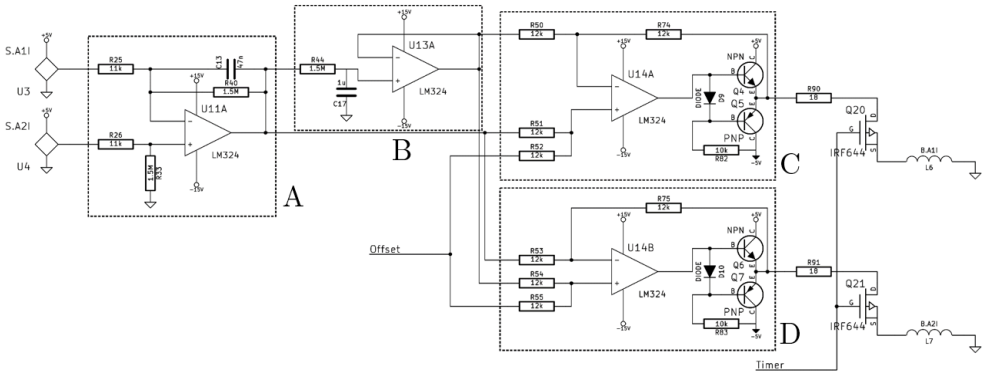

Figure 6.10: The electric circuit corresponding to one of the lateral damping subsystems.

the others in the other, generating a differential signal between Hall sensors.

At first, the circuit takes the difference between the pair of sensors in stage A. Then, the signal goes through a low pass filter, B, with a large time constant whose output is practically a DC signal.

If the sensors had perfectly equal characteristics, and were perfectly symmetrically positioned, then this DC signal would be zero and this step would be unnecessary, but since this is impossible, this signal is subtracted from the original signal in order to obtain a zero centred displacement signal. A capacitive coupling could also be used to filter any DC signal. However the frequency range of the lateral damping system starts at very low

frequencies, at 1 or 2 Hz, which is very low for AC coupling, since it works as a high pass filter and would require a very large capacitance to to allow frequencies as low as 1 Hz to pass. Even then, some distortion would always be present for the lower end of the frequency range. The use of a low pass filter also helps to cope with any small tilt in the vertical alignment that the instrument may have, since this would mean that the lower end of the rotor would naturally be closer to one of the sensors. This would cause a change in the DC signal of the low pass filter instead of being interpreted as a displacement by the lateral damping system.

Then, the circuit proceeds to amplify two symmetric versions of the signal, one with positive gain, C, and other with negative gain, D, to feed to the respective damping coils. In this last step, there is also an optional DC offset summed into both these signals. It is important to note that contrary to the displacement signal, the offset is the same for both damping coils, and not symmetrical. Its purpose is not to create any differential signal between them, but to aid the passive stabilization component by changing the magnetic field shape.

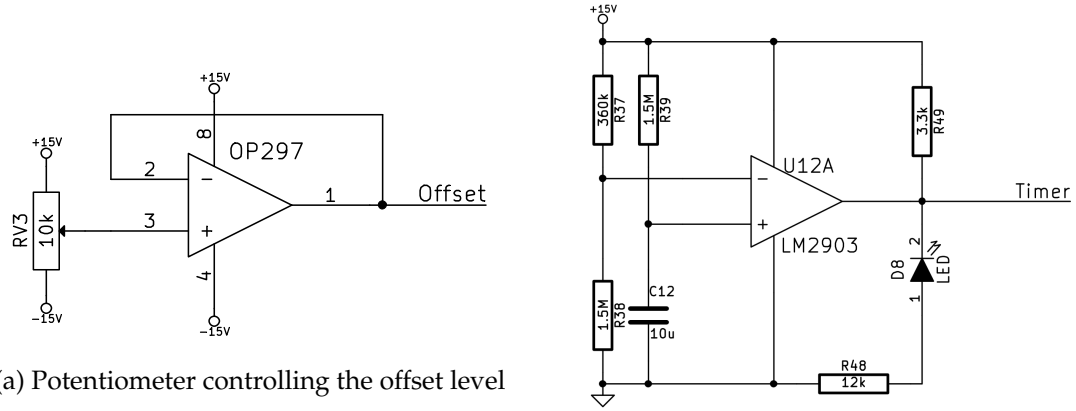

(a) Potentiometer controlling the offset level

(b) Delay circuit

Figure 6.11: Offset and delay auxiliary circuits to the main circuit in figure 6.10.

The offset has to be equal in all the four subsystems in order to avoid any displacement in the rotor from the symmetry axis.

The FEM simulation helps visualizing the way the magnetic field shape can be influenced. However, from the equipotential lines alone, it is hard to predict its practical consequences. For this reason, other several simulations were performed to show the torque generated in a tilted rotor under these different conditions.

In the simulation environment, the rotor was tilted 10 degrees in each direction from the symmetry axis with a step of 5 degrees and the torque was measured for each angle. The resulting plot can be seen in figure 6.13, where the steeper the torque response curve is with the angle, the stronger is the passive stabilization. As such, a magnetic field opposing the levitation field turns out to help the passive stabilization, where the supporting field configuration makes it weaker. At first only three measurements were performed, but

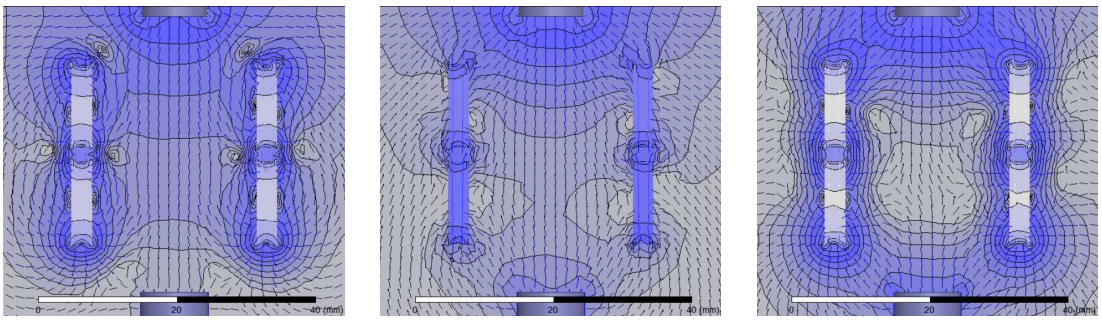

(a) Opposing magnetic field (b) Zero current (c) Supporting magnetic field

Figure 6.12: FEM simulation of the lateral damping system offset's impact in the overall magnetic field shape, where the black lines represent magnetic equipotential lines. The generated magnetic field is denominated as supporting if it contributes to the levitation of the rotor and opposing if it makes the levitation more difficult.

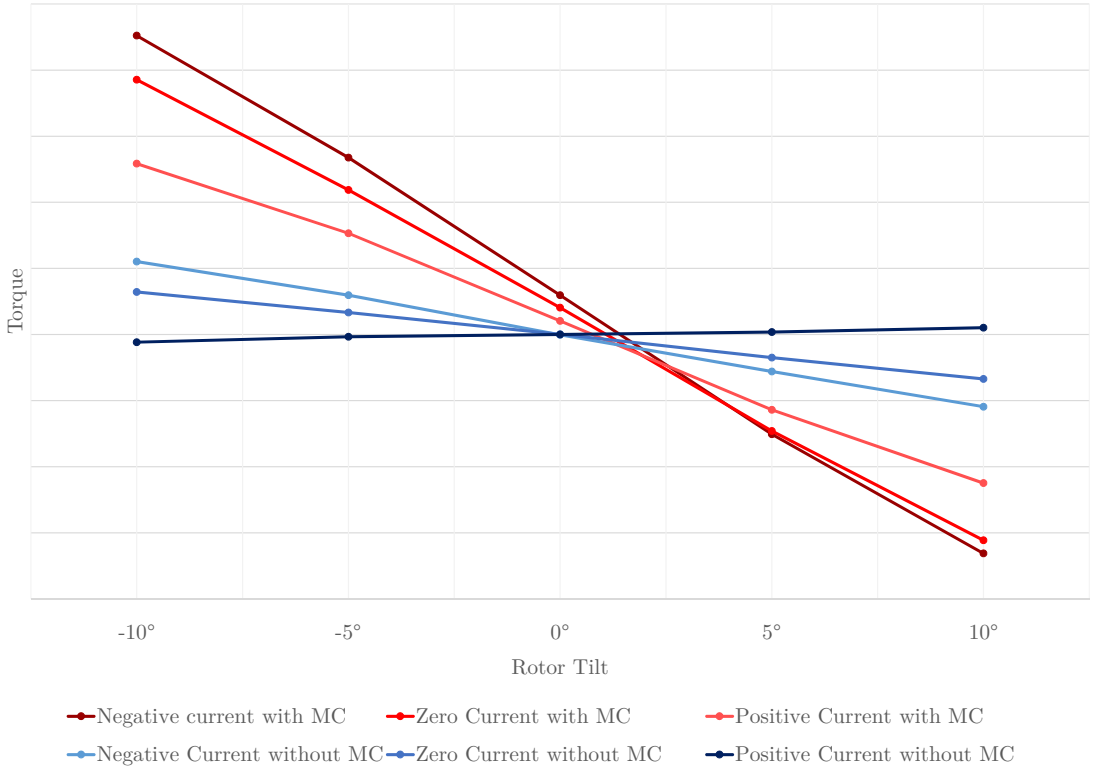

Figure 6.13: Torque in arbitrary units from the passive stabilization for several rotor angles with and without the magnetic circuit (MC).

the fact that the torque did not cross the zero at zero current was surprising. This fact motivated three new measurements without the magnetic circuit. The absence of it reduces considerably the strength of the passive stabilization, and eliminates the shift in the zero crossing.

From this plot, it is possible to conclude that most of the passive stabilization is carried by the suspension field, but can be improved by the lateral stabilization by generating an

opposing magnetic field. The magnetic circuit aids significantly the suspension magnetic field, but being a disturbance in the instrument's cylindrical symmetry, it is expected to introduce some degree of asymmetry in the magnetic field.

The maximum current of the lateral stabilization coils is rated at 280 mA. This represents a limitation in the dynamic range of this system that is reduced even further by the introduction of a DC offset. Given that the lateral damping system worked as intended, and no observable improvement came from the introduction of a DC signal, the offset was left at zero volts.

Additionally, there is a delay circuit controlling the gate of the MOSFETs in the output of the lateral stabilization circuits depicted in figure 6.24b. It works by comparing the voltage of a voltage divider with the voltage of a charging capacitor. The RC time constant of the capacitor with it's series resistor determines the charging time. As soon as the capacitor charges beyond a certain threshold determined by the voltage divider, the comparators changes its state from low to high, raising the gate voltage of the MOSFETs.

This circuit is used to shut off the lateral stabilization in the first seconds of operation, where the magnetic suspension is still being stabilized along the vertical axis, and the rotor is very unstable. By shutting off, the vertical magnetic suspension system is allowed to stabilize without interference of the lateral damping system and its coils are spared from unnecessary current spikes from the rotor's initial erratic vibrations.

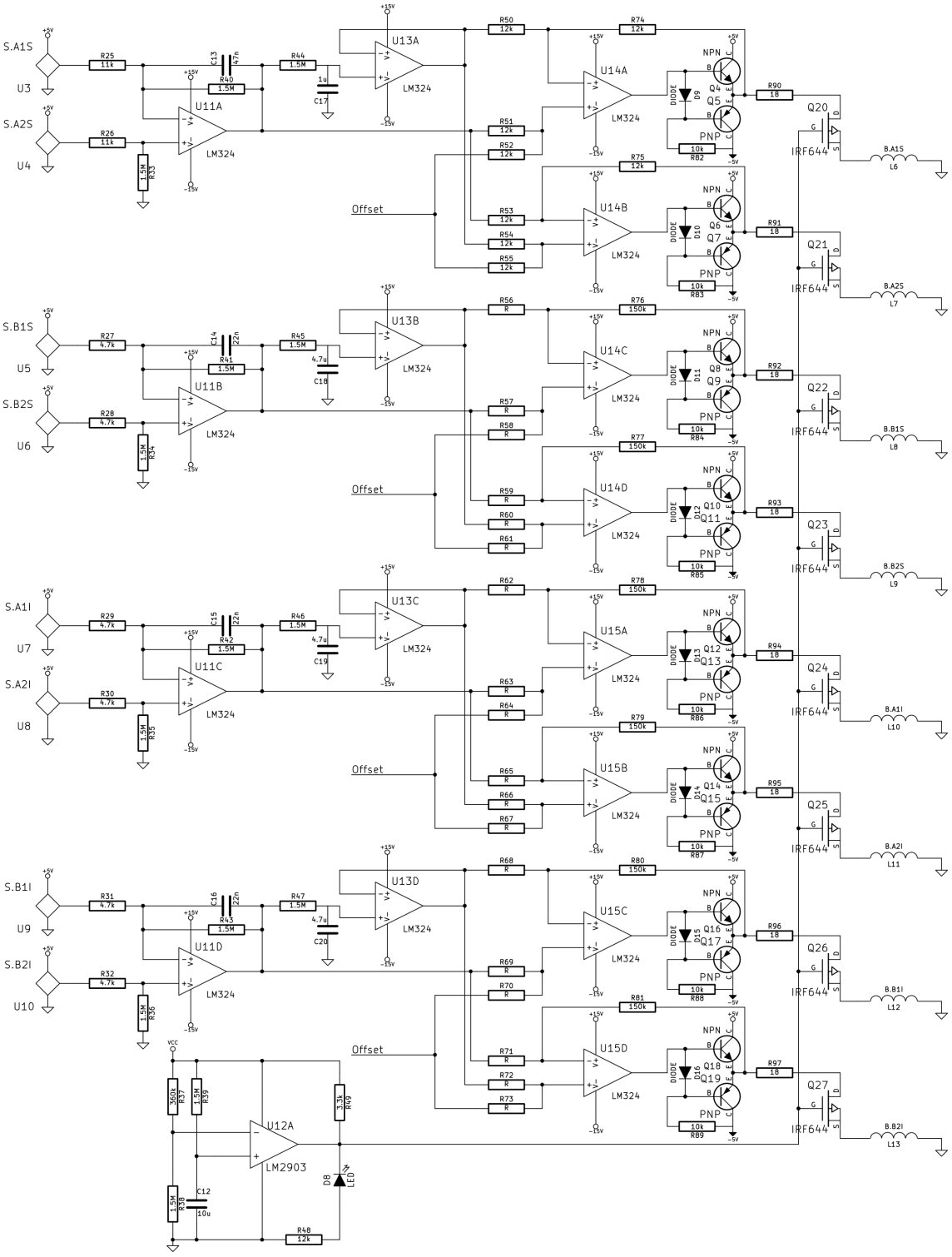

Figure 6.14: Complete lateral damping system circuit, with the four subsystems.

6.4 Driving system

The driving system is in everything similar to an induction motor. In these machines, windings in the stator are exited by alternating currents. These alternating currents create a rotating magnetic field that in turn induces currents in the rotor windings. These are electrically short-circuited, and the only current they experience is a consequence of the stator's field induction. Thus, the name induction motor.

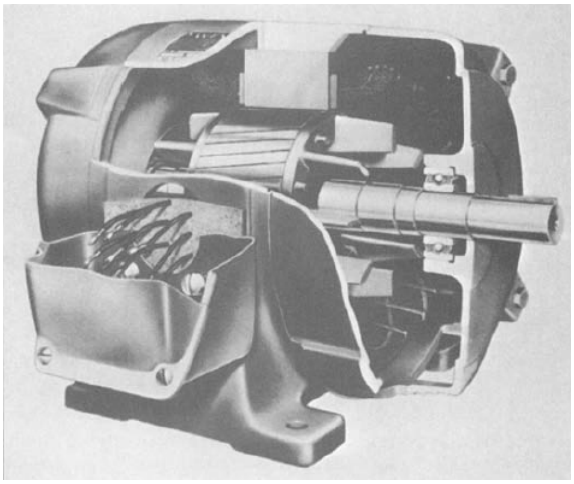

Figure 6.15: Typical induction-motor speed-torque characteristic [56].

Often, the rotor windings are nothing more than a conductor grid, also called squirrel cage, which is the case of the induction motor in figure 6.15. The eddy currents generated here by the stator's magnetic field create the rotor's own magnetic field. From the interaction between this two fields, a torque is generated.

However, contrary to synchronous motors, the rotor can never achieve the magnetic field frequency. At the same frequency, the gyrating field would be static in the rotor's reference frame, and therefore no induction would occur and consequently no torque.

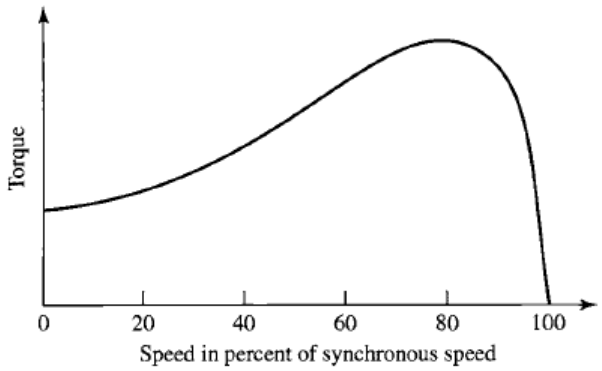

Figure 6.16: Typical induction-motor speed-torque characteristic [56].

There are three different rotating components to be considered: the rotor itself, the stator's magnetic field and the rotor's induced magnetic field. The magnetic fields are

synchronous, with only a difference in phase between them, while the rotor speed lags behind and this difference in speed is called the slip.

$$s = \frac{n_1 - n}{n_1} \tag{6.4}$$

Where n is the rotation speed of the rotor, and the n_1 is the speed of both magnetic fields.

The slip is critical to the intensity of the induced magnetic field, but the phase difference between magnetic fields is just as important.

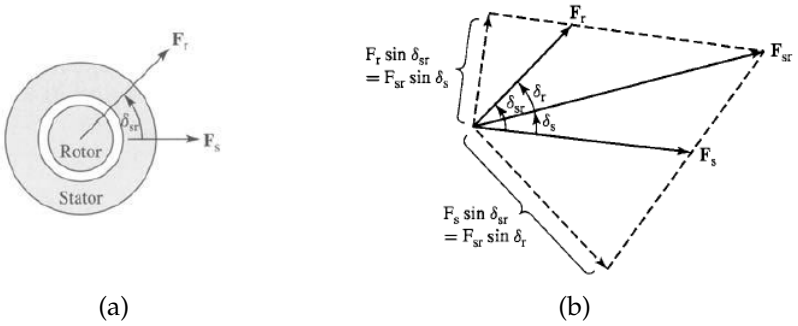

(a) (b)

Figure 6.17: Simplified two-pole machine: a) elementary model and b) vector diagram of the induced waves [56].

Torque is produced by the tendency of the rotor and stator magnetic fields to align. Note that, in figure 6.17b, the phase difference δ_{sr} is positive, i.e., the rotor induced wave $\mathbf{F}_r$, leads that of stator $\mathbf{F}_s$.

Being a standard induction motor, an IC driver for bipolar stepper motors was used.

The circuit used, depicted in figure 6.18, is strongly based on the typical application circuit suggested by the IC's datasheet.

The IC supports a number of transistor to transistor logic (TTL) control inputs, from the direction of rotation that can be clockwise or counter-clockwise, to the output signal shape. However, these were not used, and were all connected to 5 volts.

For the clock, a square wave generator was used with a frequency of roughly 70 kHz. However, it was measured to be eight times higher than the actual rotation frequency, consequence of the fact that it takes several clock pulses for the IC to be able to form one output period.

Therefore, the actual frequency of the magnetic field is $\sim$ 8 kHz. For comparison, the MKS's SRG-2 manual [57] indicates a frequency of 153 kHz, which was the target. But as the frequency increases, so does the perceived resistance of the driving coils, due to inductance, to the point where the integrated circuit cannot keep up, and the current starts to fall. Nevertheless, the frequency used provided the necessary torque for this prototype.

Pushing the IC to the limit took a toll in its thermal dissipation. The IC itself has an over temperature protection that shuts down operation if it is too hot, but the driving off

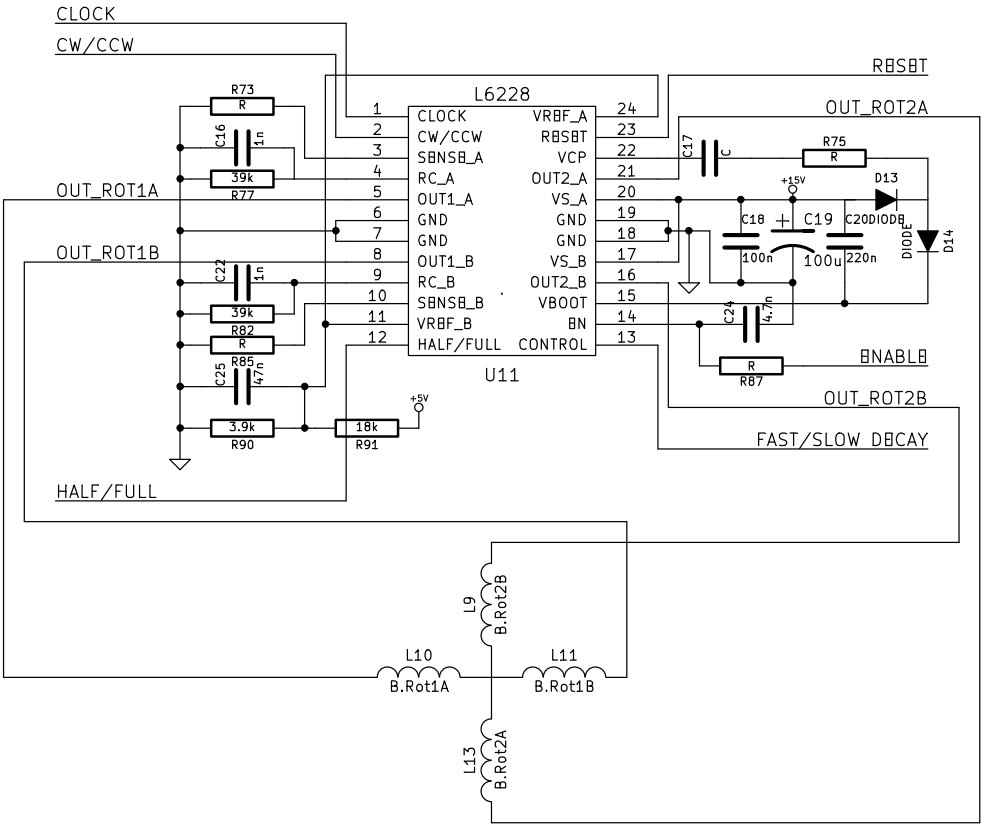

Figure 6.18: Rotation driving circuit.

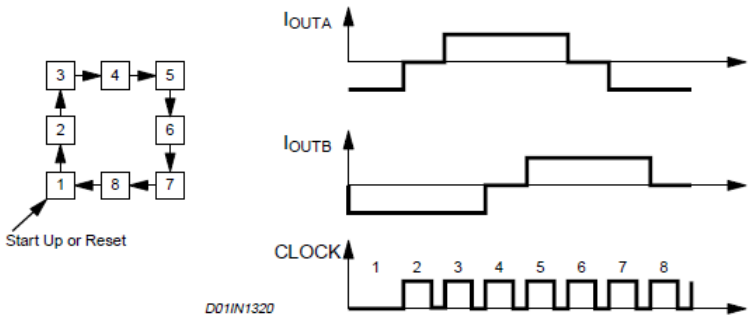

Figure 6.19: Generic layout of the system.

the rotor would be visibly affected. Since the IC came as a through-hole DIP package, it was not practical to use a heat sink, and thus a fan was used to cool off the circuit.

The rotation circuit concludes the operational aspects of the spinning rotor gauge. All things considered, the following diagram shortly conveys the way the different systems are organised.

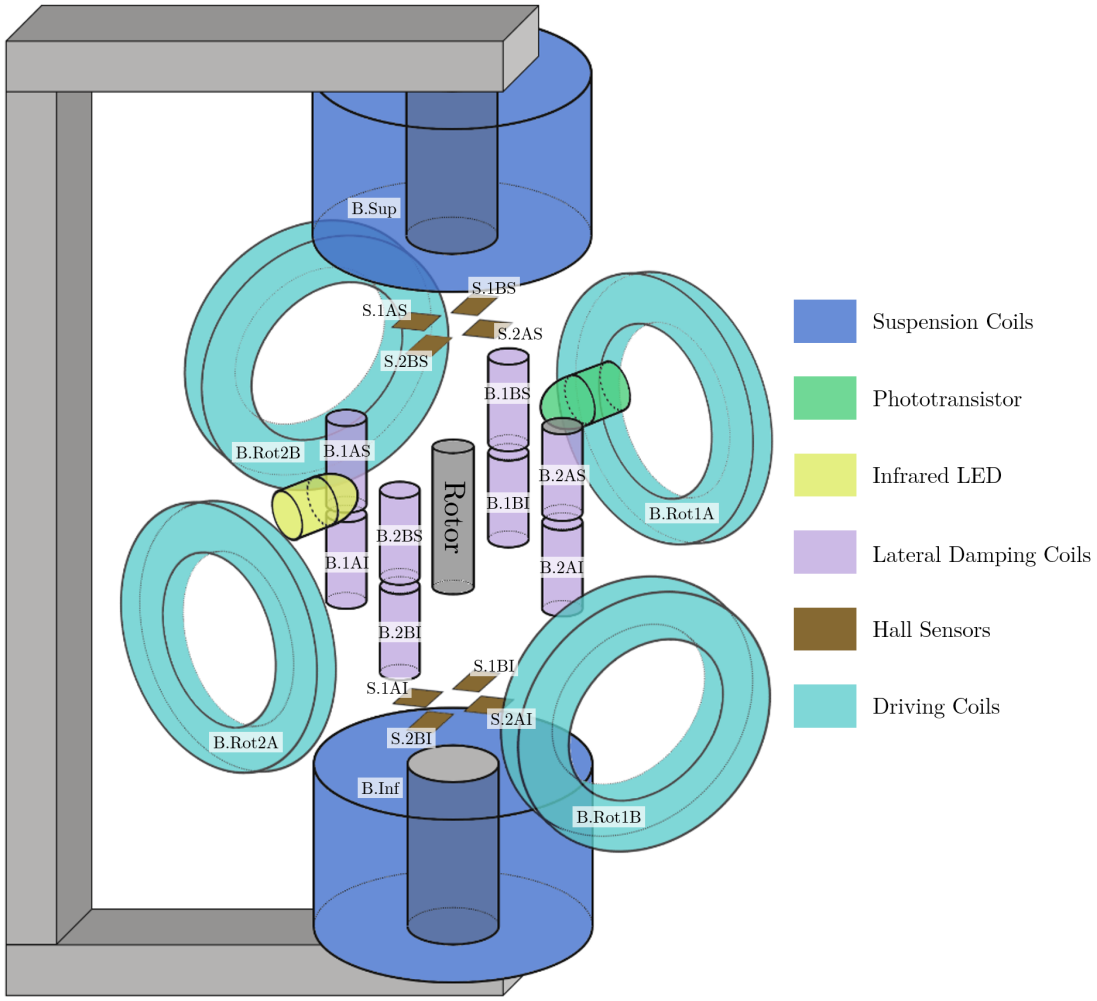

Figure 6.20: Diagram of the prototype's different systems. Every component is identified by a code used in the different circuit schematics in figures 6.3, 6.9, 6.10, 6.14 and 6.18.

6.5 Measurement

Every pressure reading is calculated from one or more measurements of the rotor's frequency of rotation. This is accomplished by another infrared-phototransistor pair, but unlike the pair responsible for the vertical stabilization, this pair is facing the rotor's lateral surface. The light emitted by the LED is reflected in the surface of the rotor into the phototransistor. The surface is irregular, especially after its oxidization in the glass welding process that will be explained in detail in the next section, which means that the reflection on its surface will also be irregular, causing a periodic signal to appear at the emitter of the phototransistor with the rotor's rotation frequency.

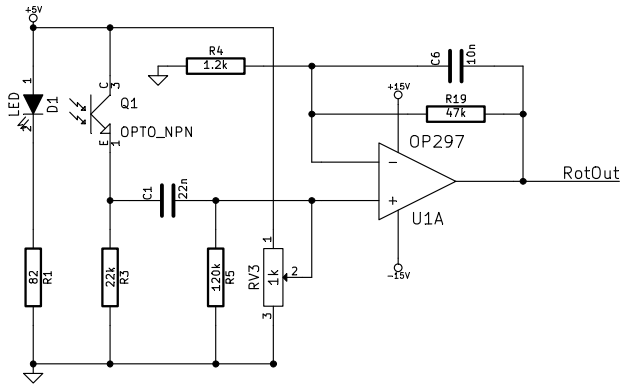

Figure 6.21: Rotation frequency measurement circuit.

This signal goes through a comparator with a defined threshold level that outputs a transistor to transistor logic (TTL) square signal as exemplified by figure 6.22.

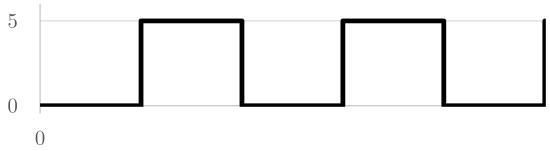

Figure 6.22: Example of the shape of a TTL signal with the rotor's frequency of rotation ready for data acquisition.

This signal is then feed into an $Arduino^{TM}$ based microcontroller input. The microcontroller code makes use of a programming library specifically built to measure frequencies called FreqMeasure. This library works by measuring the period between successive levels in the measured signal which works very well for frequencies lower than 1 kHz. Above this level if the microprocessor's interrupts are disabled for more than one cycle of the waveform, the measurement can span two or more cycles, resulting in a wrong measurement. If the rotor was able to reach higher frequencies than 1 kHz, this system would have to be reworked.

In the programming of the microcontroller the user is able to define a number of periods to average, before sending the data to a pc through serial port. At this point the

user is able to define the acquisition scheme as was discussed in the subsection 3.2.1. For the validation of the prototype, the most simple scheme represented in figure 3.8 was used.

On the computer, a python script then manages the data acquisition in parallel with the reference gauge controller unit. Besides receiving, managing and storing the data, the script was also able to plot the data live for user feedback.

Figure 6.23 summarizes the process in a block diagram.

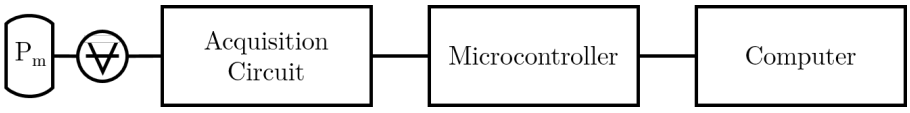

Figure 6.23: The different stages of the measurement process of the instrument.

6.6 Pressure Calculation

Assuming that every variable is constant in the present system except for the pressure and the relative deceleration rate, one can calculate the conversion factor.

$$p = -\frac{\dot{\omega}}{\omega} \cdot C \tag{6.5}$$

$$C = \frac{\pi r \rho \bar{c}}{4\sigma} \left(\frac{1}{2 + r/h} \right) \tag{6.6}$$

Where $\bar{c}$ is the mean thermal speed and equal to

$$\bar{c} = \sqrt{\frac{8RT}{\pi M_m}} \tag{6.7}$$

The parameters of the prototype are presented in table 6.1.

Table 6.1: Values of the parameters of the prototype relevant for the pressure calculation.

Parameter	Values	Units
R	8.314	$J/mol.K$
T	293	K
M_m	0.029	kg/mol
h	25.6	mm
r	2.5	mm
ρ	7730	kg/m^3
σ	1	

Note that despite the factor σ being listed as valuing one, this is not a known parameter. The value one is the theoretically expected, and the real value can drift upwards or

downwards but usually not very significantly. Therefore, the value one was used as a starting point.

Considering all the values in the table 6.1, the factor C is evaluated.

$$C = 3.35 \times 10^3 \qquad (Pa.s)$$

In a simpler way, the relationship between pressure and the relative deceleration rate can be expressed as following, for the specifications of the prototype.

$$p = 3.35 \times 10^3 \frac{\dot{\omega}}{\omega} \qquad (Pa) \tag{6.8}$$

6.7 Mechanical Considerations

The first iterations of the system were simple enough that the different parts could be built in the department's workshop, from the magnetic core to the coil supports. These parts became more complex through the different iterations to the point where it became impractical to machine them. At this point 3D printing was used since it was more versatile and was a simple enough solution for rapid prototyping.

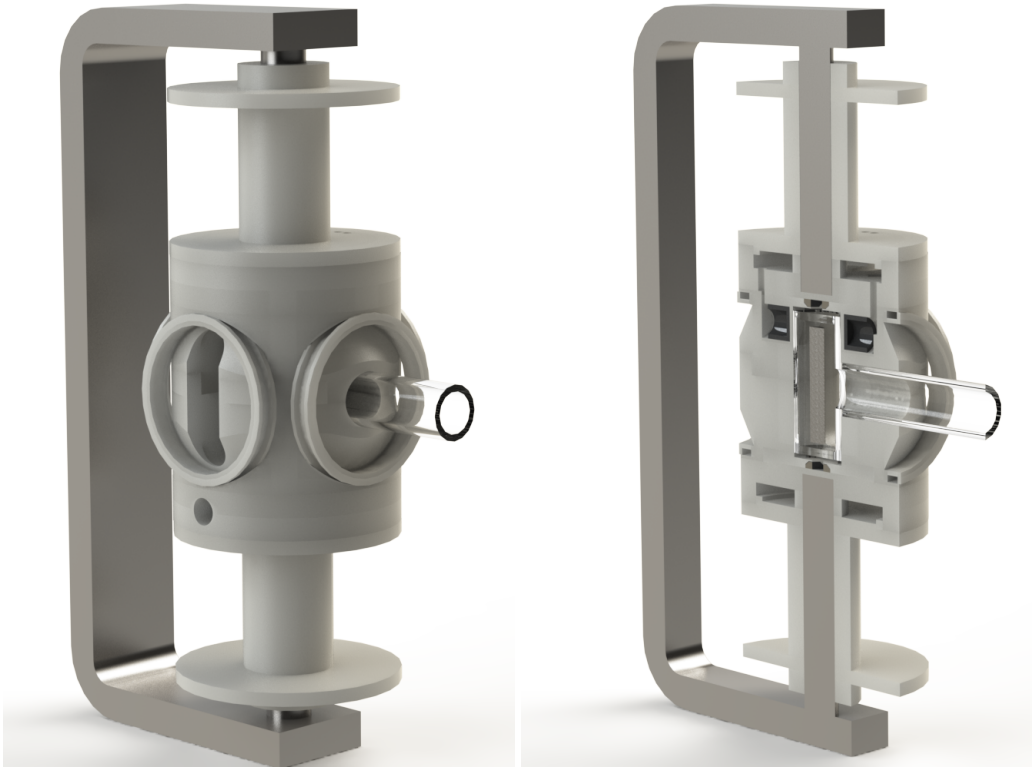

(a) Assembled system (b) Cutaway view of the assembled system

Figure 6.24: *SolidWorks*^{TM} 3D render of all the built parts of the system.

Besides the steel magnetic circuit and the glass enclosure, the system is comprised of ten independently 3D printed parts: two identical big coil supports for the upper and the lower levitation coils, four identical coil supports for the driving coils, two central parts that fit around the glass enclosure and together form the body of the instrument where the lateral damping coils also fit and two lids that fit into the top and bottom of the body, holding the Hall sensors, and the top one also holding the LED-phototransistor pair.

All the parts fit together as seen in figure 6.24. The parts fit together nicely but to clamp everything together the coil's magnetic cores enter through two threaded holes in the magnetic circuit and were screwed into place, holding the parts together. The magnetic circuit is locked into an acrylic glass base with three adjustable feet, for the alignment of the instrument's vertical axis.

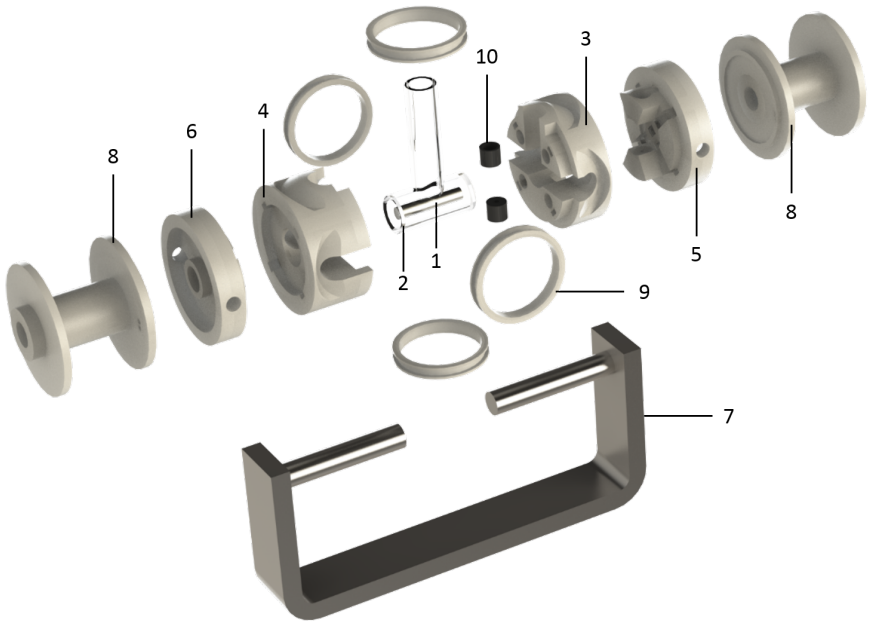

Figure 6.25: *SolidWorks*^{TM} 3D rendered exploded view. 1 - rotor; 2 - glass enclosure; 3 - upper body*; 4 - lower body*; 5 - upper lid*; 6 - lower lid*; 7 - magnetic circuit; 8 - two identical upper and lower coil supports*; 9 - one of four drive coil supports*; 10 - cylindrical holders of the LED-phototransistor of the vertical stabilization circuit (* 3D printed parts).

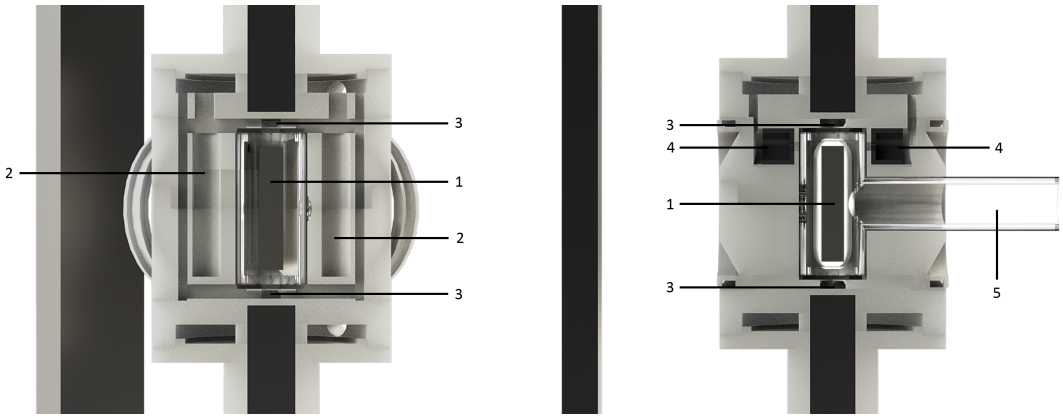

(a) Cutaway view in one of the lateral stabilization planes

(b) Cutaway view of the optical stabilization plane

Figure 6.26: *SolidWorks*^{TM} 3D rendered cutawy views. 1 - rotor; 2 - lateral stabilization coil slots; 3 - Hall sensor slots; 4 - LED-phototransistor pair slots; 5 - vacuum entrance. All the rest vacant space was used for the necessary wiring.

The 3D printing was made with Polylactic acid, a biodegradable thermoplastic aliphatic polyester (PLA). Except the LED-phototransistor holders, which where machined in the workshop from black Ertalon, to ensure a tight fit with the components and to block external infrared interference.

The inner glass enclosure was made by request, and the process of building it with

the cylindrical rotor inside was not trivial. First, two tubes were welded in the "T" shape, and one end of the "T" was closed. Then, the other end was partially closed, leaving a hole big enough for the insertion of the rotor. After the insertion of the rotor, the end of the enclosure was completely closed with the rotor inside. A final annealing of the part concluded the process. This way the rotor's heat exposure to the welding of the glass was minimized.

The surface of the rotor became visibly oxidized, which was not problematic and was even taken advantage of in the rotation frequency measurement, since it introduced optical irregularities. However, it could be quite problematic if the heat exposure changed the rotor's magnetic characteristics, thus the carefulness with the welding process of the glass.

6.8 Vacuum Setup

Finally, in order to validate the instrument it was necessary to connect it to a vacuum system so it could generate different pressure measurements, which is depicted in figure 6.27.

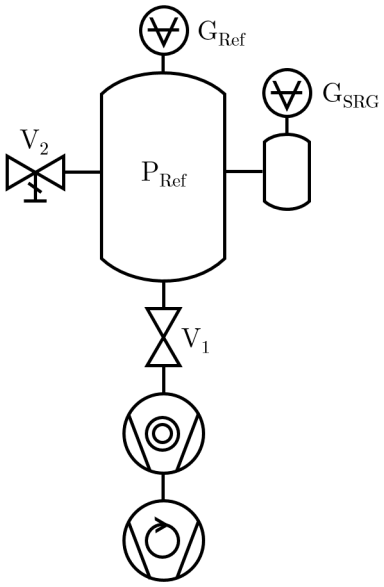

Figure 6.27: Diagram of the vacuum system.

The turbomolecular pump, supported by the rotary pump, is capable of generating high vacuum (<10^{-5} mbar) which is more than enough to test the device. Valve V_1 is useful to allow the pressure to raise without having to shut down the turbomolecular pump, and the needle valve V_2 not only allows for faster pressure increase and overall control, but is also critical to generate static pressures.

A dual transducer with a microPirani and a piezoelectric pressure gauges, G_{Ref}, was connected to the main chamber and used as a non calibrated reference gauge, with a

low pressure limit of 10^{-5} mbar. The prototype, G_{SRG}, was connected to the vacuum chamber through its glass enclosure entrance, with 9 mm of intern diameter, attached to a rubber tube which is connected to the vacuum chamber through to a flexible hose. This connection may have some impact in the device's enclosure pressure, which may be somewhat higher.

CHAPTER 7

RESULTS AND DISCUSSION

The goal at this stage was to test the behaviour of the built prototype by performing pressure measurements and comparing them against a non-calibrated reference gauge, as shown in figure 6.27. Vacuum homogeneity was not studied, which may be responsible for a difference between the measured pressure and the pressure measured by the reference gauge. However, this is not critical since the objective is to prove that the instrument has a consistent and reliable response to different pressure levels, i. e. the instrument's ability to respond to pressure changes.

Assuming that the deduced equation 5.8 is valid, a linear dependence between pressure and the relative deceleration rate is to be expected. Yet, in its deduction, molecular regime was assumed. This means that the equation is not applicable for higher pressures where a saturation effect arises distorting the linearity. Measurements of the deceleration dependence with pressure can be seen in figure 7.1a. Pressures from under 10^{-4} *mbar* to over 10^{1} *mbar* were used, comprising over five orders of magnitude. For this reason the plot uses a log-log scale. To more clearly show the linear dependence, other two close up plots are provided in figures 7.1b and 7.1c.

To obtain this characteristic curve, two different types of measurements were performed constant pressure measurements and continuous pressure measurements. Constant pressure measurements were necessary to obtain good readings at low pressures, where a needle valve was used to maintain a stable constant pressure in the vacuum chamber and then the rotor was left to coast freely for roughly five minutes while its deceleration rate was being recorded. The resulting average deceleration and the stabilized pressure indicated by the reference gauge are used to plot one point in figure 7.1a. An example of such a measurement is shown in figure 7.1d.

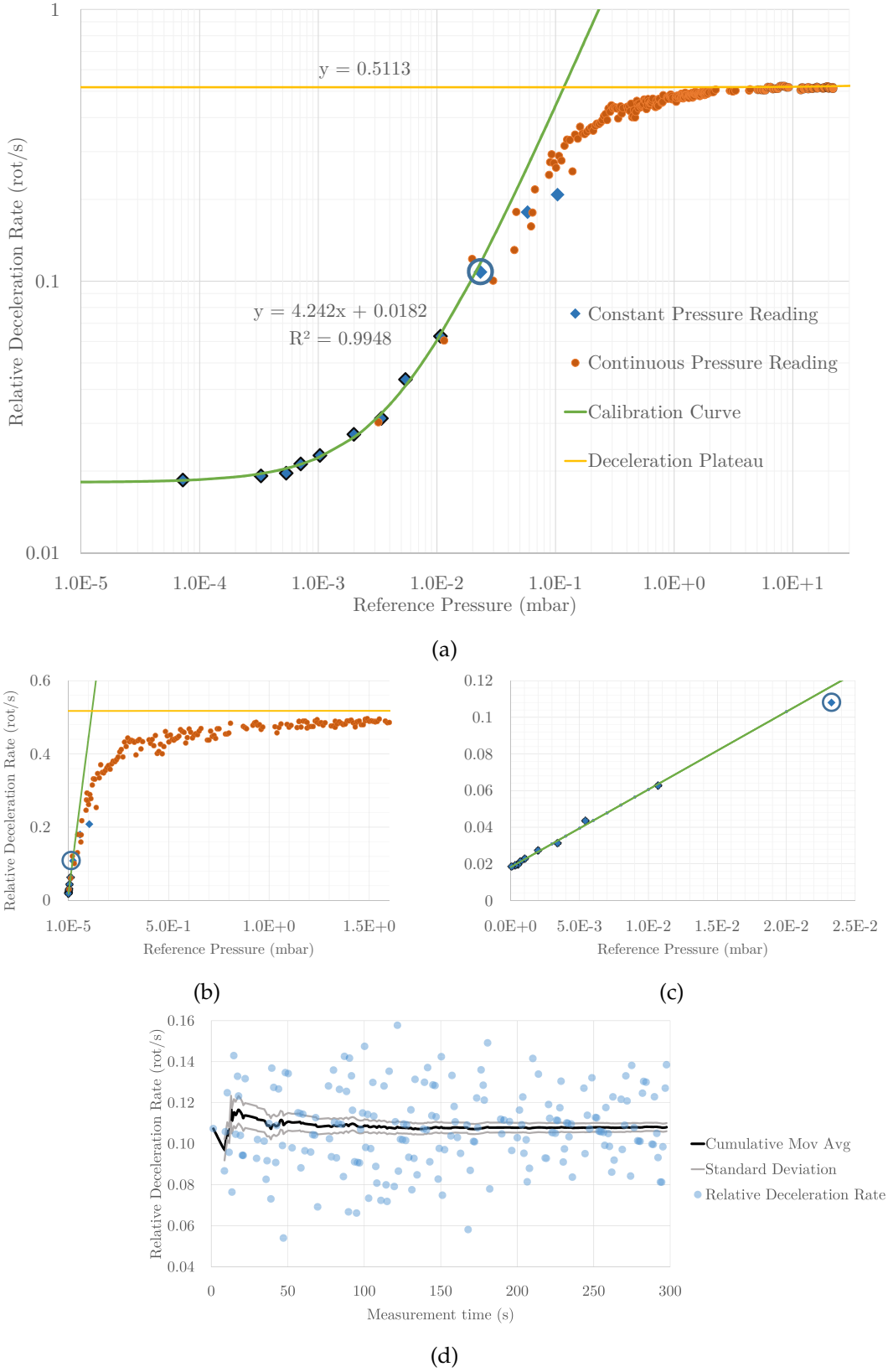

Figure 7.1: The prototype's response to pressure where a) is log-log plot of the whole pressure range and b) and c) are two additional linear close ups. As an example the plot d) shows the acquisition of one constant pressure data point at 2.3×10^{-2} *mbar*. For the sake of clarity this data point is marked with a blue circle in the other plots.

Despite the dispersion of the signal, it is possible to verify in figure 7.1d that the values hang around a stable average. After one minute the cumulative moving average converges to a value quite close to the final reading, and after the two minute mark there are no significant changes in the average value, which is taken as the instrument's response to this pressure level. Using this method, several measurements were preformed between 10^{-1} and 7×10^{-5} $mbar$.

Besides constant pressure measurements, continuous pressure measurements were also preformed. The method employed consisted of obtaining a very low pressure in the vacuum chamber ($< 10^5$ $mbar$), closing the connection to the vacuum pump and allowing the pressure to steadily rise. The output rate of the instrument was set to be around one value per second, which means that some dispersion in the readings is to be expected, as was already verified in the static measurements. This method aimed to characterize the behaviour of the deceleration rate for higher pressures.

These results are in agreement with the expected behaviour and the results obtained by Fremery shown in the figure 7.2.

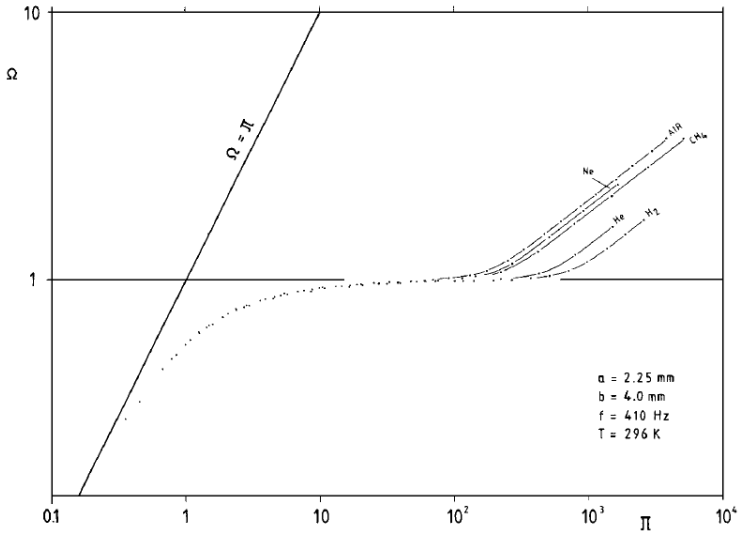

Figure 7.2: Fremerey's SRG normalized characteristic curve of relative deceleration ($\Omega = (-\dot{\omega}/\omega)/(-\dot{\omega}/\omega)_{sat}$) vs pressure ($\Pi = p/p_{sat}$) [42].

Like Fremerey's results, there is a linear range of operation for lower pressures where the deduced equation 5.8 is applicable, and then there is a deceleration saturation plateau at higher pressures. The figure 7.2 showing Fremerey's results goes to even higher pressures beyond the saturation plateau that are out of the testing scope of the prototype.

All things considered, the prototype's calibration curve was thus obtained in figure 7.1.

$$\frac{\dot{\omega}}{\omega} = 4.242 \times p + 0.0182 \qquad (rot/s) \tag{7.1}$$

Where the pressure is in *mbar*. This is a very interesting outcome since it means that it is in fact possible to use this prototype as a pressure gauge.

However, this is a very different result from the calculated expression in equation 6.8.

$$\frac{\dot{\omega}}{\omega} = 2.99 \times 10^2 \; p \qquad (rot/s) \tag{7.2}$$

Where the pressure is in *mbar*. The large offset of two orders of magnitude was quite puzzling. There is quite possibly lack in homogeneity in the vacuum system creating a difference in pressure between the SRG's glass enclosure and the vacuum chamber, as was already mentioned, but which is not expected to cover for such a wide discrepancy.

Another possibility is the induction of unforeseen eddy currents. Given that the rotor used is significantly bigger than the respective commercial counterpart, it is possible that eddy current effects become considerably larger. Theoretically, in a perfectly symmetric system this effect would not be much of a problem, but this is hardly the case. In the SRG-2's manual by MKS it is possible to verify that the system has an angular tolerance of 1^o degree in the alignment of the vertical symmetry axis as shown in figure 7.3. It is only expectable that this tolerance is much smaller for bigger cylindrical rotors.

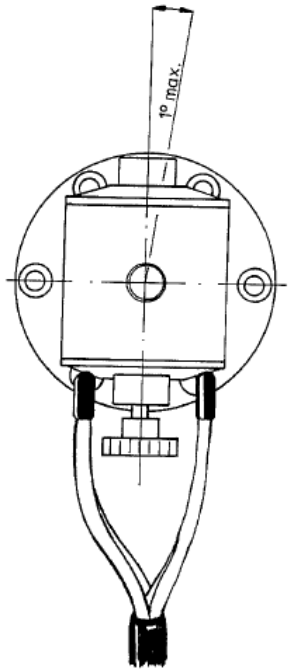

Figure 7.3: Angle tolerance of the spinning rotor gauge [57].

The prototype's head mount has three adjustable feet for alignment purposes. Since the visibility to the inside of the glass chamber is distorted by the glass, the vertical adjustment was performed with the rotor suspended by turning the lower levitation coil on and off. The rotor would hang perfectly vertical with the lower coil shut off, like a pendulum, and

tilt with and angle in the lower coil direction when it was on. The three feet were then adjusted until no tilt was observed when changing states. This is probably not enough to ensure a vertical alignment, even more so if its position is somehow changed by accident amid measurements.

The figure 7.4 comes from a study by Lindenau and colleagues on the effects of misalignment of the SRG [58].

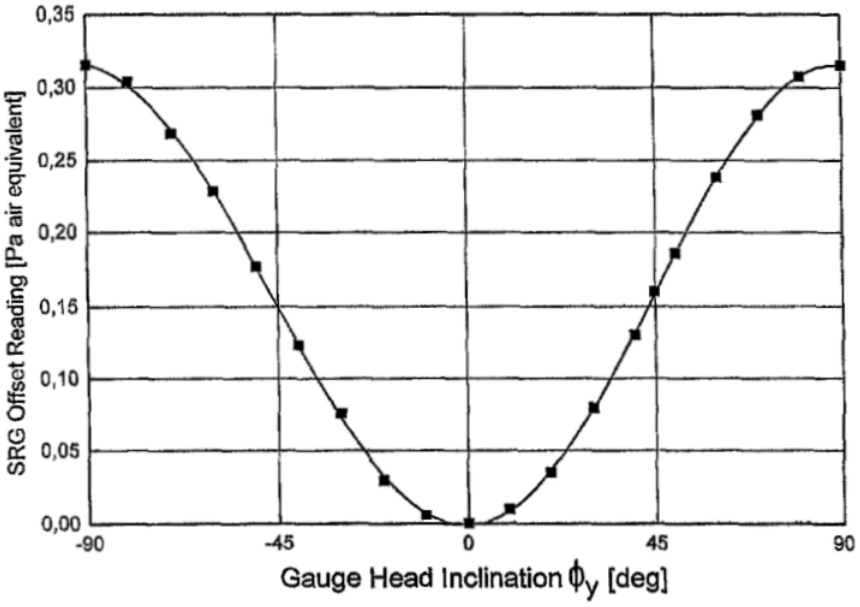

Figure 7.4: Eddy current induction drag dependence on the angle of the SRG's head.

Lindenau's highly optimized SRG has an extra drag offset of up to 0.3 Pa (3×10^{-3} $mbar$) in equivalent pressure. However, besides the incomparable levels of optimization between Lindenau's SRG and the built prototype, the use of a high cylinder is a big disadvantage when it comes to eddy current induction. Not only the much higher volume results in more current induction, but also means that any small angular tilt displaces the lower end of the rotor from the symmetry axis of the instrument, creating the perfect environment for the generation of eddy currents.

All previously measurements were performed at an initial frequency of 400 Hz, which is the nominal working frequency of the commercially available SRG. However, very preliminary tests seem to indicate that higher initial frequencies tend to increase the rotor's drag, creating an unpredicted dispersion of the instrument's readings based on the initial frequency of the rotor. This is yet another indication that the extra drag comes from eddy currents, given that eddy current induction is expected to increase with the frequency of rotation.

7.1 Magnetic Levitation Stability

The magnetic stability was good enough to achieve complete macroscopic stability, i. e. when in suspension no vibrations were observed in the rotor. Despite not being visible to the naked eye, in the oscilloscope it is possible to observe the vertical stabilization signal correcting small displacements.

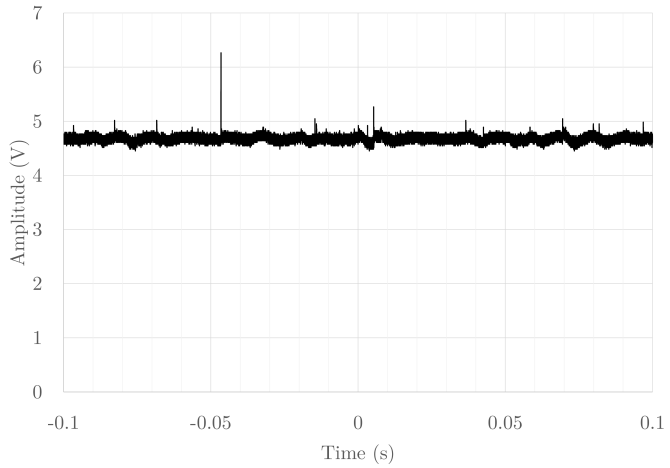

Figure 7.5: Output signal of the vertical stabilization circuit (TP node in figure 6.3) with no rotation.

The signal has a typical amplitude of 0.4 V. If it is taken into account that this signal has a dynamic range of roughly 14 V, from the LED's infrared light being completely blocked to being completely unblocked in its 2 mm window, it is reasonable to assume that the displacements are of the order of 50 μm. In fact, it is unclear how much of this amplitude is simply due to noise in the signal, which means that the displacements are probably smaller than this value. For comparison, the same signal was measured with the lower levitation coil turned on.

As expected, the extra pull downwards forces the upper coil to increase its magnetic field, and consequentially the average output signal increases from 4.68 V to 4.9 V. This also stiffens the levitation, increasing both uppwards and downwards forces, and further improves the stability of the system. On the other hand, the system seemed to be more susceptible to exterior interference, for this reason the coil was shut off during pressure measurements.

Nevertheless, this coil is necessary to start the driving system because of an angular vibration resonance around the 12 Hz mark. To surpass this obstacle, the acceleration process would start with the lower coil on, which changes the resonance frequency to slightly higher values (around 14 Hz). As soon as the rotor would enter the new resonance range the coil would be turned off, changing the resonance frequency back to its original frequency, which would already be surpassed by then. From there the rotor is stabilized by the lateral damping circuit, and further accelerated by the driving circuit.

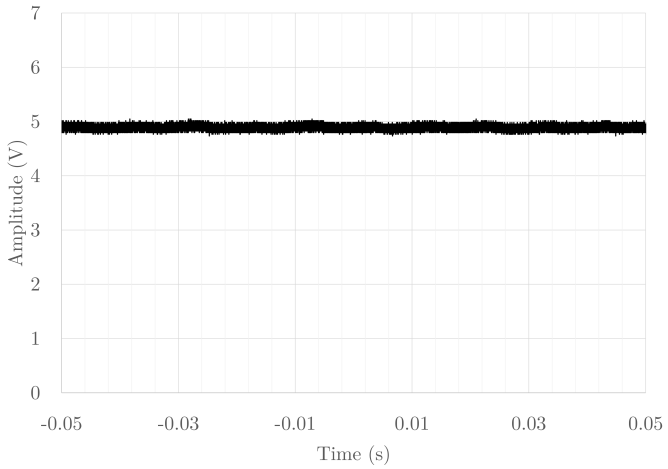

Figure 7.6: Output signal of the vertical stabilization circuit (TP node in figure 6.3) with lower levitation coil turned on and no rotation.

Despite achieving good results in static magnetic suspension, a rather surprisingly different output signal was observed with a rotation rotor.

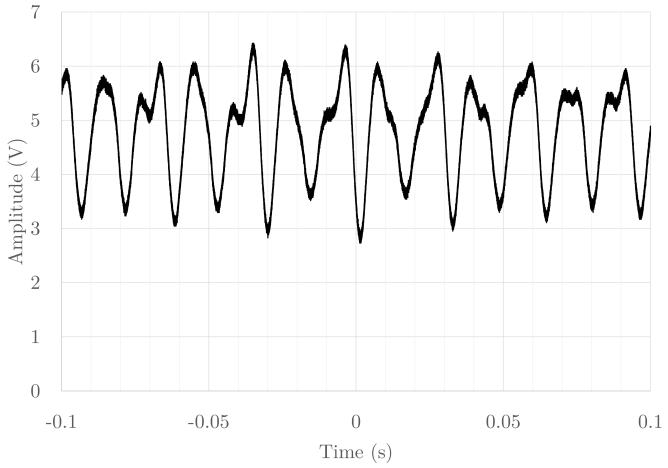

Figure 7.7: Output signal of the vertical stabilization circuit (TP node in figure 6.3) with a rotating rotor and with the driving system shut off.

This output signal follows clearly the rotation frequency which is different from the driving system frequency because of the slip of the induction motor discussed in section 6.4. Given that the suspension circuit works by optical sensing, no crosstalk between systems was expected. Probably, the cause for this interference lays in the lateral damping system.

7.2 Lateral Damping

Ideally, the horizontal damping would only act laterally, and not vertically, but this is impossible. In fact, the horizontal component of the magnetic field is being picked up by the Hall sensors, causing the lateral damping circuit to respond with a periodic signal with the rotation frequency.

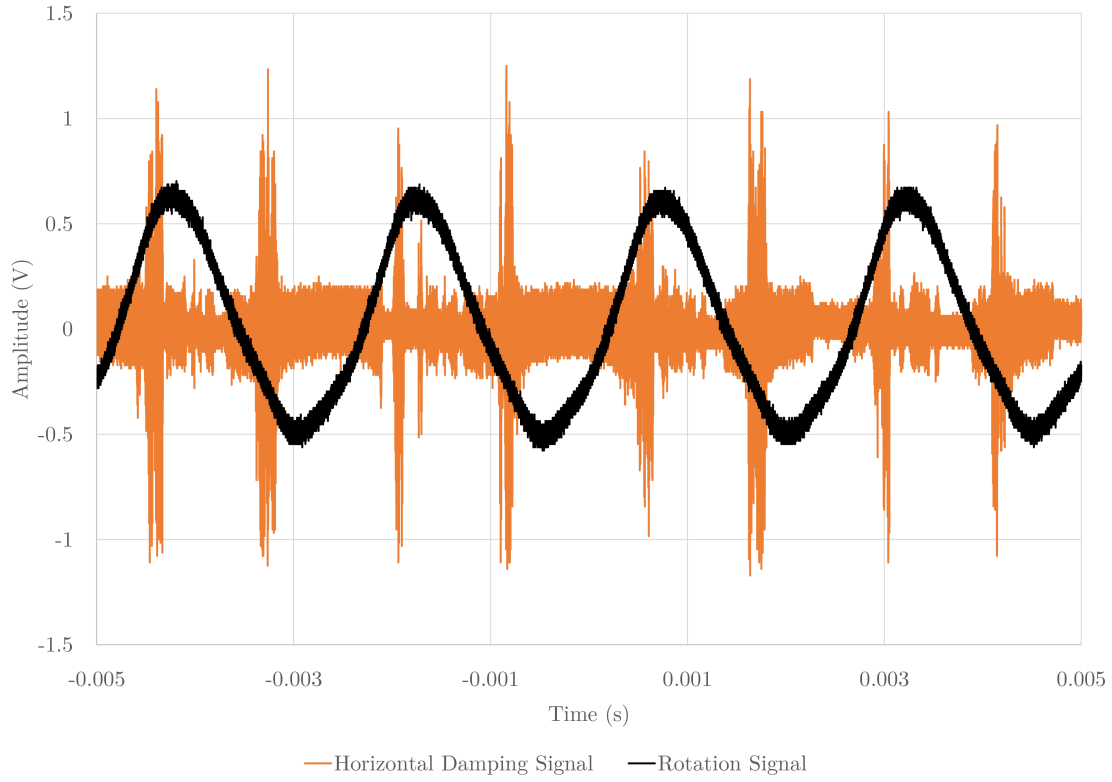

Figure 7.8: The rotation signal, In black, is compared to the lateral damping signal, in orange, at 400 Hz.

In figure 7.8 it is possible to confirm two lateral correction peaks per rotation, corresponding to the alignment and anti-alignment of the magnetic poles of the rotor with the Hall sensors.

Every lateral correction force comes with an unwanted vertical component, thus interfering with the vertical stabilization circuit. Despite this interference, the suspension circuit seems to respond accordingly, keeping the object macroscopically stable. The high angular momentum of the rotor has also probably a significant role in keeping the rotor stable.

After all these considerations, it seemed reasonable to assume that the lateral damping system was causing the discrepancy in the pressure readings, by causing extra drag while performing its lateral damping function.

To test this possibility, four constant-pressure measurements were preformed at

roughly 1.5×10^{-3} and 4×10^{-4} mbar, two with the lateral damping system on, and two off. The results can be seen in figure 7.9.

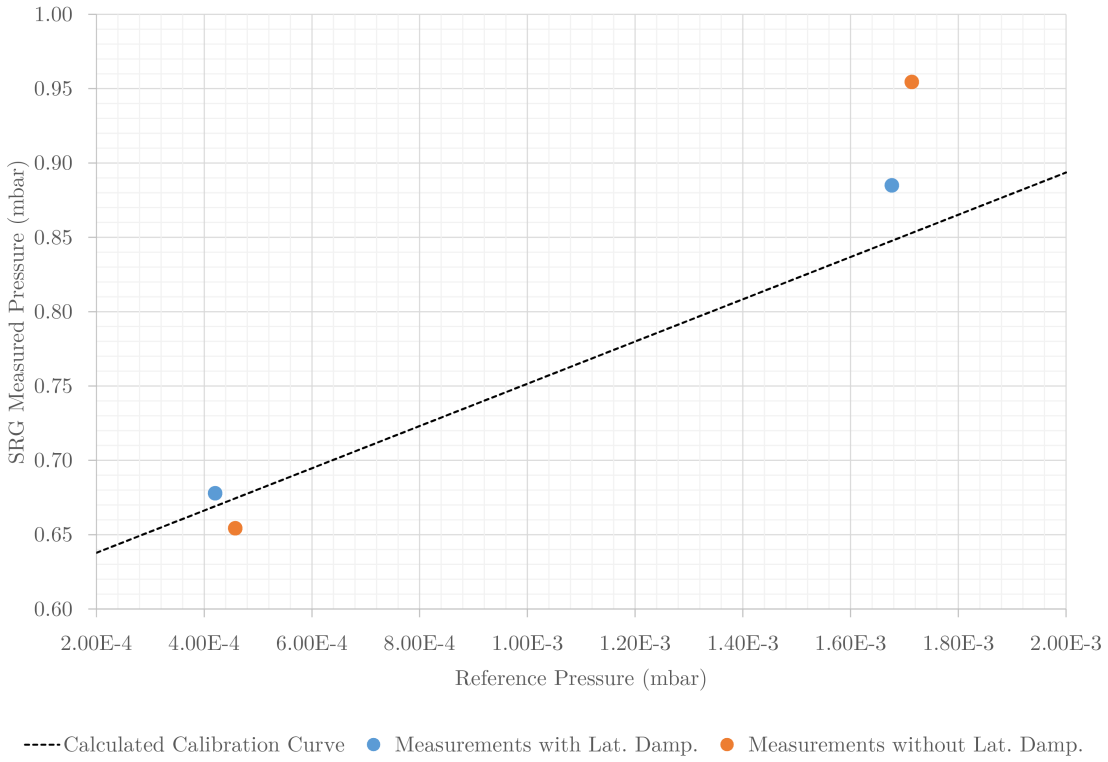

Figure 7.9: Measurement of the impact of the horizontal damping in the pressure readings.

If the lateral damping system was responsible for the extra drag, the pressure reading with the system shut off would be expected to be lower. However, there does not seem to be any correlation linking the deceleration rate with this system, or at least it is not an obvious connection. Note that, without lateral damping, the rotor starts to pick up vibrations after some time.

7.3 Driving System

In order to measure the performance of the driving circuit, the rotor was accelerated from 100 Hz to the high frequency limit of the system, which is close to 800 Hz. At this last frequency, there is an angular vibration resonance to which the lateral damping circuit is not prepared to respond efficiently. These vibrations increase to the point where the rotor collides with the glass enclosure, stopping the rotor's acceleration.

The drive circuit is capable of a steady acceleration of 30 Hz per min. The higher moment of inertia of the rotor, when compared to the typical SRG smaller rotor, makes the acceleration process slower. But the rotation circuit also has some limitations, mainly because of the coils used.

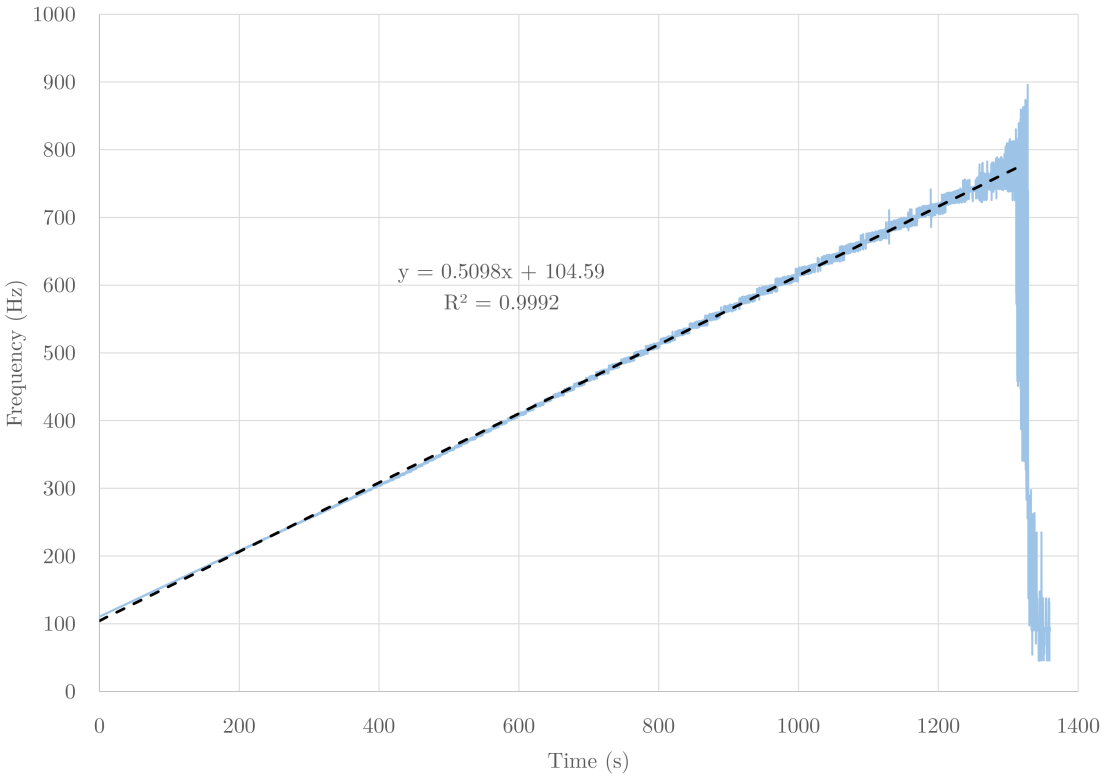

Figure 7.10: Acceleration of the rotor from 100 Hz to the upper frequency limit around 750 Hz.

7.4 Frequency Detection

The frequency detection circuit only makes accurate measurements for frequencies above 75 Hz. This is due to the fact that the optical signal only takes a cleaner sinusoidal shape for higher frequencies, whereas for lower frequencies the signal is more irregular, and crosses the trigger level multiple times per rotation giving false readings. The increasing cleanliness of the signal for higher frequencies can be seen in figure 7.11.

This is a consequence of a low pass filter effect in the signal treatment, and as a consequence, the amplitude of the signal decreases with rotor's frequency. This is not of critical importance as long as a clean triggered signal is obtained at operation frequencies, which for 400 Hz couldn't be better.

In the present prototype, the frequency measuring circuit may actually be a redundancy, since it was later discovered that the rotation frequency is present in the vertical stabilization circuit and also in the lateral damping circuit. Nevertheless, it will be pertinent if this interferences are somehow eliminated.

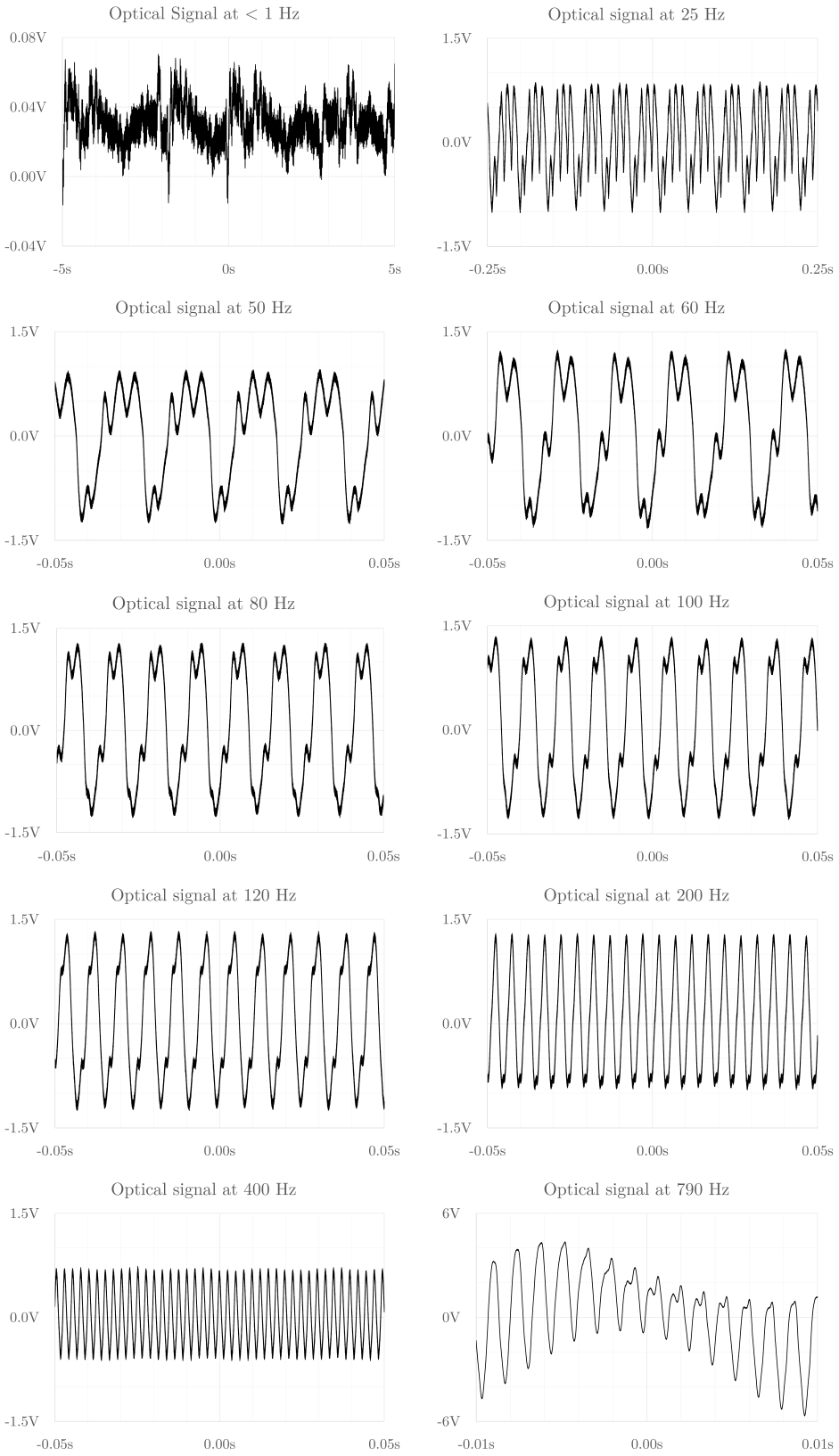

Figure 7.11: Optical signal of the rotation frequency at different frequencies.

It is also interesting to notice that if the rotor vibrates, this signal captures the vibration frequency, i.e. not only measures the rotation frequency, but can also be used to measure angular vibrations, as long as there is a way to distinguish one frequency from the other. Both frequencies can be seen in the last plot of the figure 7.11, where the rotor was close to its maximum speed at roughly 790 Hz, where it was close to a vibration resonance and was about to collide with the glass enclosure as was shown in the figure 7.10.

CHAPTER 8

CONCLUSIONS AND FUTURE PERSPECTIVES

A new spinning rotor gauge based on a cylindrical rotor was proposed, successfully implemented and tested. Different approaches were tested through several iterations, resulting in a final prototype, which was used to make pressure measurements.

The main objective of verifying a linear response of the relative deceleration rate with pressure was successful, and pressure measurements were preformed from 10^{-4} mbar up to 10^{2} mbar. Yet, the observed linear response of the instrument does not agree with the theoretical expectations, which seems to indicate the presence of unforeseen extra drag. The most likely explanation for this extra drag is based on eddy current induction within the rotor, which is possibly related to an inadequate alignment of the device, given that asymmetries in the system augment the loss of energy by eddy currents.

The magnetic suspension, however, is achieved with great stability, with displacements under the 50 μm range, but also with the possibility of achieving even better stability by making use of the lower vertical coil.

The lateral damping system is quite effective in keeping the rotor still, except when the rotation frequency goes through two resonance frequencies at $\sim$ 13 Hz and $\sim$ 800 Hz. The first frequency can be coped with by changing the strength of suspension magnetic field with the lower vertical coil amid the acceleration process, changing the resonance location, while the other was not possible to avoid and ultimately represents the system's upper frequency limit. Being a completely new system, since the angular stability of the cylindrical rotor has to be treated differently from a spherical one, it could cause the extra drag measured, but as far as it was possible to test with the current setup, this was not the case.

The driving system, which works similarly to an induction motor, is capable of an acceleration of 30 Hz/min, which is more than enough for the prototype's purposes.

This project was a start for what hopefully will develop into a continuous line of investigation regarding the spinning rotor gauge. Being an exploratory work, there are innumerable aspects of the prototype that can be optimized. However, a more in depth understanding of this complex system can only be attained with more extensive work.

There are several aspects in which the prototype can be improved. For one, the magnetic suspension system does not make active use of the lower vertical coil. The rotor stability would probably be significantly improved even further if this coil was controlled by an active feedback system similar to the one responsible for the upper levitation coil. The vertical position detection based on a LED-phototransistor pair worked as intended for a first approach. However, in the future there is interest in testing different rotors, and as such it is important to make the swapping of rotors easier. The optical sensing system requires a glass enclosure, making the system less versatile. To avoid this problem, the vertical position sensing should be obtained like in the SRG, by sensing the coil's inductance in response to the proximity of the rotor.

Still in the topic of versatility, the driving coils should have a bigger inner diameter to allow the swapping of rotor similarly to the SRG. Besides, the used coils limited severely the maximum driving frequency because of their high inductance. In the future new driving coils with lower inductance should be used, which would boost the acceleration of the system.

The lateral damping system works as intended except at resonance frequencies. This system could have extra bandpass filters targeting the specific resonance frequencies, which could possibly improve the upper limit rotation frequency of the instrument. However, for different rotors the resonance frequencies are going to be located at different points in the frequency spectrum, meaning that this optimization may not be of interest when testing different rotors as the filters would have to be tuned for every different rotor.

Despite all the future improvements that could be made to the prototype, the most pertinent short term investigation would be the identification of the measured extra drag. It would be interesting to measure the misalignment effect on the pressure reading, for which a better way to control the orientation of the instrument should be provided.

Finally, it would be interesting to see if the frequency of the rotor can be influenced by radiation pressure and if there could be other uses for this effect.

BIBLIOGRAPHY

[1] J. C. Keith. "Magnetic torques and Coriolis effects on a magnetically suspended rotating sphere". In: *Journal of Research of the National Bureau of Standards, Section D: Radio Propagation* 67D.5 (1963), p. 533. ISSN: 1060-1783. DOI: 10.6028/jres.067D.056.

[2] J. K. Fremerey. "Apparatus for Determination of Residual Drag Torque on Small Spinning Spheres in Magnetic Suspension". In: *Review of Scientific Instruments* 42.6 (1971).

[3] S. Earnshaw. "On the Nature of the Molecular Forces which Regulate the Constitution of the Luminiferous Ether". In: *Trans. Cambridge Phil. Soc.* 7 (1842), pp. 97–112.

[4] F. Hellman, E. M. Gyorgy, D. W. Johnson, H. M. O'Bryan, and R. C. Sherwood. "Levitation of a magnet over a flat type II superconductor". In: *Journal of Applied Physics* 63.2 (1988), pp. 447–450. ISSN: 00218979. DOI: 10.1063/1.340262.

[5] H. Chetouani, C. Jeandey, V. Haguet, H. Rostaing, C. Dieppedale, and G. Reyne. "IEEE Xplore - Diamagnetic Levitation With Permanent Magnets for Contactless Guiding and Trapping of Microdroplets and Particles in Air and Liquids". In: 42.10 (2006), pp. 3557–3559.

[6] M. Siebert, B. Ebihara, R. Jansen, R. L. Fusaro, W. Morales, A. Kascak, and A. Kenny. *Magnetic Bearing Flywheel*. Tech. rep. February. 2002.

[7] M. D. Simon. "Spin stabilized magnetic levitation". In: *American Journal of Physics* 65.4 (1997), p. 286. ISSN: 00029505. DOI: 10.1119/1.18488.

[8] F. T. Holmes. "Axial Magnetic Suspensions". In: *Review of Scientific Instruments* 8.11 (1937), p. 444.

[9] W Jones. "Earnshaw's theorem and the stability of matter". In: *European Journal of Physics* 1.2 (1980), p. 85.

[10] B. Jayawant. "Electromagnetic suspension and levitation". English. In: *IEE Proceedings A (Physical Science, Measurement and Instrumentation, Management and Education, Reviews)* 129 (8 1982), 549–581(32). ISSN: 0143-702X.

[11] M. V. Berry and a. K. Geim. "Of flying frogs and levitrons". In: *European Journal of Physics* 18.4 (1999), pp. 307–313. ISSN: 0143-0807. DOI: 10.1088/0143-0807/18/4/012.

[12] R. Evrard. "An Absolute Micromanometer Using Diamagnetic Levitation". In: *Journal of Vacuum Science and Technology* 6.2 (Mar. 1969), p. 279. ISSN: 00225355. DOI: 10.1116/1.1492679.

[13] Z. Novak and M. Hofreiter. "Mendocino motor and a different approaches to its control". In: *MECHATRONIKA, 2012 15th International Symposium*. 2012, pp. 1–6.

[14] Z. Novák. "Controlling speed of motor powered by solar energy". In: *Students conference 2012*. Department of Instrumentation and Control Engineering, Faculty of Mechanical Engineering, Czech Technical University in Prague, Prague, Czech republic. 2012.

[15] L. Spring. *Larry Spring's Magnetic Levitation Mendocino Brushless Solar Motor*. June 2015.

[16] R. F. Post and D. D. Ryutov. "Inductrack: A simpler approach to magnetic levitation". In: *IEEE Transactions on Applied Superconductivity* 10.1 (2000), pp. 901–904. ISSN: 10518223. DOI: 10.1109/77.828377.

[17] L. S. Tung, R. F. Post, E. Cook, and J. Martinez-Frias. "The NASA Inductrack Model Rocket Launcher at the Lawrence Livermore National Laboratory". In: *Fifth International Symposium On Magnetic Suspension Technology*. 2001, pp. 93–98.

[18] J. K. Fremerey and K Boden. "Active permanent magnet suspensions for scientific instruments". In: *Journal of Physics E: Scientific Instruments* 11.2 (1978), p. 106.

[19] D. Cho, Y. Kato, and D. Spilman. "Sliding mode and classical controllers in magnetic levitation systems". In: *Control Systems, IEEE* 13.1 (1993), pp. 42–48. ISSN: 1066-033X. DOI: 10.1109/37.184792.

[20] I. Echeverria and M. a. Rubio. "High-precision magnetic levitation device with electro-optical feedback". In: *Review of Scientific Instruments* 66.7 (1995), p. 3931. ISSN: 00346748. DOI: 10.1063/1.1145397.

[21] J. P. Looney, F. G. Long, D. F. Browning, and C. R. Tilford. "PC-based spinning rotor gage controller". In: *Review of Scientific Instruments* 65.9 (1994).

[22] a. Charara, J. De Miras, and B. Caron. "Nonlinear control of a magnetic levitation system without premagnetization". In: *IEEE Transactions on Control Systems Technology* 4.5 (1996), pp. 513–523. ISSN: 10636536. DOI: 10.1109/87.531918.

[23] a. El Hajjaji and M. Ouladsine. "Modeling and nonlinear control of magnetic levitation systems". In: *IEEE Transactions on Industrial Electronics* 48.4 (2001), pp. 831–838. ISSN: 02780046. DOI: 10.1109/41.937416.

[24] N. F. Al-Muthairi and M. Zribi. "Sliding mode control of a magnetic levitation system". In: *Mathematical Problems in Engineering* 2004.2 (2004), pp. 93–107. DOI: 10.1155/S1024123X04310033.

[25] Z.-J. Yang and M. Tateishi. "Adaptive robust nonlinear control of a magnetic levitation system". In: *Automatica* 37.7 (2001), pp. 1125 –1131. ISSN: 0005-1098. DOI: http://dx.doi.org/10.1016/S0005-1098(01)00063-2.

[26] J. W. Beams and S. a. Black. "Electrically-Driven Magnetically-Supported Vacuum-Type Ultracentrifuge". In: *Review of Scientific Instruments* 10.2 (1939), p. 59.

[27] J. W. Beams, J. D. Ross, and J. F. Dillon. "Magnetically Suspended Vacuum-Type Ultracentrifuge". In: *Review of Scientific Instruments* 22.2 (1951), p. 77.

[28] J. W. Beams, C. W. Hulburt, W. E. Lotz, and R. M. Montague. "Magnetic Suspension Balance". In: *Review of Scientific Instruments* 26.12 (1955), p. 1181.

[29] J. Fremerey. "Application of the magnetic suspension technique in vacuum and surface physics". In: *Vacuum* 40.1-2 (Jan. 1990), pp. 19–22.

[30] J. K. Fremerey. "Spinning rotor vacuum gauges". In: *Vacuum* 32.10 (1982), pp. 685 –690. ISSN: 0042-207X. DOI: http://dx.doi.org/10.1016/0042-207X(82)94048-9.

[31] J. W. Beams, J. L. Young, and J. W. Moore. "The Production of High Centrifugal Fields". In: *Journal of Applied Physics* 17.11 (1946), p. 886.

[32] J. W. Beams. "Magnetic Suspension for Small Rotors". In: *Review of Scientific Instruments* 21.2 (1950), p. 182.

[33] J. W. Beams. "High-Speed Rotation". In: *Physics Today* 12.7 (1959), p. 20.

[34] J. W. Beams. "Double Magnetic Suspension". In: *Review of Scientific Instruments* 34.10 (1963), p. 1071.

[35] J. W. Beams, D. M. Spitzer, and J. P. Wade. "Spinning Rotor Pressure Gauge". In: *Review of Scientific Instruments* 33.2 (1962), p. 151.

[36] T. Reichert, T. Nussbaumer, and J. W. Kolar. "Complete analytical solution of electromagnetic field problem of high-speed spinning ball". In: *Journal of Applied Physics* 112.10 (2012), p. 104901.

[37] L. E. MacHattie. "The Production of High Rotational Speed". In: *Review of Scientific Instruments* 12.9 (1941), p. 429.

[38] R. Lord and P. Harbour. "The Aerodynamic Drag Torque on a Rotating Sphere in the Transition Regime". In: *Rarefied Gas Dynamics, Volume 1*. Vol. 1. 1965, p. 611.

[39] R. Lord. "Tangential momentum accommodation coefficients of rare gases on polycrystalline metal surfaces". In: *Rarefied gas dynamics* (1977), pp. 531–538.

[40] L. B. Thomas and R. Lord. "Comparative measurements of tangential momentum and thermal accommodations on polished and on roughened steel spheres". In: *Rarefied gas dynamics* 8 (1974), pp. 405–412.

[41] W Steckelmacher. "On the theory of viscosity vacuum gauges". In: *Vacuum* 23.5 (1973), pp. 165–169.

[42] J. K. Fremerey. "The spinning rotor gauge". In: *Journal of Vacuum Science and Technology A* 3.3 (1985), pp. 1715–1720. DOI: http://dx.doi.org/10.1116/1.573007.

[43] J. Fremerey and B. Lindenau. *Coil system for inductive measurement of the velocity of movement of a magnetized body*. US Patent 4,658,658. 1987.

[44] J. Fremerey and B. Lindenau. *Coil system for inductive measurement of the velocity of movement of a magnetized body*. CA Patent 1,231,255. 1988.

[45] B. Lindenau, J. Fremerey, and K. Witthauer. *Gas-friction vacuum indicator with a gas-friction sensor rotating about a fixed axis of rotation*. US Patent 5,777,233. 1998.

[46] J. Fremerey. *Rotor device*. CA Patent 2,369,956. 2007.

[47] H. Isogai. "An analysis of the effects of eddy currents on the accuracy of a Spinning Rotor Gauge". In: *Vacuum* 48.2 (1997), pp. 175 –179. ISSN: 0042-207X. DOI: http://dx.doi.org/10.1016/S0042-207X(96)00297-7.

[48] J. K. Fremerey. "Residual Drag Torque on Magnetically Suspended Rotating Spheres". In: *Review of Scientific Instruments* 43.10 (1972), p. 1413.

[49] J. K. Fremerey. "Significant Deviation of Rotational Decay from Theory at a Reliability in the 10^{-12} sec^{-1} Range". In: *Phys. Rev. Lett.* 30 (16 1973), pp. 753–757. DOI: 10.1103/PhysRevLett.30.753.

[50] E. Frehland. "Critique of the gravitational radiation damping effects calculated by Keith". English. In: *Lettere al Nuovo Cimento (1971-1985)* 7.12 (1973), pp. 490–492. DOI: 10.1007/BF02727861.

[51] *Instruction Manual - SRG 3 - Spinning Rotor Gas Friction Vacuum Gauge*. URL: http://www.mksinst.com/docs/R/SRG-3-man.pdf. MKS Instruments, Inc.

[52] *What do 'high vacuum' and 'low vacuum' mean?* URL: http://www.npl.co.uk/reference/faqs/what-do-high-vacuum-and-low-vacuum-mean-(faq-pressure). Accessed: 18-02-2015.

[53] J. F. O'Hanlon. *A User's Guide to Vacuum Technology*. Third Edit. Wiley InterScience, 2003. ISBN: 3175723993.

[54] W. Jitschin, J. Migwi, and G. Grosse. "Gauge calibration in the high and medium vacuum range by a series expansion standard". In: *Vacuum* 41.7-9 (1990), pp. 1799–1801. ISSN: 0042207X. DOI: 10.1016/0042-207X(90)94096-9.

[55] V Odnoralov. “Employment of Continuous Expansion Method for Vacuum Gauge Calibration in Medium Vacuum Range”. In: *Revista Brasileira de Aplicações de Vácuo* 24.2 (2005), pp. 110–116. DOI: http://dx.doi.org/10.17563/rbav.v24i2.101.

[56] A. E. Fitzgerald, C. Kingsley, and S. D. Umans. *Electric Machinery*. Sixth Edit. McGraw-Hill, 2003. ISBN: 0073660094.

[57] *Instruction Manual - SRG 2 - Spinning Rotor Gas Friction Vacuum Gauge*. MKS Instruments, Inc.

[58] B. Lindenau, J. Fremerey, and K Witthauer. “Spinning rotor gauge for operation at free spatial orientation”. In: *Vacuum* 46.8–10 (1995), pp. 835 –837. ISSN: 0042-207X. DOI: http://dx.doi.org/10.1016/0042-207X(95)00051-8.

APPENDIX A

LIGHT PRESSURE

Light pressure could be an interesting way to deliver the torque to accelerate the rotor of a CSRG, as was already discussed in chapter 5. The mechanism is illustrated in figure A.1.

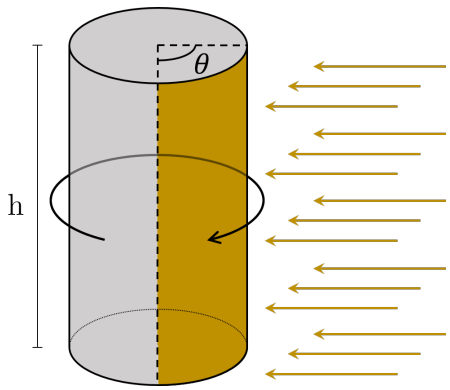

Figure A.1: Diagram of a light-based torque delivery method for the rotor of a CSRG.

The radiation pressure on a given surface can be separated on two different components. The first happens when the photon is absorbed, transferring all of its momentum to the surface. On the other hand, if the photon is reflected, the momentum transferred will depend on the incident angle, meaning that it will vary from virtually no momentum transfer for an angle of 90º with the normal to the surface to the double the amount of the photon's linear momentum if the angle is of 0º, or perpendicular to the surface.

Moreover, in the case of a round surface the transferred momentum may be separated in radial and tangential components. The reflection has virtually no tangential momentum transfer as shown in figure A.2a, whereas the absorption may have the two components depending on the angle of incidence as can be seen in figure A.2b.

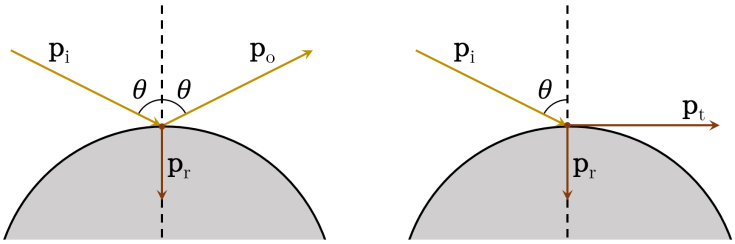

(a) (b)

Figure A.2: Photon incidence with two possible outcomes: a) photon reflection and b) photon absorption.

The radiation pressure is defined by

$$P_l = \frac{S}{c} \tag{A.1}$$

Where s is the irradiance in W/m^2, and c the speed of light. For a sense of scale, a typical value for the sun's irradiance on the earth's surface is of $1000W/m^2$ resulting in a pressure of $3.3 \times 10^{-6} mbar$, which is well inside the operating range of the SRG.

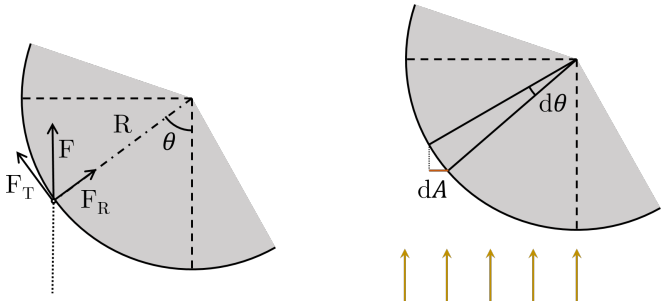

(a) (b)

Figure A.3: Incidence of light for torque delivery where a) represents the different force components of one photon collision and b) the incidence of light with other important parameters for the torque calculation.

From the geometric parameters seen in figure A.3, the torque resulting from the incident beam can be calculated in the following way.

The force exerted by the light pressure P_l is defined by

$$\mathrm{d}F = P_l \, \mathrm{d}A \tag{A.2}$$

However, only the tangential component of the force is able to generate torque.

$$\mathrm{d}\tau = R \, \mathrm{d}F_T \tag{A.3}$$

Where τ is the torque, R the cylinder radius and F_T is the tangential force which depends on the angle of incidence, as shown in figure A.3a.

$$\mathrm{d}F_T = \sin\theta \, \mathrm{d}F \tag{A.4}$$

The tangential force can be replaced in equation A.3.

$$\mathrm{d}\tau = R \sin\theta P_l \, \mathrm{d}A \tag{A.5}$$

$$\tau = \int_0^{\pi/2} R \sin\theta P_l \, \mathrm{d}A \tag{A.6}$$

Where $\mathrm{d}A = hR\cos\theta \, \mathrm{d}\theta$. Note that the $\mathrm{d}A$ considered is not exactly an infinitesimal area from the surface of the cylinder, but is in fact only the horizontal component of it as depicted in figure A.3b. Unlike gas pressure, the light pressure here has direction, meaning that only the perpendicular component of the surface to the said direction actually suffers the pressure.

$$\tau = R^2 P_l h \int_0^{\pi/2} \cos\theta \sin\theta \, \mathrm{d}\theta \tag{A.7}$$

$$\tau = \frac{1}{2} R^2 P_l h \tag{A.8}$$

After replacing the light pressure P_l for its expression from equation A.1, a final result for the torque is obtained.

$$\tau = \frac{sR^2 h}{2c} \tag{A.9}$$

Again, with the light pressure of the sun as a reference 3.3×10^{-6} mbar, and the dimensions of the rotor's prototype, $h = 0.025$ m and $R = 0.0025$ m, the resulting torque is $\tau = 2.6 \times 10^{-13}$ N.m.

Preliminary tests indicate that this torque is not sufficient to overcome the tendency of the rotor to align with the earth's magnetic field, for this reason it is possible that the rotation has to start by some other mechanism.

For comparison, the drag torque from the gas pressure can be easily calculated from the relative deceleration rate equation 5.8.

$$\tau = \frac{2pR^3\omega\sigma}{\bar{c}} \left(R + 2h\right) \tag{A.10}$$

where p is the gas pressure in Pascal, ω is the angular velocity in rad/s, σ is the momentum accommodation which is dimensionless and typically very close do one and $\bar{c}$ is the thermal velocity expressed by

$$\bar{c} = \sqrt{\frac{8kT}{\pi m}} \tag{A.11}$$

The terminal velocity of such a system would only be achieved when both torques from equation A.9 and equation A.10 equal each other.

$$\frac{sR^2h}{2c} = \frac{2pR^3\omega\sigma}{\bar{c}}(R + 2h) \tag{A.12}$$

From this equality results the terminal angular velocity.

$$\omega = \frac{s\bar{c}}{4cp\sigma}\frac{h}{R^2 + 2Rh} \tag{A.13}$$

To estimate of this terminal angular velocity, the typical values from table A.1 were used.

Table A.1: Typical values for the equation A.13.

Variables	Values	Units
σ	1	
h	0.025	m
R	0.0025	m
s	1000	W/m^2
T	293	K
m	$0,029$	kg/mol

$$\omega_t = \frac{7.4 \times 10^{-2}}{p} \qquad (rad/s) \tag{A.14}$$

With the result in SI units (the pressure p is in Pa). For convenience it can be converted to rotations per second and the pressure to $mbar$.

$$f_t = \frac{1.18 \times 10^{-4}}{p} \qquad (rot/s) \tag{A.15}$$

The performance of the light based driving system only considered $1/4$ of irradiated lateral surface of the rotor until now. In fact more light sources could be used as shown in figure A.4, multiplying the irradiated surface as well as the delivered torque.

The figure A.5 shows the resulting terminal velocity variation with pressure with one system and with four.

In one hand, there are several other drag sources that were left out of this calculations that would push the terminal velocity to lower values, but not by much since they can be minimized as discussed in section 3.3. On the other hand this calculations were performed

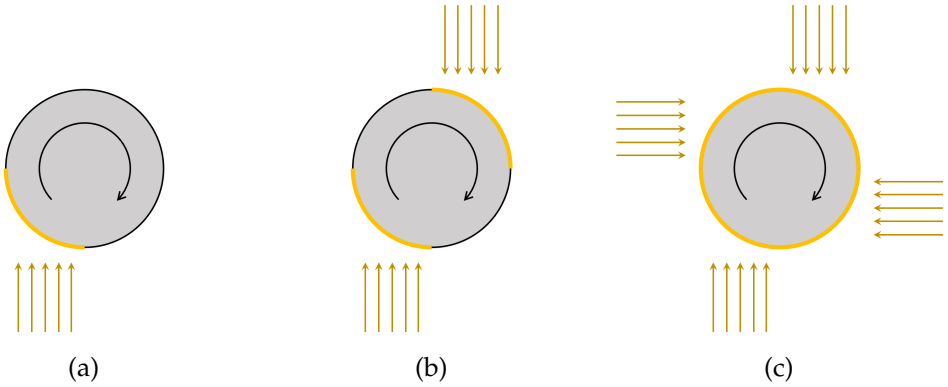

Figure A.4: Three different configurations of the driving system. a) with just one system, b) with two systems and c) with four.

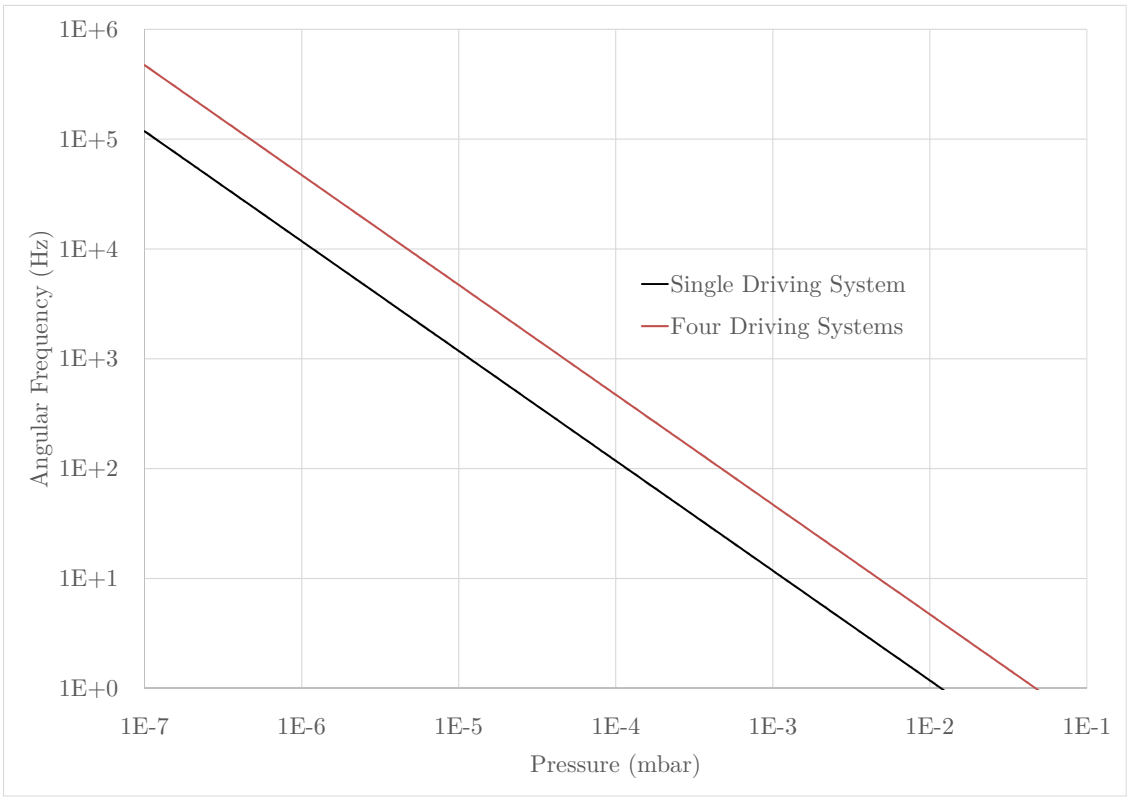

Figure A.5: Terminal angular frequency of a cylindrical rotor driven by a light pressure based mechanism.

with the prototype's rotor in mind, but there is probably a lot of room for optimization here, specially considering the possible improvements to the rotor considered in chapter 5.

Nevertheless, it is possible to verify that the 400Hz are achieved for pressures under 10^{-4} $mbar$, which is the nominal speed of operation of the SRG.

APPENDIX B

TECHNICAL DRAWINGS

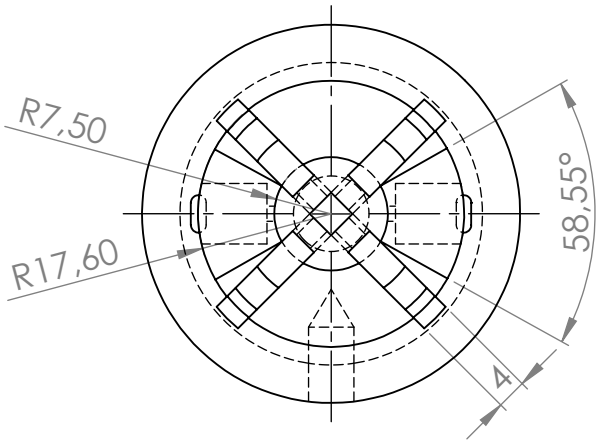

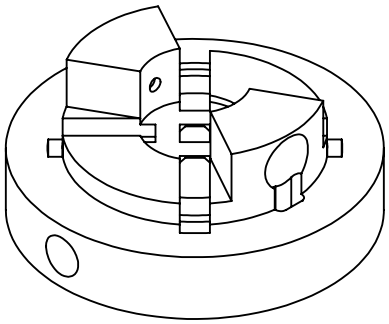

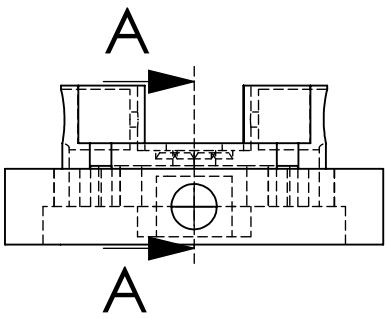

SECTION A-A

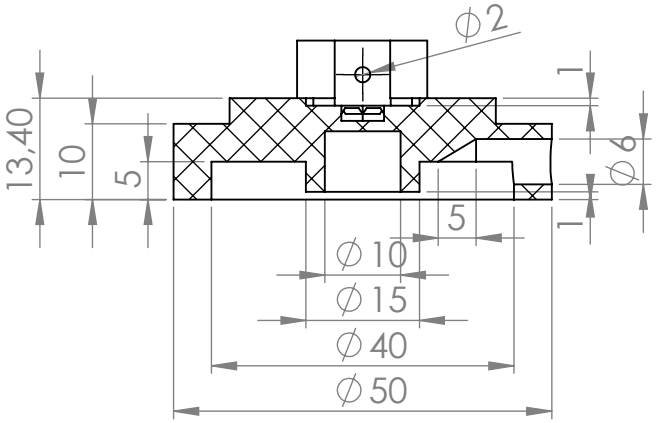

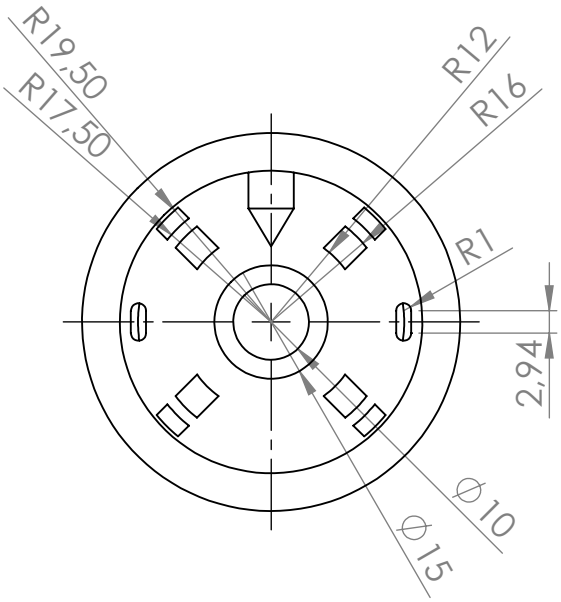

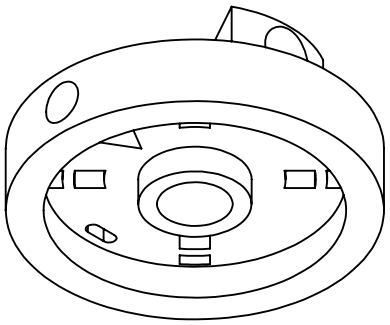

	Name	Date	Part:	FCT-UNL
Desenho	PA	15/01/15	**Upper Lid**	
Verificação	OT	15/01/15		
MATERIAL: PLA				
Size: A4 Scale: 1 : 1	Tolerância: ±0.05		Assembly: Cylindrical Spinning Rotor Gauge	1 parts

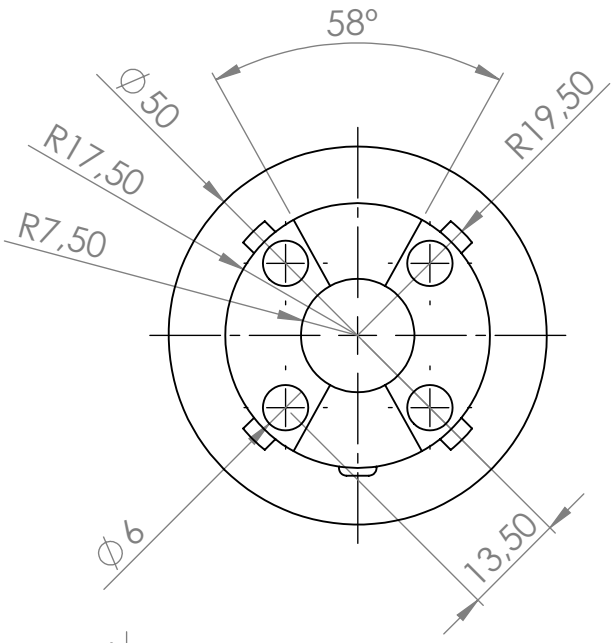

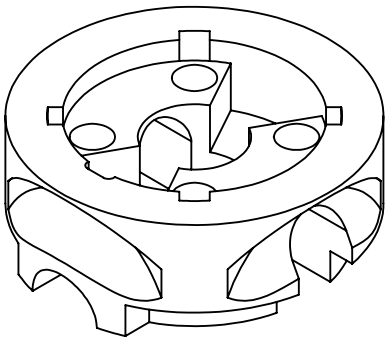

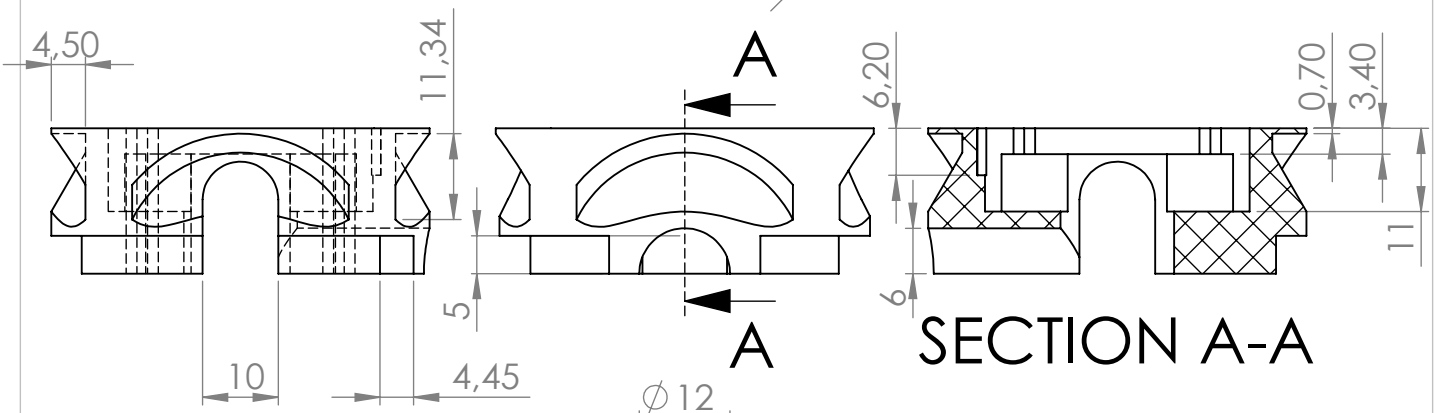

SECTION A-A

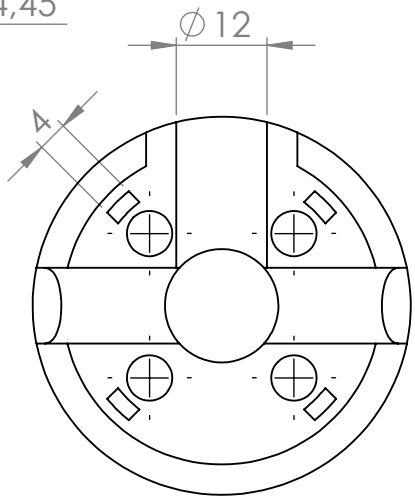

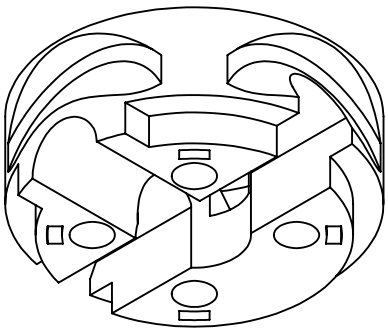

	Name	Date	Part:	FCT-UNL
Desenho	PA	15/01/15	**Upper Body**	
Verificação	OT	15/01/15		
MATERIAL: PLA				
Size: A4 Scale: 1 : 1	Tolerância: ±0.05		Assembly: Cylindrical Spinning Rotor Gauge	1 part

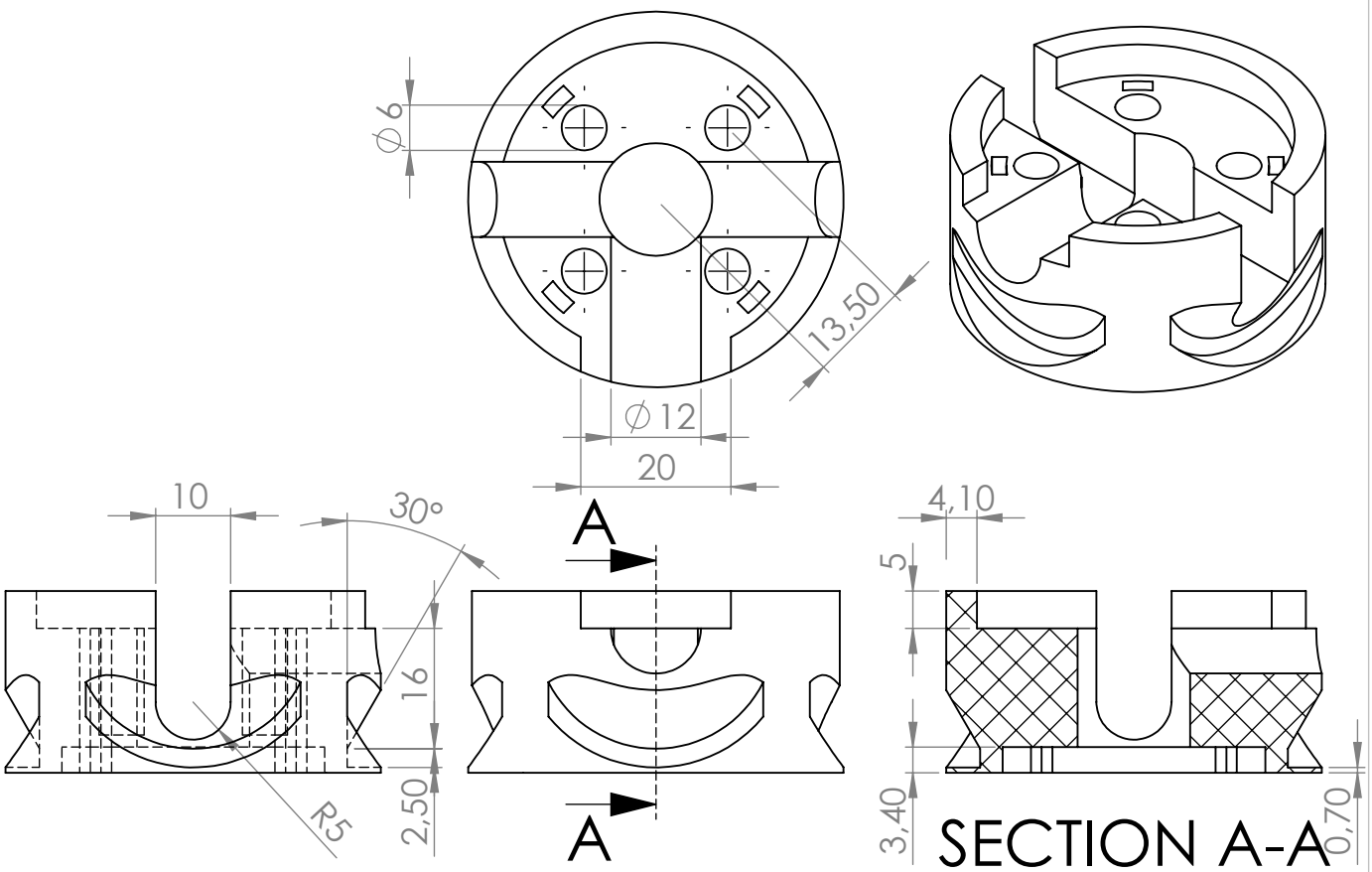

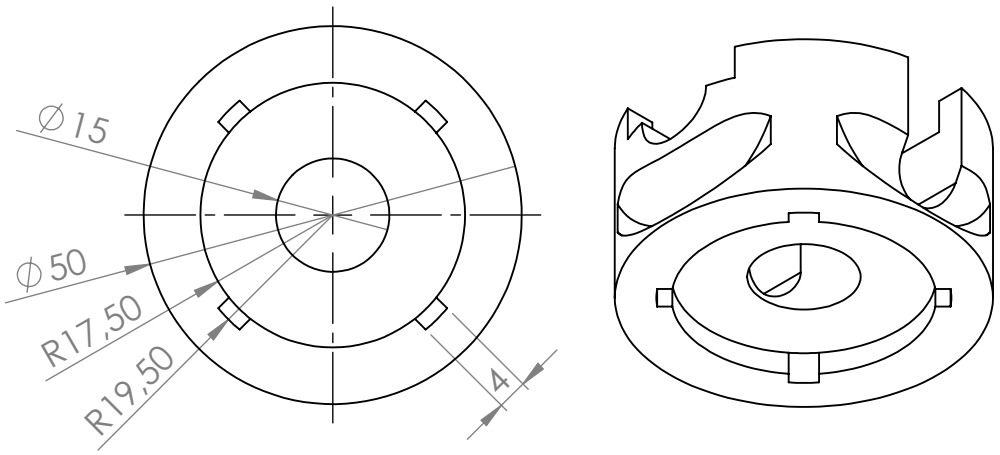

	Name	Date	Part:	FCT-UNL
Desenho	PA	15/01/15	**Lower Body**	
Verificação	OT	15/01/15		
MATERIAL: PLA				
Size: A4 Scale: 1 : 1	Tolerância: ±0.05		Assembly: Cylindrical Spinning Rotor Gauge	1 part

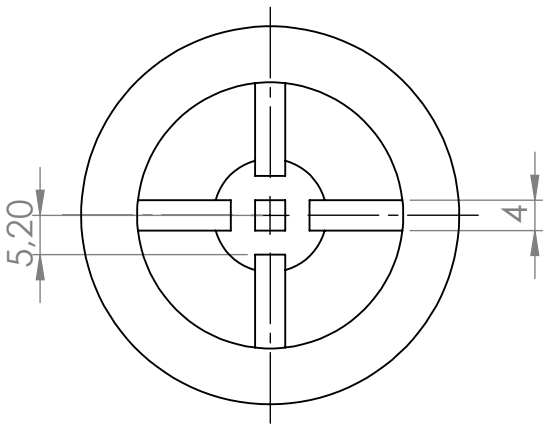

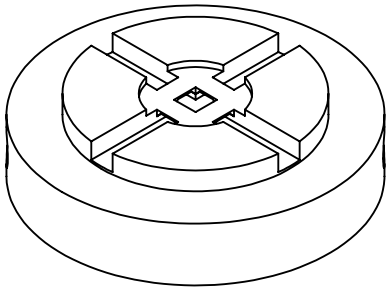

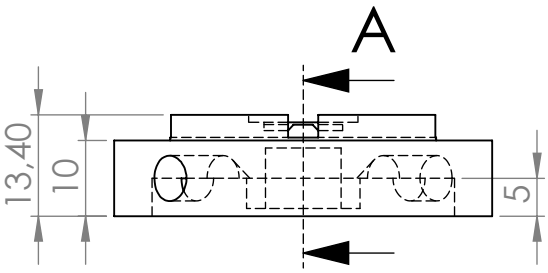

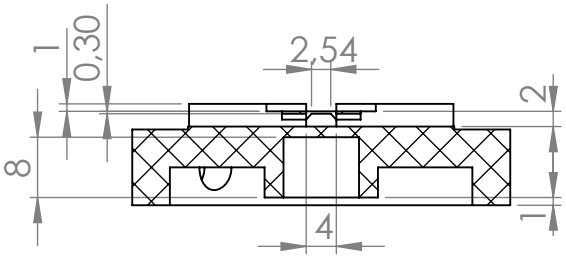

SECTION A-A

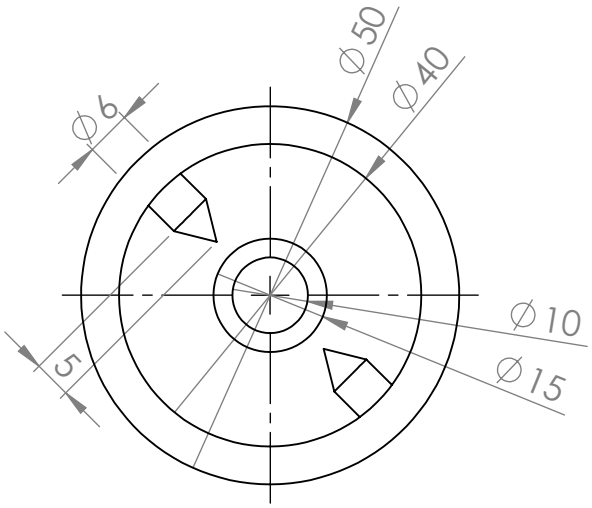

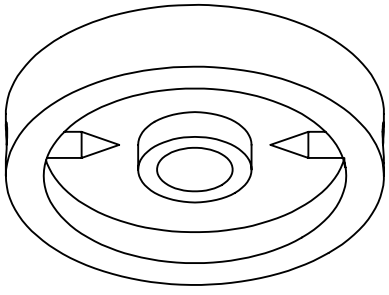

	Name	Date	Part:	FCT-UNL
Desenho	PA	15/01/15	**Lower Lid**	
Verificação	OT	15/01/15		
MATERIAL: PLA				
Size: A4 Scale: 1 : 1	Tolerância: ±0.05		Assembly: Cylindrical Spinning Rotor Gauge	1 part

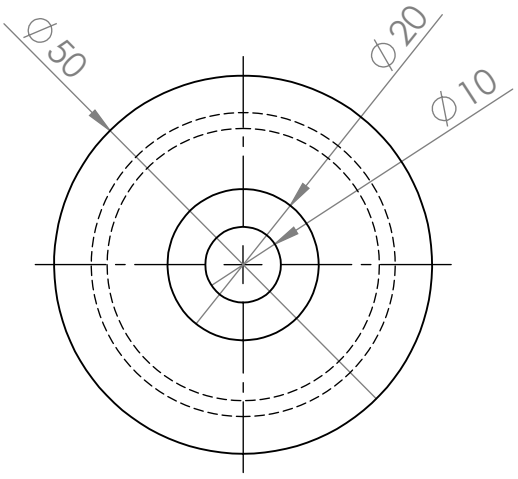

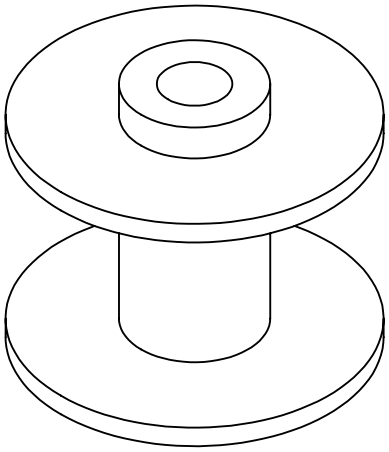

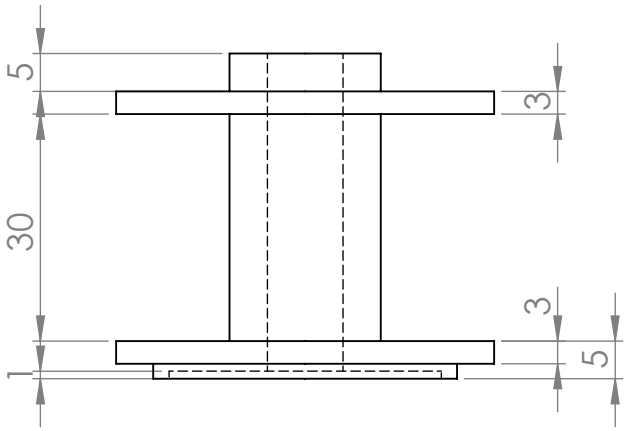

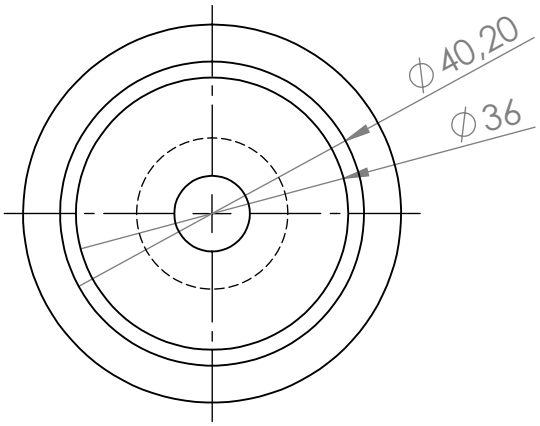

	Name	Date
Desenho	PA	15/01/15
Verificação	OT	15/01/15

Part:

Magnetic Suspension Coil Support

FCT-UNL

MATERIAL:

PLA

Size: A4

Scale: 1 : 1

Tolerância:

±0.05

Assembly:

Cylindrical Spinning Rotor Gauge

2 parts

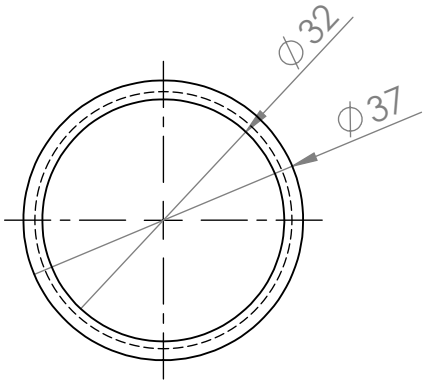

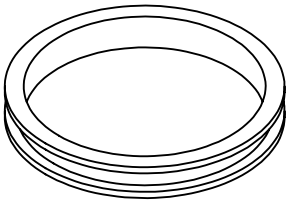

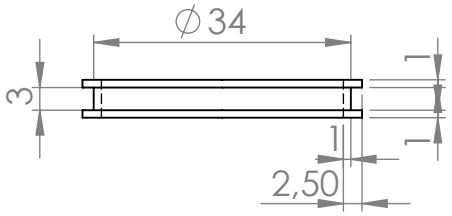

	Name	Date	Part:	FCT-UNL
Desenho	PA	15/01/15	**Driving Coil Support**	
Verificação	OT	15/01/15		
MATERIAL: PLA				
Size: A4 Scale: 1 : 1	Tolerância: ±0.05		Assembly: Cylindrical Spinning Rotor Gauge	4 parts

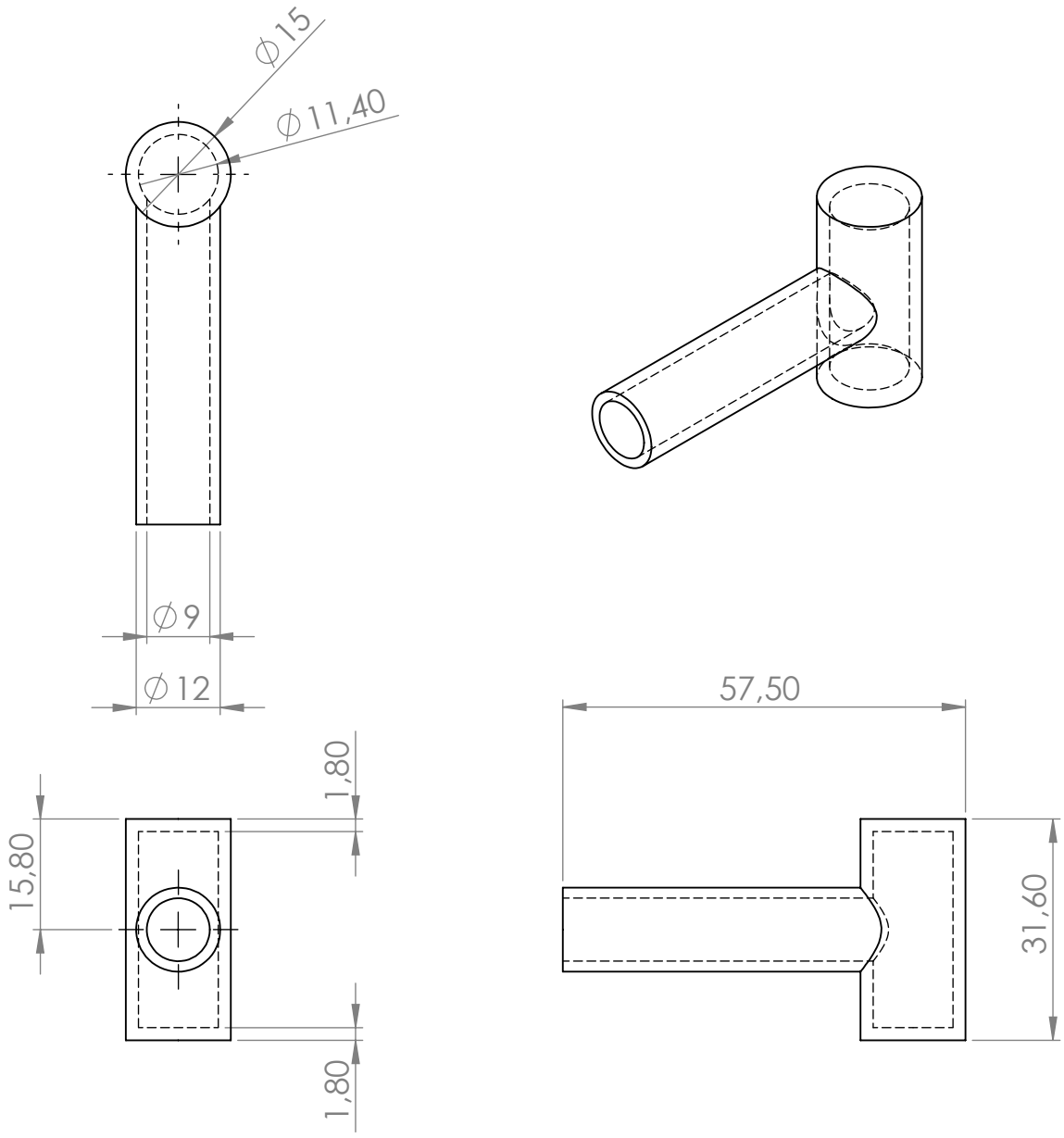

	Name	Date	Part:	FCT-UNL
Desenho	PA	15/01/15	**Glass Chamber**	
Verificação	OT	15/01/15		
MATERIAL: Glass				
Size: A4 Scale: 1 : 1	Tolerância: ±0.05		Assembly: Cylindrical Spinning Rotor Gauge	1 part